Journal of Advanced Ceramics
2021, **10**(5): 933–972
https://doi.org/10.1007/s40145-021-0489-7

ISSN 2226-4108
CN 10-1154/TQ

Review

Garnet-type solid electrolyte: Advances of ionic transport performance and its application in all-solid-state batteries

P. M. GONZALEZ PUENTE[a], Shangbin SONG[b], Shiyu CAO[b], Leana Ziwen RANNALTER[a], Ziwen PAN[b], Xing XIANG[a], Qiang SHEN[a], Fei CHEN[a,b,*]

[a]*State Key Lab of Advanced Technology for Materials Synthesis and Processing, Wuhan University of Technology, Wuhan 430070, China*
[b]*International School of Materials Science and Engineering, Wuhan University of Technology, Wuhan 430070, China*

Received: January 1, 2021; Revised: April 4, 2021; Accepted: April 27, 2021

Abstract: All-solid-state lithium batteries (ASSLBs), which use solid electrolytes instead of liquid ones, have become a hot research topic due to their high energy and power density, ability to solve battery safety issues, and capabilities to fulfill the increasing demand for energy storage in electric vehicles and smart grid applications. Garnet-type solid electrolytes have attracted considerable interest as they meet all the properties of an ideal solid electrolyte for ASSLBs. The garnet-type $Li_7La_3Zr_2O_{12}$ (LLZO) has excellent environmental stability; experiments and computational analyses showed that this solid electrolyte has a high lithium (Li) ionic conductivity (10^{-4}–10^{-3} S·cm^{-1}), an electrochemical window as wide as 6 V, stability against Li metal anode, and compatibility with most of the cathode materials. In this review, we present the fundamentals of garnet-type solid electrolytes, preparation methods, air stability, some strategies for improving the conductivity based on experimental and computational results, interfacial issues, and finally applications and challenges for future developments of LLZO solid electrolytes for ASSLBs.

Keywords: $Li_7La_3Zr_2O_{12}$ (LLZO); solid electrolytes; lithium ionic conductivity; lithium concentration; mobility of lithium-ion; air stability; solid-state batteries

1 Introduction

Lithium-ion batteries (LiBs) have been broadly used in portable electronics and mobile communication because of their high energy density, high operating voltage, and long cycle life. However, current commercially available LiBs generally used liquid electrolytes. Although the liquid electrolyte has high Li-ion conductivity, critical safety issues such as overcharging or short-circuiting, easy leakage, corrosion, and high temperature decomposition make it have safety hazard result in fire or explosion [1,2]. The liquid electrolyte easily reacts with the electrode to produce Li dendrites, which lead to serious safety problems, resulting from thermal runaway of chemical exothermic reactions and must be solved considering the requirements of a large-scale application in the field of electrochemical

* Corresponding author.
E-mail: chenfei027@whut.edu.cn

energy storage [3,4].

The development of electrochemical energy storage devices for these applications has become subject of extensive research. Studies have been directed to understand the performance, safety, energy density, and cost requirements for the batteries of the future: all-solid-state lithium batteries (ASSLBs). Compared with LiBs using liquid electrolytes, ASSLBs (Fig. 1) are simple in structure and small in size, and may solve the safety concerns by replacing the liquid with solid electrolytes which results in a longer life cycle, simplify the manufacturing process, and increase energy density [5]. The main working principle of ASSLBs is the solid electrolyte (SE), which functions not only as an ionic conductor but also a separator, allowing the transfer of ions from the anode (negative) to the cathode (positive) during the charging and discharging processes, and the electrons generated by the reaction are used to promote a load in the external circuit [6]. Therefore, SEs are promising candidates to improve the overall performance of batteries. Battery performance depends on the materials used, so the development of new SEs and electrode materials are important in battery technology development. Several critical issues need to be considered for real-world applications, including the improvement of low ionic conductivities of SEs at low temperatures, large interfacial resistance at the electrode–electrolyte solid interface, poor electrochemical compatibility with electrodes such as Li-metal anodes and high-voltage cathode materials, enhanced physical stability, and better understanding of the interfacial process after charge/discharge of the battery [7]. Even though there is a fast development in ASSLBs, the safety and manufacturing process are another important challenges to fulfill the requirements of safe solid storage systems [8].

There are two general classes of materials used for SEs in ASSLBs: inorganic and polymer electrolytes. The main difference between them is the mechanical properties that influence the battery design. Although polymers are easier to process and reduce the fabrication costs, they possess a low Li-ion conductivity for battery operation at room temperature (RT). However, polymer electrolytes can be combined with Li anodes and safely cycled at elevated temperatures [9]. Therefore, challenges remain to develop stable polymer electrolytes for applications with Li metal anode and cathode materials at acceptable C-rates.

The key functional features of solid electrolytes should include: high electrochemical decomposition voltage of 5 V vs. Li/Li^+; chemical stability against reaction with the electrodes to prevent the formation of any undesired products at the electrode–electrolyte interfaces; negligible electrode–electrolyte interface charge transfer resistance; low cost; environmental friendliness; and most importantly a high Li-ion conductivity of about 10^{-4} $S \cdot cm^{-1}$ [10,11]. Inorganic solid electrolytes are more suitable for high temperatures or aggressive environments, and a wide range of inorganic electrolytes have been developed, due to their amorphous and crystalline structures [12]. These two structures enable ion transport, as they provide

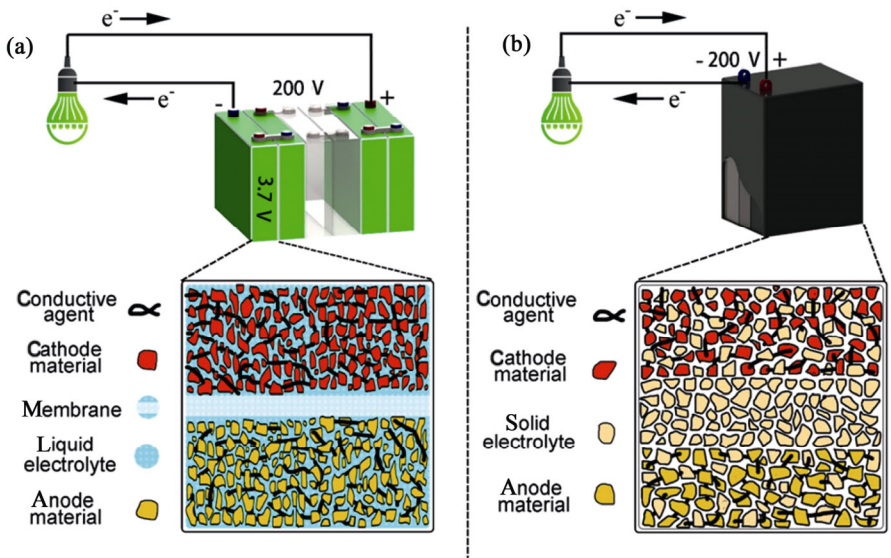

Fig. 1 A schematic representation of (a) a traditional Li-ion battery (LiB) using a liquid electrolyte and (b) all solid-state lithium-ion battery (ASSLB) using a solid electrolyte. Reproduced with permission from Ref. [9], © *Materials China* 2017.

enough vacancies and coordination defects that enable the flux of a number of ions throughout the framework [13–15]. Crystalline materials offer the highest Li-ion conductivities in SEs. The main inorganic SEs being explored are NASICON-type, perovskite-type, LISICON-type, garnet-type, and sulfide-type materials. Research has shown that $Li_{1+x}Al_xTi_{2-x}(PO_4)$ (LATP) and $Li_{1+x}Al_xGe_{2-x}(PO_4)_3$ (LAGP) exhibited high ionic conductivity (up to 10^{-3} S·cm^{-1}), but they are unstable against Li metal anodes due to facile Ti^{4+} reduction [16,17]. LLTO presents a similar problem at the interface with metallic Li, but the synthesis methods also result in high Li_2O losses [18]. $L_7P_3S_{11}$, a sulfide-type material presents the highest ionic conductivity (10^{-2} S·cm^{-1}), though it is sensitive to moisture and has poor compatibility with cathode materials [19]. Nevertheless, the major drawback of all of them is their mechanical properties. Table 1 summarizes the main characteristics of inorganic SEs. Thus, it is a major challenge to determine which electrolyte is more suitable for solid battery development and application, material synthesis, and device integration.

Garnet-type $Li_7La_3Zr_2O_{12}$ (LLZO) electrolytes stand out as the most promising SEs. LLZO presents high ionic conductivity at RT (10^{-4}–10^{-3} S·cm^{-1}), wide electrochemical window range (0–5 V), and good stability against Li metal anode, all this according to the first-principals calculation and experimental results. LLZO is also simple environmental caring [20–23]. Figure 2 shows a brief chronology of the development of garnet-type solid electrolytes among ASSLBs. In 2003, Thangadurai and coworkers [24] reported $Li_5La_3M_2O_{12}$

Table 1 Summary of the main characteristics of inorganic solid electrolytes

Material	Type	Ionic conductivity (S·cm^{-1})	Advantages	Disadvantages
NASICON: $Li_{1+x}Al_xGe_{2-x}(PO_4)_3$	Crystalline	10^{-5}–10^{-3}	High chemical and electrochemical stability	Non-flexible
LISICON: $Li_{14}Zn(GeO_4)_4$	Crystalline		High mechanical strength	Expensive large-scale production
Garnet-type: $Li_7La_3Zr_2O_{12}$	Crystalline		Good crystallinity High density	Heterogeneous phase
Perovskite: $Li_{3.3}La_{0.56}TiO_3$	Crystalline Amorphous		High electrochemical oxidation voltage	High interfacial resistance
Sulfide: Li_2S–P_2S_5 Li_2S–P_2S_2–MS_x	Glass-ceramic	10^{-6}–10^{-2}	High conductivity Good mechanical strength and mechanical flexibility Low grain-boundary resistance Easy to operate	Low oxidation stability Sensitivity to moisture Poor compatibility with cathode materials

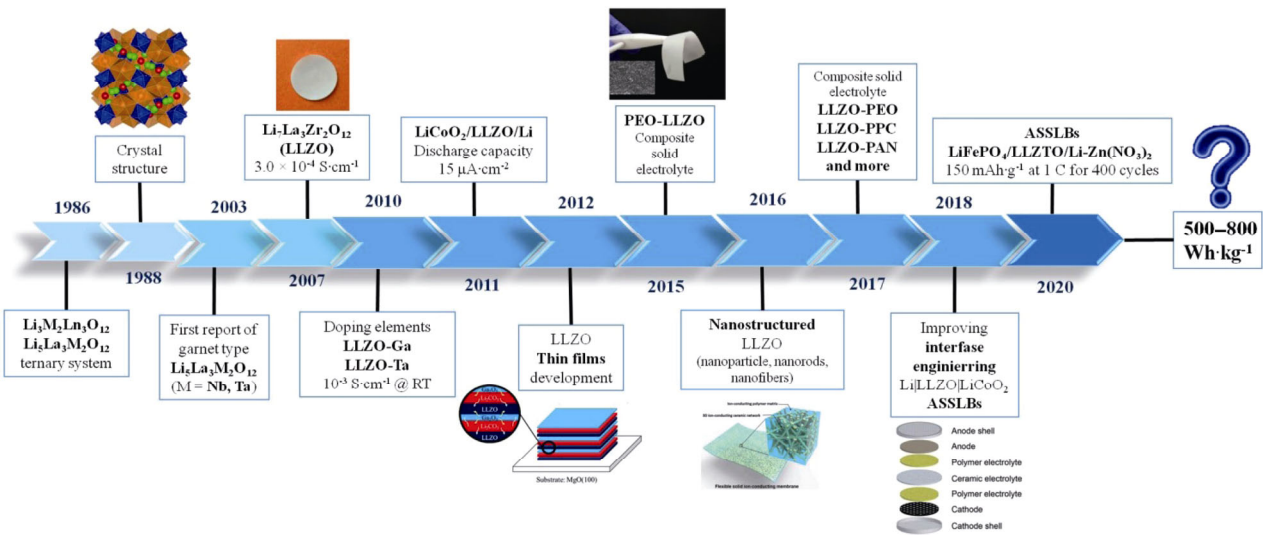

Fig. 2 A brief chronology of the development of garnet-type solid electrolytes: since the crystal structure reported, the first value of the ionic conductivity, doping elements used to improve ionic conductivity, distinct morphology development, and compatibility with polymers, Li anodes and cathodes among ASSLBs [24,28,29,33–40].

(M = Nb, Ta, Bi, Sb) with a bulk ion conductivity of 10^{-6} S·cm^{-1} at RT. After this study, several Li garnet-types have attracted attention due to their desired physical and chemical properties for application as solid electrolytes in ASSLBs. The most notable composition of garnet-type is $Li_7La_3Zr_2O_{12}$ (LLZO), which has two polymorphs: a cubic phase (c-LLZO) and a tetragonal phase (t-LLZO) [24–26]. The c-LLZO phase presents the highest values of ionic conductivity. Substitution is the primary method to improve the conductivity; commonly studied garnets typically contain five to seven Li atoms per formula unit, which allowed them to induce changes in the Li-ion distribution [27,28]. Further doping with tantalum (Ta) and gallium (Ga) elements resulted in an improvement of ionic conductivity, to 10^{-3} S·cm^{-1} [29,30]. Experimental and computational simulation results suggest that the coordinated migration of Li-ions by the side of Li1 and Li2 sites, contributes to auto-diffusion in the cubic phase in LLZO; *ab initio* molecular dynamics method (AIMD) confirms that the Li transport mechanism is related to Li-ion concentration [31,32].

In 2010 early studies of the compatibility of LLZO SE for ASSLBs were focused on the usage of Li metal anode [35]. The composite solid electrolyte (CSE) in 2015, utilizing mainly polyethylene oxide (PEO) and some other polymer materials such as polyacrylonitrile (PAN), poly(vinylidene fluoride) (PVDF), and poly(methyl methacrylate) (PMMA), has been investigated [36]. The research showed that the morphology of LLZO has a significant influence on the overall performance of the SE, and the chemical and mechanical interactions between ceramic particles and polymer matrix enable fast Li^+ conduction and wide electrochemical window in the CSE [31].

Therefore, efforts have been directed to understand diverse methods of synthesis of garnet-type materials and development of diverse morphologies and structures such as bulk ceramics, thin films, and nanostructured LLZO [29]. However, challenges in producing effective ion transmission networks, enhance the need of engineering stable electrolyte–electrode interfaces with cathode and Li metal anode materials [35–40]. Current research is oriented towards the construction of high energy density Li batteries all over the world. The goal of the "future batteries" is to produce a battery pack of 500–800 Wh/kg. It will only be achieved by focusing on developing methods to increase our understanding of the multiple non-equilibrium process in batteries, exploring the use of Li batteries in large energy storage systems, with higher performance, low cost for applications, and low maintenance for grid storage.

We will review now the fundamentals of garnet-type electrolyte LLZO, and discuss the developments and strategies used by researchers to improve the performance of LLZO as an SE. We will describe the Li-ion conductivity, chemical composition, stability in the air, and interfacial properties between LLZO and electrodes, as well as the electrochemical stability, with different types of anode and cathode materials based on experimental and computational results. Then, we comment on the mechanisms by which the LLZO-based and LLZO–polymer solid electrolytes operate in a full battery with different LLZO/electrode interfaces. Finally, we provide information about further application of solid electrolytes in ASSLBs, challenges, and perspectives.

2 Crystal structure and phase transition of LLZO

LLZO is represented by the general chemical formula $A_3B_2(CO_4)_3$, where the cations A, B, and C occupy crystallographic sites with 8-fold, 4-fold, and 6-fold oxygen coordination sites respectively, which usually crystallize in cubic structure with the space group $Ia-3d$ [41]. The LLZO has two polymorphs with Li^+ ionic conductivities that differ by 2–3 orders of magnitude. One is the t-LLZO, space group $I4_1/acd$, with a garnet-type framework with two types of dodecahedral LaO_8 polyhedral (8b and 16e) and ZrO_6 octahedral (16c) (Fig. 3(b)). The Li ions occupy three distinct sites in the t-LLZO. The first one is the tetrahedral 8a site with distorted octahedral 16f and 32 sites (Fig. 3(f)) [42], which is thermodynamically stable at RT [43] and presents a total ionic conductivity of 10^{-7}–10^{-6} S·cm^{-1} and lattice constant of a = 13.134(4) Å, c = 12.663(8) Å, and c/a = 0.9641 [42,44]. The second one is the t-LLZO with a desired cubic structure (c-LLZO), space group $Ia-3d$, with a framework of 8-fold coordinated LaO_8 dodecahedra (24c) and 6-fold coordinated ZrO_6 octahedra (16a). This site possesses the higher ionic conductivity of 10^{-4} S·cm^{-1} (Fig. 3(a)). In addition to the distinct value of ionic conductivity, the most significant difference between the two structures is the distribution of Li. In the cubic phase Li ions occupy two positions (Li1-tetrahedral

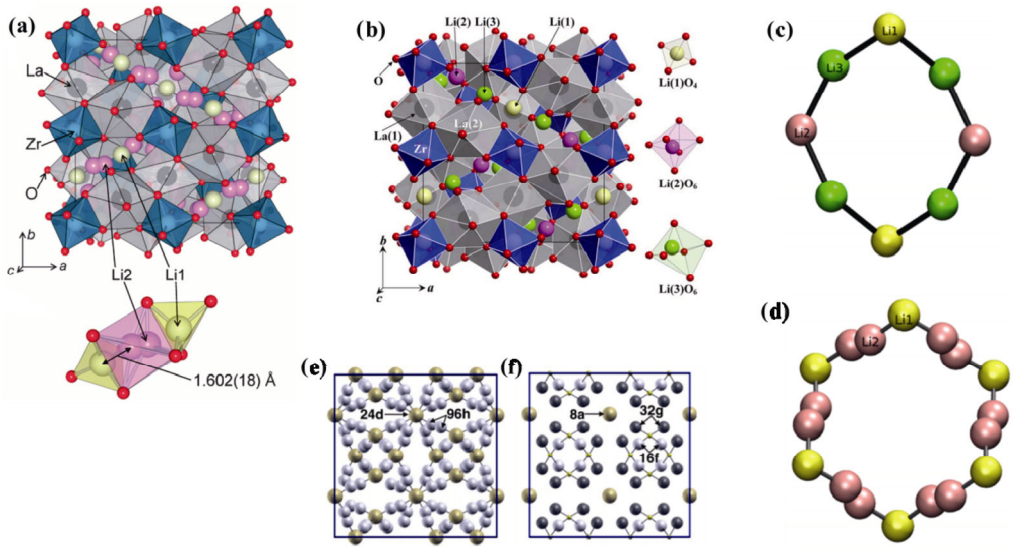

Fig. 3 Crystal structure of (a) cubic LLZO and (b) tetragonal LLZO. Reproduced with permission from Ref. [42], © Elsevier Inc. 2009; Ref. [47], © The Chemical Society of Japan 2011. Loop arrangement of different Li sites: tetrahedral Li1 site (yellow), octahedral Li2 (pink), and Li3 (green) sites: (c) tetragonal LLZO, (d) cubic LLZO. Reproduced with permission from Ref. [51], © American Chemical Society 2014. Li sublattice in the cubic (e) and tetragonal (f) phases of LLZO. All Li positions are included, although, in the cubic phase, not all are occupied. The Li (1) atoms (8at and 24dc) are large gray (gold), Li (2) atoms (16ft and 96hc) are white, and Li (3) atoms (32gt) are dark gray. The cubic Li (1) positions that become vacant upon transition to the ordered tetragonal structure (16et) are indicated by small (gold online) spheres. Reproduced with permission from Ref. [43], © American Physical Society 2012.

void 24d and Li2-eccentric octahedral gap 96h) (Figs. 3(d) and 3(e)), while in the tetragonal phase Li is fully occupied (Li1 tetrahedral void 8a, Li2 octahedral gap 16f, and Li3-eccentric octahedral gap 32), which impedes the ion transmission between the adjacent positions [45]. However, as Li ions are unstable at Li3 sites, lithium ions primarily occupy the Li1 and Li2 sites, forming a Li-ion channel for t-LLZO (Fig. 3(c)). Murugan *et al*. [33] were the first to report a c-LLZO ($Li_7La_3Zr_2O_{12}$) synthesized at 1230 ℃ (a = 12.9682(6) Å; $Ia-3d$ space group) with a face-centered cubic (FCC) anionic framework. Based on crystal lattice evidence of pure LLZO phases, the constant ranges from 12.95 to 12.97 Å [35,46–48]. The phase stability of LLZO has become a challenge. LLZO can transform from cubic to tetragonal phase in a transition process called tetragonal distortion. The tetragonal distortion is a result of Li^+ redistribution that removes the short Li−Li interactions and disordered Li^+. The 24th site in the cubic phase is transformed into fully occupied 8a sites and unoccupied 16e sites, while the 96h site is in the cubic phase. The cubic phase is then transformed into two 16f and 32g sites [43,49,50] (Fig. 4(a)). The lattice parameters documented in the literature range in a = 13.07–13.12 Å and in c = 12.67–12.72 Å in the tetragonal distortion. Several studies have shown that

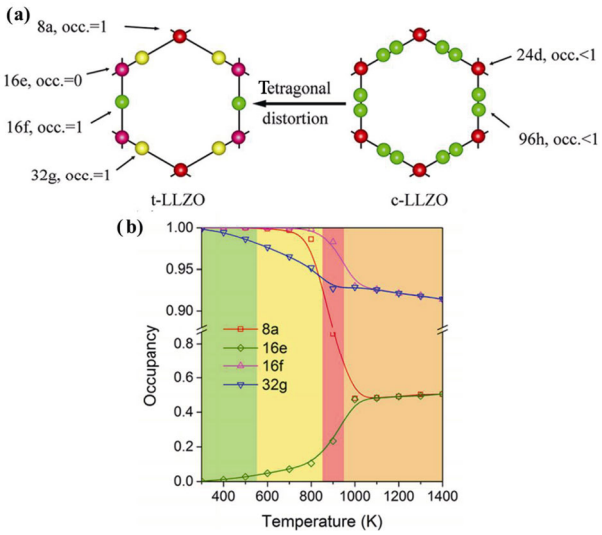

Fig. 4 Computational results of the lithium arrangements. (a) The loop structure of lithium arrangement in both tetragonal and cubic LLZO. (b) Temperature dependence of site occupancies in LLZO. Reproduced with permission from Ref. [50], © American Chemical Society 2018.

tetragonal distortions had an effect on the Li distribution and decreased the ionic conductivity over two orders of magnitude [33,42]. By density-functional theory (DFT) and molecular dynamics (MD), Bernstein *et al.* [43] argued that at low temperatures the tetragonal structure is formed and at higher temperatures, the

cubic phase appears. Also, the transition temperature decreases with an increasing concentration of Li^+ vacancy, and the disrupted cubic structure has lower energy when the number of vacancy positions per formula unit is greater than about 0.4. Therefore, the tetragonal phase stability benefits from Li-ion sublattice ordering and volume preservation of tetragonal distortion, which generate the Li–Li gap and relieve the Coulomb repulsion [46].

Structural data obtained by *in situ* synchrotron X-ray diffraction (SXRD) of atomic layer deposition (ALD) showed that the phase transition of LLZO is related to an annealing temperature as low as 555 ℃ [52]. Rather low temperatures achieved the tetragonal phase of LLZO (< 650 ℃) (space group $4_1/acd$) and ionic conductivity two to three orders of magnitude lower than the high-temperature cubic phase [47]. Experimental and molecular studies have reported the phase transition of $Li_7La_3Zr_2O_{12}$ change through tetragonal to cubic phase between 177 and 750 ℃ [10]. Studies by Chen *et al*. [50] combined MD and DFT to simulate LLZO, and found two important factors of origin of the phase transition. The evolution of the Li migration pathway can be divided into four stages by temperature dependence of the occupancy of different sites and the effects on the Li distribution when supervalent elements are doped with LLZO. The four stages of Li migration pathways are oscillation, local migration, 2-dimensional-like migration, and 3-dimensional migration (Fig. 4(b)) these combine occupancy and local structure by temperature. In the 2-dimensional-like migration, there are vacancies in 8a, 32g, and 16e sites, which are responsible of the formation of the Li migration pathways *a* and *b* (parallel), and *c* (perpendicular) dimensional directions. The *a* and *b* pathways intersect at 8 sites and Li-ions can be exchanged in these two directions, making the ionic conduction in the *c* direction relatively small and blocked by 16f sites [51]. When 16f sites participate in the Li conduction, the 3-dimensional migration is formed as a result of no blocking ions; in the meantime the gap of diffusivity between the *ab* plane and *c* direction is reducing, suggesting a blocking effect of 16f sites, and thus, reducing the temperature of the phase transition from the tetrahedral phase to the cubic phase [47]. These studies also revealed that Ta doping can stabilize the cubic phase at low temperatures by variating the site occupancy with different contents of Ta as a function of temperature [53,54].

Studies on phase stability of LLZO described the influence of the temperature in the phase stability. In addition to the high conductive cubic phase and the tetragonal phase, another phase was identified and called the "low-temperature cubic phase" [42–47]. Early studies suggest that the nature of the low-temperature cubic phase showed in Li garnet materials was caused by the sensitivity to humid conditions and the formation of a low-temperature cubic phase between the transition of cubic to tetragonal phase was cause by hydration mechanisms [55–57]. Recent studies of nuclear magnetic resonance spectroscopy (NMR) revealed that when we use Al-doped LLZO, aluminum (Al) cations slowly diffuse into the LLZO structure forming Li_5AlO_4, which react with the tetragonal phase and transform into the cubic phase LLZO [58]. However, multiple Al environments may occur due to the disorder generated by the 24d Li site shown on the crystal structure, which results in the formation of the low-temperature cubic phase [58]. Recent confirmation of LLZO doping demonstrates the influence of Al and Ta elements on the formation of the cubic phase of LLZO at lower temperatures. In the structure of the high-temperature cubic phase (space group $Ia-3d$) the Li sublattice is disordered with a partial site occupation, which influences the value of the Li^+ ionic conductivity to 10^{-4} S·cm^{-1} at RT [28,59]. One main drawback of the high-temperature cubic phase is that it is not stable at RT and a high temperature of sintering is required (> 1150 ℃). Various chemical compositions are possible by doping at different sites; further doping with elements closer to ionic radius is used to stabilize the c-LLZO and improve the ionic conductivity, and this strategy is one of the most powerful approaches in considering the usability of SE [60,61].

3 Development process and synthesis of LLZO

As discussed above, the cubic phase exhibits the highest ionic conductivity and its stabilization is a critical issue. Furthermore, it has been shown that synthesis conditions, such as sintering temperatures, have a high effect on the crystal microstructure (e.g., crystal size, grain size, grain boundary, and bulk density, which can influence the ionic conductivity of LLZO), resulting in different ionic conductivity and electrochemical performance [62–64]. The total ionic conductivity of LLZO is affected by the grain

boundary resistance due to the impure phases at the boundary [65]. Therefore, increasing the density of the LLZO electrolyte is essential to improve ionic conductivity, as it not only reduces the grain boundary, but also increases the mechanical strength [66]. Adding sintering aids and applying different sintering methods, such as hot-pressing and discharge plasma sintering, can be an alternative to solve this issue. Various methods have been used to synthesize LLZO, being the conventional solid-state reaction the most commonly utilized in laboratories [67]. However, this method requires high temperatures and high energy consumption, which leads to reactivity with the reaction vessels. Other chemical techniques to synthesize dense LLZO are the sol–gel and co-precipitation methods [68]. These permit good ionic conductivity at low sintering temperatures and can regulate the microstructure, hot-press sintering [69], and field-assisted sintering [65]. Sophisticated sintering methods allow to optimize the performance of the bulk LLZO, and some examples include electrospinning [70,71], thin-film preparation technology [72], and spark plasma [73] (Table 2). The most common method of synthesis yields a high ionic conductivity in the cubic phase of LLZO and, as a result, enhances Li ionic transport in the SE [8]. However, current research shows that existing preparation methods of LLZO still present some challenges and limitations, such as availability of commercially reagents, problems to densify in a thin format to reduce ohmic resistance, and incorporation into a battery with a suitable mixture of electrode materials. After all, LLZO has a strong potential to become a promising electrolyte in the development of future ASSLBs.

4 Challenges on LLZO air stability

Theoretical calculations and experiments revealed that garnet electrolytes are unstable in the air, to atmospheric moisture and carbon (IV) oxide (CO_2), leading to lithium carbonate (Li_2CO_3) formation, ionic conductivity degradation, and high interfacial resistance [79,80]. Li_2CO_3 easily forms a coat on the surface of LLZO because it can react with H_2O and CO_2 in the air, as shown in Fig. 5. Cheng *et al.* [81,82] reported that a Li_2CO_3 coating was formed on the surface of LLZO when LLZO pellets were exposed to air. Different mechanisms have been reported to describe the reaction between garnet electrolytes and air. The most satisfactory mechanism involves a two-step reaction. First Li^+/H^+ exchange occurs between LLZO and moisture, forming the LiOH intermediate (Eq. (1.1)). Then, upon exposure to CO_2 in the air the LiOH transforms into Li_2CO_3 constituting a contaminating layer on the surface of LLZO (Eq. (1.2)) [83–85]:

Table 2 Advantages and disadvantages of different LLZO synthesis methods

Synthesis method	Advantages	Disadvantages	Ionic conductivity ($S \cdot cm^{-1}$) at 25 ℃	Ref.
Conventional solid-state reaction	High values of density and ionic conductivity Flexible and cheap Scalability from laboratory to industrial scale	High sintering temperature Long sintering time Lithium loss Repeated heat treatment and intermittent grinding powder	2.11×10^{-4}	[74]
Sol–gel	Lower sintering temperature Shorter time density and ionic conductivity	Low sample density Cubic phase instability	3×10^{-4}	[75]
Hot-press sintering	High density and ionic conductivity	No scalability from laboratory to industrial scale Slow heating and cooling speed	9.9×10^{-4} 4.0×10^{-4}	[62]
Field-assisted sintering	Quick heating rates High density and ion conductivity Short sintering time at lower sintering temperatures	Expensive equipment	0.33×10^{-3} 5.7×10^{-4}	[63,65]
Electrospinning	Nano structuring Cubic phase LLZO stability at RT Phase transformation	Bulk of LLZO cannot be prepared	—	[70]
Thin films	Practical for commercialization	Nanopowders required Low ionic conductivity	1.67×10^{-6}	[76]
Spark plasma	Low sintering temperature Short sintering time Rapid densification Scalability from laboratory to industrial scale	Previous synthesis method required	1.35×10^{-3}	[77,78]

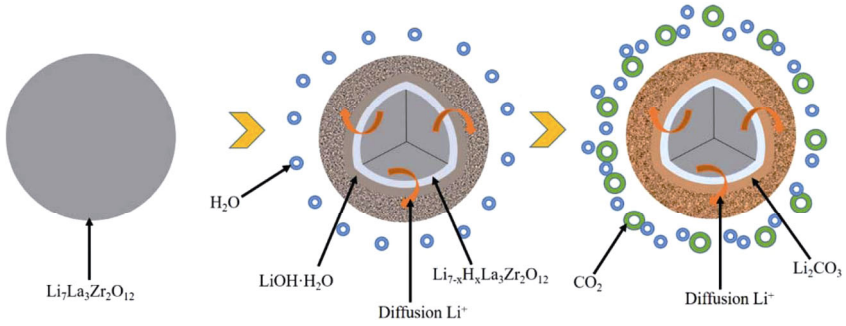

Fig. 5 A schematic representation of the Li_2CO_3 formation process on the surface of lithium garnets. Reproduced with permission from Ref. [84], © The American Ceramic Society 2017.

$$Li_7La_3Zr_2O_{12} + xH_2O \rightarrow Li_{7-x}H_xLa_3Zr_2O_{12} + xLiOH \quad (1.1)$$

$$LiOH + \frac{1}{2}CO_2 \rightarrow \frac{1}{2}Li_2CO_3 + \frac{1}{2}H_2O \quad (1.2)$$

Formation of LLZO also requires a direct, slow, and difficult reaction with CO_2, which is favored when surface Li levels are lower, as with the small-grained samples (Eq. (1.3)) [86]:

$$Li_7La_3Zr_2O_{12} + xCO_2 \rightarrow Li_{7-2x}La_3Zr_2O_{12-x} + xLi_2CO_3 \quad (1.3)$$

The contaminating layer formed on the surface of LLZO decreases the ionic conductivity and induces an increase of interfacial resistance of the electrolyte–electrode interface. Studies from Kobi and Mukhopadhyay described that spontaneous cracking of LLZO occurs during storage of c-LLZO pellets in ambient air atmosphere for a few weeks possibly due to the formation of $La_2Zr_2O_7$ in the LLZO bulk [87]. X-ray diffraction studies indicate the formation of Li_2CO_3 and $LaAlO_3$ just the 3rd day ahead upon exposure to air following by the formation of $La_2Zr_2O_7$. The XRD pattern recorded in the pellet exposed to air for 6 days shows another additional small peak corresponding to cubic $La_2Zr_2O_7$ (Fig. 6(b)). Importantly, after 21 days of exposure to air, the intensity of the $La_2Zr_2O_7$ peaks increased significantly to the extent that it appeared to be the primary phase, co-existing with the original cubic garnet LLZO phase, and other impurity phases (Fig. 6(c)).

$$Li_{56}La_{24}Zr_{16}O_{96} + 28H_2O \rightarrow 56LiOH + La_{16}Zr_{16}O_{56} + 4La_2O_3 \quad (1.4)$$

$$Li_{56}La_{24}Zr_{16}O_{96} + 28CO_2 \rightarrow 28Li_2CO_3 + La_{16}Zr_{16}O_{56} + 4La_3O_3 \quad (1.5)$$

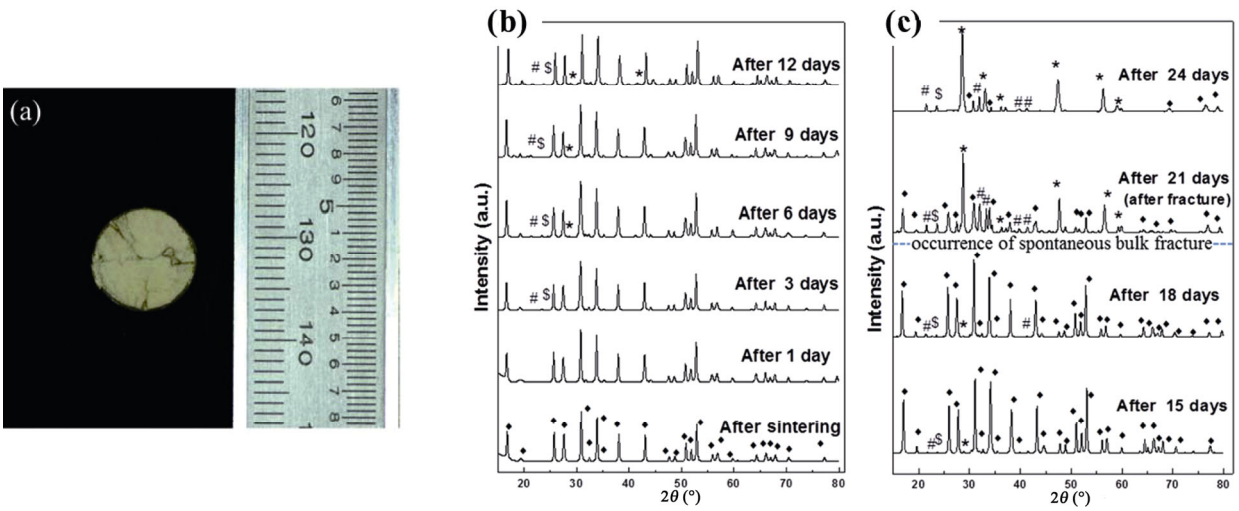

Fig. 6 Phase evolution and integrity of the pellets upon storage. (a) Photographs taken after 21 days for Al-doped LLZO pellets kept in an ambient air atmosphere. X-ray diffraction patterns recorded with sintered cubic Al-doped LLZO pellet, exposed to ambient air till (b) the 12th day and (c) from the 15th to the 24th day. The symbols correspond to: ♦ LLZO, # Li_2CO_3, $ $LaAlO_3$, and * $La_2Zr_2O_7$. Reproduced with permission from Ref. [87], © Elsevier Ltd. 2018.

Researchers discovered some factors that affected air stability of garnet electrolytes, like humidity, grain size, the amount of grain boundary, and relative density [85]. Sharafi and co-workers [83] exposed LLZO in the air at relative humidity (RH) ≈ 50% and RH ≈ 0.5% for 240 h. The LLZO exposed to dry air (RH ≈ 0.5%) presents a lower carbonate peak intensity at 1100 cm^{-1} when compared to LLZO in ambient air (RH ≈ 50%) exposed for the same amount of time (Fig. 7). This data indicates that the moisture content during exposure plays a significant role in the formation rate of Li_2CO_3 on the LLZO surface [84]. Also, the microstructure of LLZO: the pores, grain size, and grain boundaries influence the air stability. Xia *et al*. [88] prepared LLZO pellets in both Al_2O_3 and Pt crucibles. The pellets sintered in Pt crucibles have large grains and reduced grain boundaries compared to those in Al_2O_3 crucible. The formation of Li_2CO_3 was shown by X-ray photoelectron spectroscopy (XPS) as a lower peak for LLZO pellets sintered on Pt crucible. Using Pt crucible is favorable for the air stability, enhancing the ionic conductivity and relative density. However, Cheng *et al*. [82] demonstrated that smaller grain size (≈ 20 μm) leads to lower formation of Li_2CO_3 and higher air stability for LLZO pellets sintered on Al crucibles. By X-ray absorption spectroscopy (XAS) lower peaks of Li_2CO_3 of the small grain size LLZO are observed. They conclude this difference is due to that Al tends to segregate at grain boundaries for the small grain size LLZO, resulting in an Al-rich surface and the variation of the Al and Li distribution at the sample surface. More research is needed to clarify this topic.

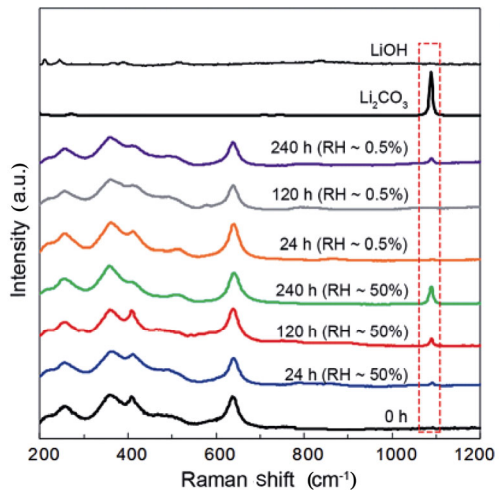

Fig. 7 Raman analysis of LLZO before and after exposure to ambient and dry air. The dotted line highlights the growth of the Li_2CO_3 layer on LLZO as a function of exposure time and RH. Topographic analysis of LLZO exposed to air (RH = 50%) for 240 h. Reproduced with permission from Ref. [83], © The Royal Society of Chemistry 2017.

Mechanical polishing [84], etching [89–91], and microstructure modification are effective methods to improve the air stability and interfacial issues of LLZO. The increase of interfacial resistance is caused by the Li_2CO_3 insulating surface layer, which can be removed effectively after surface polishing. Both thermal and chemical etching, can remove Li_2CO_3. Ruan *et al*. [90] demonstrated that H_3PO_4 can also react with the Li_2CO_3/LiOH passivation layer of the LLZT surface, and form a uniform Li_3PO_4 modification layer. This procedure transformed the contamination layer into SEI film which not only promoted interfacial wettability but also suppressed Li^{2+} dendrite penetration from the surface of LLZO [90]. For instance, Xia *et al*. [88] recovered 94.1% ionic conductivity of pellets stored in humid air for 6 weeks by removing the top reaction layer, that had originally caused a decrease in ionic conductivity to 55.9%, before surface polishing. Abdel-Basset *et al*. [91] demonstrated that thermally etching at 900 ℃ for 6 h partly removes the Li_2CO_3 layer as well as chemical etching using 0.5 M HNO_3 to remove the Li_2CO_3 layer for 15 min. Li *et al.* [89] developed a method to completely remove the Li_2CO_3 layer. In this study, the garnet was incubated with carbon-treated at 700 ℃ for 10 h which resulted in pellets with ultralow interfacial resistance. The lack of air stability of the garnet-type electrolytes may contribute to the high interfacial resistance hampering its development. Material properties, synthetic conditions, and the humidity in ambient air play an important role in the air stability. Approaches to mitigate the formation of the Li_2CO_3 need to be developed.

5 Mechanism and regulation of Li-ion transport

Since the discovery of the Li^+ conductivity in garnet-type electrolytes, extensive research has focused to understand the origin of this process. The flexibility of the garnet structure of Li^+, La^{3+}, and Zr^{4+} resolved in the LLZO crystal structure, showed that the ions can occupy octahedral and tetrahedral sites [92]. Furthermore, the differences in chemical stoichiometry may also

affect the ionic conductivity of Li^+ [47]. Thus, in addition to the effect of sintering temperature, the control of chemical stoichiometry and Li^+ concentration in LLZO is important to improve the ionic conductivity [51]. Li^+ conductivity is determined by the concentration and mobility (π) of the divalent cation. The properties of LLZO and doping mechanism can be expressed by the following equation: $\sigma = n_c \cdot e \cdot \mu$, where n_c, e, and μ represent Li^+ concentration, elementary load, and Li^+ mobility, respectively [43], and the elementary load is the Li^+ conductivity constant.

One way to improve the conductivity of LLZO is modifying the Li^+ concentration or the mobility of the cations [53,93]. This can be achieved by element doping or substituting ions following the specifications listed in Table 3. A considerable number of publications demonstrate that doping is increasingly being used in the synthesis of LLZO. Elements such as Fe, Ga, Al, Sr, Y, Ti, Ta, Sb, Mg, Sc, Zn, Ru, W, Nb, and Te [32,48,62, 92–96] have been demonstrated to promote the stabilization of the c-LLZO phase at RT by reducing the Li concentration or increasing Li vacancy content, which result in an improved Li^{2+}-ion conductivity [97,98]. Based on various doping sites of LLZO, doping may be classified into lithium-, lanthanum-, or zirconium-site. The lithium-site doping uses high-valent ions to replace Li from the sites, producing lithium vacancies that alter the concentration of Li^{2+} [63]. Through lanthanum- and zirconium-site doping, the size of the LLZO framework structure can be changed to adjust the size of the Li^{2+} ion migration path, ultimately changing its mobility [29,44]. In addition to affecting the size of the Li^{2+}-ion migration path, the concentration of Li-ion can be also affected by the lanthanum- and

Table 3 Summary of ionic conductivity, activation energy, and sintering temperature of different LLZO doping sites: Li, La, and Zr

Chemical formula	Sintering temperature (℃)	Ionic conductivity at RT ($S \cdot cm^{-1}$)	Activation energy	Ref.
Li-site substitution				
$Li_{6.4}Fe_{0.2}La_3Zr_2O_{12}$	750 ℃ for 4 h	1.1×10^{-3}	—	[99]
$Li_{6.25}Fe_{0.25}La_3Zr_2O_{12}$	1230 ℃ for 6 h	1.38×10^{-3}	0.28	[100]
$Li_{6.55}Ga_{0.2}La_3Zr_2O_{12}$	1230 ℃ for 4 h	1.32×10^{-3}	0.32	[101]
$Li_{6.25}Ga_{0.25}La_3Zr_2O_{12}$	1100 ℃ for 24 h	1.46×10^{-3}	0.25	[93]
$Li_{5.92}Al_{0.36}La_3Zr_2O_{12}$	1150 ℃ for 10 h	0.24×10^{-3}	NR	[102]
$Li_{6.64}Al_{0.12}La_3Zr_2O_{12}$	1100 ℃ for 3 h	0.33×10^{-3}	0.28	[75]
$Li_{6.95}Zn_{0.025}La_3Zr_2O_{12}$	1000 ℃ for 12 h	0.029×10^{-3}	0.254	[103]
La-site substitution				
$Li_{6.4}La_{2.4}Ce_{0.6}Zr_2O_{12}$	1050 ℃ for 1 h	1×10^{-4}	0.40	[95]
$Li_{7+x}La_{3-x}Sr_xZr_2O_{12}$	1200 ℃ for 24 h	4.95×10^{-4}	0.31	[60]
Zr-site substitution				
$Li_{6.25}La_3Zr_{1.25}Ta_{0.75}O_1$	1150 ℃ for 12 h	2.72×10^{-4}	0.40	[104]
$Li_{6.4}La_3Zr_{1.4}Ta_{0.6}O_{12}$	1140 ℃ for 12 h	7×10^{-4}	0.35	[105]
$Li_{6.25}La_3Zr_{1.25}Nb_{0.75}O_{12}$	1150 ℃ for 12 h	2×10^{-4}	0.42	[104]
$Li_6La_3Zr_1Sb_1O_{12}$	1100 ℃ for 24 h	2.6×10^{-4} (20 ℃)	0.38	[61]
$Li_{7.2}La_3Zr_{1.8}Gd_{0.2}O_{12}$	1220 ℃ for 36 h	2.3×10^{-4}	0.25	[106]
$Li_{6.55}La_3Hf_{1.55}Ta_{0.45}O_{12}$	1130 ℃ for 48 h	3.5×10^{-4} (22 ℃)	0.43	[107]
$Li_6La_3Zr_{1.5}W_{0.5}O_{12}$	100 ℃ for 36 h	2.08×10^{-4} (30 ℃)	0.46	[108]
$Li_{6.75}La_3Zr_{1.875}Te_{0.125}O_{12}$	1100 ℃ for 15 h	3.3×10^{-4} (30 ℃)	0.41	[109]
$Li_7La_3ZrY_{0.5}Nb_{0.5}O_{12}$	1200 ℃ for 6 h	8.3×10^{-4} (30 ℃)	0.31	[110]
$Li_{6.6}La_{2.75}Y_{0.25}Zr_{1.6}Ta_{0.4}O_{12}$	1200 ℃ for 18 h	4.36×10^{-4}	0.34	[57]
$Li_{6.4}La_3Zr_{1.4}Ta_{0.6}O_{12}$	1100 ℃ for 3 min	1×10^{-3}	—	[111]
Co-doping				
$Li_{6.20}Ga_{0.30}La_{2.95}Rb_{0.05}Zr_2O_{12}$	1100 ℃ for 24 h	1.62×10^{-3}	0.26	[112]
$Li_{6.65}Ga_{0.15}La_3Zr_{1.9}Sc_{0.1}O_{12}$	1100 ℃ for 12 h	1.8×10^{-3}	—	[113]
$Li_{5.9}Al_{0.2}La_3Zr_{1.75}W_{0.25}O_{12}$	1200 ℃ for 12 h	0.49×10^{-3}	0.34	[114]

zirconium-site doping ions if these are non-equivalent [94,95]. Therefore, by modifying the framework structure of LLZO, the ion mobility and lithium-ion concentration can be modified, which will result in different electrochemical properties [93]. This will render a solid electrolyte with higher ion conductivity and longer battery cycle performance [40].

5. 1 Control of Li-ion concentration

The concentration of Li^{2+} can be adjusted individually by adding various amounts of lithium sources, or by combining different forms and quantities of high-valent elements at the lithium-site [62]. Usually, the Li contained in the LLZO structure is classified as Li3, Li5, Li6, and Li7 based on chemical composition [34]. Garnet-type materials can accommodate cations of different valence states and different sizes without any major change in the symmetry [95–98].

As described above, lithium doping uses high valence ions to replace lithium sites, to form lithium vacancy that enables to adjust the concentration of lithium-ion (it is easier to select a particular valance state between the dopant and the Li-ion) [97]. Ion substitution can maintain the chemical balance of oxygen and reduce the Li content at the same time, or increase the concentration of Li vacancy to stabilize the c-LLZO [98,99]. The exact number of doping required has not been determined, but is generally considered between 0.125 and 0.500 mol lithium vacancy per unit [43,62]. LLZO with a higher concentration of Li vacancy (0.4–0.5 mol) exhibit maximum ion conductivity at RT [115]. It has also been reported that the incorporation of some elements into the lithium-site will change the LLZO spatial group, thus changing its mobility [93]. Thus, it is important to understand the mechanisms of doping at different sites to improve the development of LLZO SEs with higher values of Li ionic conductivity.

Single c-LLZO exists when the Li content is between 5.63 and 6.24 mol combined with an Al concentration of 0.24 mol (1.5 wt%). Rangasamy and co-workers [62] reported that as the Li^+ content increased from 6.24 to 7.32 mol, a phase transformation from cubic to tetragonal LLZO occurred, where a sample with 6.24 mol of Li^+ exhibited the highest Li^+ conductivity of 4.0×10^{-4} S·cm^{-1}. However, $La_2Zr_2O_7$ and $LaAlO_3$ were also present in the samples, contributing to the lower concentration of Li^+ than the actual value. Li^+ vacancy distribution in un-doped LLZO and Ga-doped LLZO are shown in Fig. 8. Gallium preferred to localize at the LiO_4 tetrahedron and introduced two more Li^+ vacancies around [97, 116,121]. Xiang *et al*. [116] showed that doping with Ga and different Li^+ concentrations of LGLZO ($Li_{6.4}Ga_{0.2}La_3Zr_2O_{12}$) that revealed different amounts of Li^+ in the lattice and a change of Li^+ conductivity and activation energy (E_a). With the rise of Li^+ concentration, the Li^+ conductivity rises initially and then drops. Furthermore, when the amount of Li^+ is 6.55 mol, the lithium ionic conductivity reaches a maximum of 1.09×10^{-3} S·cm^{-1}, while the sample with 6.91 mol Li^+ exhibits the minimum Li^+ conductivity of 4.3×10^{-4} S·cm^{-1}. Correspondingly, the E_a decreases initially but increases afterwards. When utilizing 6.55 mol of Li^+ the E_a reaches a minimum of 0.22 eV, compared to the sample with 6.91 mol that shows a maximum of 0.28 eV [116]. This indicates a proper Li^+ concentration improves the conductivity of Li^+ [97]. Thus, the effect of the Li^+ concentration has been widely investigated as an important factor influencing the Li^+ conductivity of LLZO. By adding different amounts of Li_2CO_3, Liu and co-workers [117] studied the effect of an excess amount of Li_2CO_3 (from 0 to 50 mol%) in starting materials when preparing LLZTO in alumina crucibles. XRD experiment rendered patterns showed that the excess of lithium salt is not crucial for achieving the cubic LLZTO, and that $LiAlO_2$ existed as the second phase in all the samples except for LLZTO–0%Li_2CO_3. In this case, the interaction between excess Li_2O_3 and alumina crucible formed the Li_2O–Al_2O_3 compounds [118]. Larger amounts of excess Li_2CO_3 resulted in better densification of the pellets and increased the ionic conductivity, indicating ionic conductivity is influenced by density. Note that these two properties are critical factors in practical applications of garnet-type materials. Zhang *et al*. [65] used 5–20 wt%

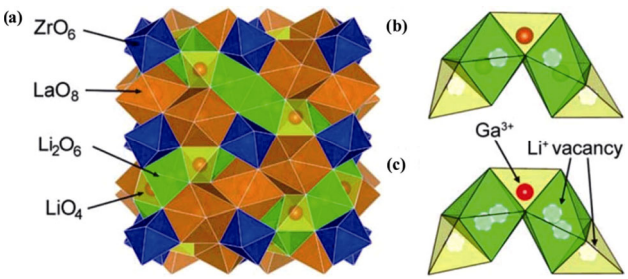

Fig. 8 (a) Crystal structure of c-LLZO. The local structure of Li^+ vacancy distribution in (b) un-doped LLZO and (c) Ga-doped LLZO. Reproduced with permission from Ref. [116], © IOP Publishing Ltd. 2019.

excess Li_2O and prepared Al-doped LLZO samples with controlled lithium-ion concentrations and less grain boundary impurities by field-assisted sintering. The authors found that as the lithium-ion concentration gradually increased from 5.80 to 7.14 mol, the ionic conductivity initially increased, reaching the maximum at 6.35 mol, which was 5.56×10^{-4} $S\cdot cm^{-1}$; after this peak, the conductivity decreased [65]. *In silico* experiments using density functional theory (DFT) and molecular dynamics (MD) calculations suggested that the introduction of 0.4 to 0.5 mol of lithium vacancies in $Li_7La_3Zr_2O_{12}$ would be more conducive to the migration of lithium ions [43]. A refined mechanism utilizing $Li_7La_3Zr_2O_{12}$ followed by neutron diffraction analyses demonstrated that that with the increase of lithium-ion concentration, the occupancy rate of lithium-ion in the octahedral vacancy gradually increased, while the occupancy rate of the tetrahedral vacancy decreased at first, followed to an increase of lithium content around 6.4 per formula unit (Fig. 9(a)) [99]. Based on the higher octahedral vacancy rate and the higher degree of lithium-ion disorder in the tetrahedral vacancy (lower tetrahedral occupancy leads to higher disorder), migration of lithium ions is favorable, so the highest lithium-ion conductivity was achieved when the ion concentration was 6.4±0.1 mol. Aliovalent doping is commonly used to increase the Li content to optimize the ionic performance, for example in $Li_7La_3Zr_2O_{12}$, $Li_{3+x}Nd_3Te_{2-x}Sb_xO_{12}$, and $Li_5La_3(Ta/Nb)_2O_{12}$ [118].

A summary of the highest conductivities of un-doped, doped, and multi-doping of LLZO substitutions reported in the literature is presented in Fig. 9(b) [119]. Briefly, the highest Li-ion conductivity was achieved by the lattice parameters in the range of 12.91–12.98 Å, at Li contents between 6.1 and 6.8 per formula unit (highlighted on the red circle). Substitutions that result in lattice parameters outside this range show lower total Li-ion conductivity. The presence of an optimum lattice parameter was observed when Nb was replaced by Zr, and alkali earth metals of different ion sizes (Mg, Ca, Sr, and Ba) were replaced by La in the LLZO. The optimal lattice parameters of LLZO have been studied systematically by Kihira *et al.* [94]. The data show no

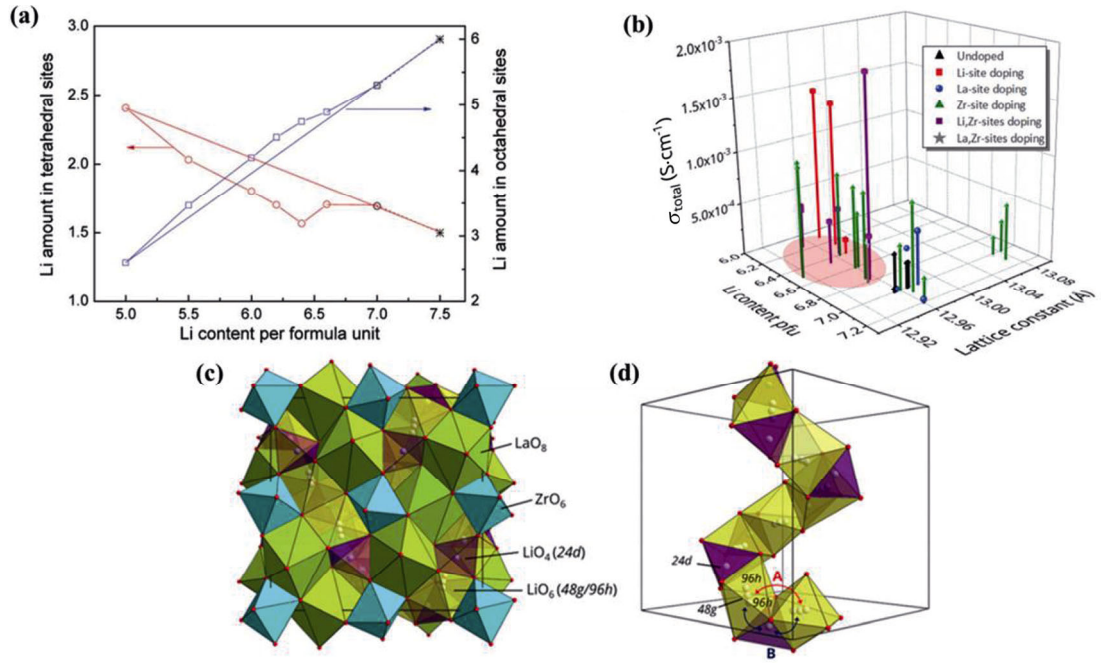

Fig. 9 Different amounts of Li concentration, conductivity, and the Li migration of c-LLZO. (a) Variation with Li concentration of 24d-A and bridging octahedral occupancies obtained from neutron diffraction data. Reproduced with permission from Ref. [99], © American Chemical Society 2011. (b) Lithium-ion conductivity vs. nominal lithium content per formula unit (pfu) and lattice constant of LLZO-based garnets. The highest conducting compositions are clustered at lithium contents between 6.1 and 6.8 per formula unit (units) and lattice constants between 12.91 and 12.98 Å. (c) Crystal structure of cubic $Li_7La_3Zr_2O_{12}$ and (d) Wyckoff positions of the Li-ions. The centers of tetrahedral and octahedral sites are noted as 24d and 48g sites, respectively. The 96h sites are slightly displaced off by the 48g sites. LiO_6 and LiO_4 connection and the two possible Li migration pathways (A and B). Path B is the most likely mechanism of Li migration in LLZO. Reproduced with permission from Ref. [119], © The Royal Society of Chemistry 2019.

change in the Li content in any component related to element doping; the group also described optimum lattice constants are between 12.94 and 12.96 μm, which are consistent with other reports for the garnet-type SEs, where the reported optimum lattice parameter ranged from 12.90 to 12.95 Å [120]. The highest conductivity obtained so far was 2.06×10^{-3} S·cm^{-1} at RT for $Li_{6.55}Ga_{0.15}La_3Zr_2O_{12}$ [121], which is around an order of magnitude higher than the first LLZO synthesized in 2007 (3×10^{-4} S·cm^{-1} at RT) [33]. These differences can be explained by the fact that simple lattice expansion may lead to the expansion of Li-ion hopping interstices, which eventually leads to high ion conductivity [116]. In fact, computational analyses have shown that the extended lattice provides slight improvements in conductivity [123]. Theoretically, the evidence suggests various Li-diffusion pathways to improve conductivity. For instance, *in silico* calculations and Li NMR suggest a mechanism by which the 24d Li-ions are immobile and Li migrates by hopping between the octahedral sites in LLZO with Li contents under 5 per formula unit [122–124]. *Ab initio* calculations support two pathways of Li-ion migration in cubic garnets that consider Li contents over 5 units per formula [34]. As shown in Fig. 9(d), in pathway A the Li migrates via the interstice between neighboring octahedral sites, by passing their common tetrahedral neighbor. In pathway B the Li-ions move through the famous shared triangular "neck" of octahedral and tetrahedral sites in the framework. The Li-ion migration in path A is favored when Li^+ content is lower ($Li_5La_3Nb_2O_{12}$) and with an activation energy of 0.8 eV, while path B selects high Li^+ content ($Li_7LaZr_2O_{12}$) with the activation energy of 0.26 eV [25,31].

It has been postulated that the Li vacancy concentration is a crucial factor in the ionic conductivity of LLZO [118]. LLZO has two stable sites: a tetrahedrally coordinated one (Li1) and an octahedrally coordinated one (Li2). The migration between sites of the Li-ion is through a triangular "neck". The size of the octahedron/tetrahedron and the neck also affects the conductivity by changing the site's energies and/or the neck energy [97]. Studies on the channel size have attempted to elucidate whether a larger or smaller channel width is beneficial for ion transport [124]. This is an important consideration, as channel size has been defined as the correlation of the size of the lattice with the conductivity [120]. Therefore, large changes in the conductivity may indicate that separate control of the two structural aspects is essential for controlling Li-ion diffusion [125]. DFT calculations, and a variety of experimental techniques like synthesis methods, neutron diffraction, high resolution X-ray diffraction (XRD), Raman measurements demonstrated a relationship between structure and stoichiometry. These two features offer the possibility of controlling the ionic conductivity of doping LLZO, suggesting that co-doping optimizes the Li vacancy concentration and the lattice size simultaneously [126]. A study using neutron diffraction and theoretical calculations showed the influence of doping LLZO, on the two Li sites (Li1 and Li2) and the triangular "neck" window between them change [126]. The neck size increased when Ta doping increased. Neutron diffraction (ND) analyses showed the Ta ion pulls the neighboring O ions more tightly than the Zr ion. The TaO_6 octahedra and the LaO_8 contribute cooperatively to decrease the lattice parameter, while slightly increasing the volume of Li sites [126]. Doping LLZO with supervalent ions like Al, Ta, Nb, and Ga can create and balance the Li vacancies and thereby produce a cubic lattice improving the ionic conductivity [104–106,111]. It is accepted that dopants, such as Al^{3+}, of the sintering process from the crucible can stabilize the cubic phase of LLZO [55]. Geiger *et al.* [59] studied the influence of Al doping and sintering temperature in the structure of $Li_7La_3Zr_2O_{12}$. The crystal structure of LLZO allowed identifying two Li binding sites without doping and low sintering temperature, which constituted the tetragonal phase. Kotobuki *et al*. [127] reported that Al_2O_3 is an effective sintering additive, as the sintering temperature was reduced and the impurity formation of $La_2Zr_2O_7$ was inhibited by this compound. Doping with Al compounds can expand the lattice filling with tetrahedral Al^{3+} ions, increasing the bottleneck size [55,58,62]. The position lattice was studied by density functional theory and NMR of the Al in the c-LLZO; the data showed Al^{3+} could have a number of slightly different local 4-fold coordinations around 24d and 96h sites in cubic LLZO: these suggest the facility of garnet structure to create intersices and enhance the Li^+ diffusion [127–129]. Researchers have used computational and experimental results to understand the stoichiometry and crystal structure, and enhance the optimization of LLZO using elemental substitution. Study about the performance the Li-ion conductivity has been the main goal to develop garnet solid electrolytes commercially available for battery fabrication.

5. 2 Regulation of ion mobility

Li-ion mobility is considered as one key requirement for a good electrolyte. Although high mobility of Li^+ in solid materials has been encountered at elevated temperatures, room-temperature mobility and chemical stability remain as significant challenges in the field [130]. These issues can be solved by element doping, at the three sites possible of LLZO: Li site, La site, and Zr site. As we mention in the previous section, lithium-site doping was only used to regulate the concentration of lithium-ion. Al^{3+} is widely used as a common element to control lithium-ion concentration and stabilize cubic lattice. Huang and coworkers [131] used the Al-doped LLZO lithium site, and obtained an ionic conductivity of 3.6×10^{-4} S·cm^{-1} at RT. However, in recent years, researchers have discovered that certain lithium-site doping elements can not only regulate the concentration of lithium ions and stabilize LLZO in their cubic phase, but also increase the mobility of Li ions by changing their space group, thereby improving the lithium-ion conductivity [131–134]. For instance, the compound $Li_{6.25}Ga_{0.25}La_3Zr_2O_{12}$ exhibited a conductivity of 1.46×10^{-3} S·cm^{-1} at RT through Ga doped on the Li site of LLZO, resulting in a mobility for $Li_{7-3x}Ga_xLa_3Zr_2O_{12}$ of 10^{-8}–10^{-7} cm^2·V^{-1}·s^{-1} at 60 ℃. This is significantly higher than the mobility observed for W-doped LLZO (10^{-9} cm^2·V^{-1}·s^{-1}) [93]. Calculations and *in silico* simulations by Garcia Daza and co-workers [132] proposed that in the Al-doped LLZO, the Li ions near the Al ion are unable to migrate; conversely, the Li ions near the Ga ions in the Ga-doped LLZO are mobile. Further XRD analyses of Ga doped LLZO by single crystal particle, demonstrated that the space group of the cubic phase structure Ga doped LLZO is $I-43d$, which is different from the traditional cubic phase LLZO, $Ia-3d$ space group [133]. This structure and the cubic phase of LLZO $Ia-3d$ space group are all formed by ZrO_6 octahedron and LaO_8 dodecahedron, and Li ions filled the vacancies [28]. The difference is that Li1 (24D) tetrahedral vacancy and Li2 (96h) octahedral vacancy is formed by the cubic phase LLZO of the $Ia-3d$ space group, while Li1 (12a) and Li2 (12b) occupy the tetrahedral vacancy, and Li3 (48e) the octahedral vacancy forming the cubic phase of LLZO of the $I-43d$ space group (Fig. 10).

Rettenwander and coworkers [101] developed the $Li_{6.4}Al_{0.2-x}Ga_xLa_3Zr_2O_{12}$ compound and found that increasing the Ga content favored the ionic conductivity,

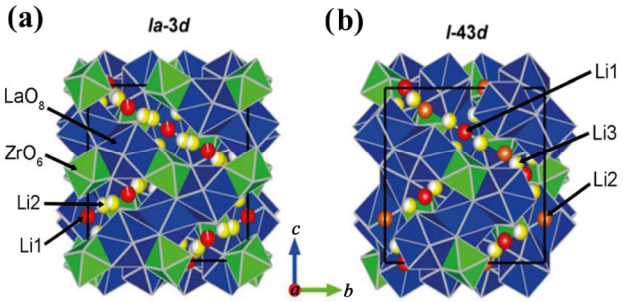

Fig. 10 Crystal structure of Ga-stabilized c-LLZO with $x_{Ga}=0.10$ and space group of (a) $Ia-3d$. Blue dodecahedra represent 8-fold coordinated La^{3+} (at the Wyckoff position 24c), green octahedra 6-fold coordinated Zr^{4+} (16a). The red spheres correspond to tetrahedrally coordinated Li^+ at the 24d (Li1) site, yellow spheres correspond to distorted 4-fold coordinated Li^+ at Wyckoff position 96h (Li2) (b), and with $x_{Ga}=0.30$ and space group $I-43d$. Blue dodecahedra represent 8-fold coordinated La^{3+} (at the Wyckoff position 24d), green octahedra 6-fold coordinated Zr^{4+} (16c). The red spheres correspond to tetrahedrally coordinated Li^+ at the 12a site (Li1), orange spheres represent tetrahedrally coordinated Li^+ at the 12b site (Li2), and yellow spheres correspond to distorted 6-fold coordinated Li^+ at Wyckoff position 48e (Li3) (b). Reproduced with permission from Ref. [133], © American Chemical Society 2016.

and when it exceeded a critical amount of 0.15 Ga per formula unit (pfu), the space group of cubic LLZO changed from $Ia-3d$ to $I-43d$. On the other hand, Wagner *et al*. [100] found that doping with Fe renders a similar crystal-chemical behavior to Ga-doping. When Fe doping at 0.18 and 0.25 pfu the cubic LLZO space group obtained was also $I-43d$ and the ionic conductivity of the sample of 0.18 pfu reached a maximum of 1.38×10^{-3} S·cm^{-1}. Studies regarding the doping of LLZO lithium sites with Al, Fe, and Ga focused on the influence of the change of space group on the migration of LLZO lithium ions by neutron diffraction [134]. The analyses demonstrated that the cubic phase LLZO with space group $I-43d$ has multiple Li-ion migration channels, and the Al ion with space group $Ia-3d$ cubic phase LLZO will not block the Li ion migration channels, resulting in lower activation energy and improved Li ion migration (Fig. 11).

5.2.1 Change of bottleneck size on mobility

The structure of LLZO is formed by the common edge of ZrO_6 octahedron and LaO_8 dodecahedron, where Li ions filled the voids in the framework, allowing the size of the lithium migration channel to be modified by

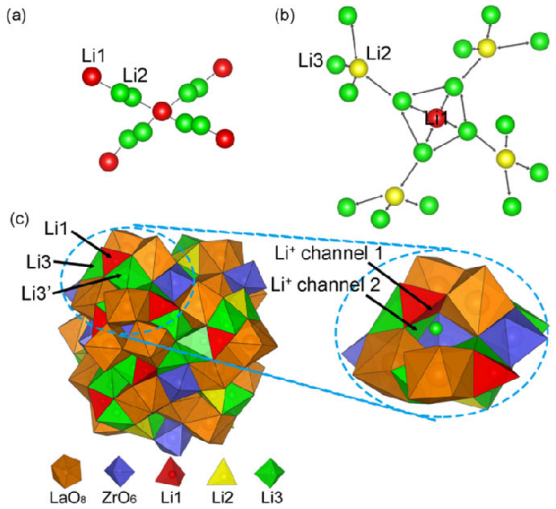

Fig. 11 Lithium-ion migration pathway of cubic LLZO with the space group of (a) $Ia-3d$ and (b) $I-43d$, and (c) the migration pathway of lithium-ion from Li3 to Li. Reproduced with permission from Ref. [134], © Elsevier Ltd. 2020.

doping at the La or Zr sites (Table 3) [57,60,61,75, 93,95,99–114]. There are few reports about lanthanum doping. The large size of lanthanum ions and the strong influence on the crystal structure of LLZO make it difficult to find suitable doping ions for La site [60,95]. However, some studies showed that doping with Sr at the La-site the ionic conductivity at RT of LLZO increased from 2.1×10^{-4} to 4.95×10^{-4} S·cm^{-1} [60]. The development of the $Li_7La_3M_{0.25}Zr_{1.75}O_{12}$ (M = Ge^{4+}, Ti^{4+}, Sn^{4+}, Hf^{4+}) compound allowed to investigate the influence of the Zr doping ion radius on the bottleneck size and activation energy of the Li-ion migration channel by synchrotron radiation [50]. The data showed that by increasing the Zr doping ion radius, the M–O bond length increased, as well as the Li vacancy polyhedron with the same edge increased, and the bottleneck size (the circumscribed radius of the smallest triangle of the migration channel) [104–111]. Consequently, as the M–O bond length rises, the volume of the MO_6 octahedron increases, so do the cell parameters (Fig. 12(a)). Another cation that has been investigated in La-site doping on LLZO is Ce^{4+}. Ce^{4+} concentrations over 0.2 mol stabilized the LLZO to the cubic phase at RT; however, its ionic conductivity was only 1×10^{-4} S·cm^{-1} [95]. There are further reports on Zr-site doping, and there are several elements that can be integrated into it and enhance its ion conductivity. Doping the Zr-site of LLZO with alkaline earth ions (Mg, Ca, Sr, Ba) into the octahedral sites (Zr^{4+}) instead

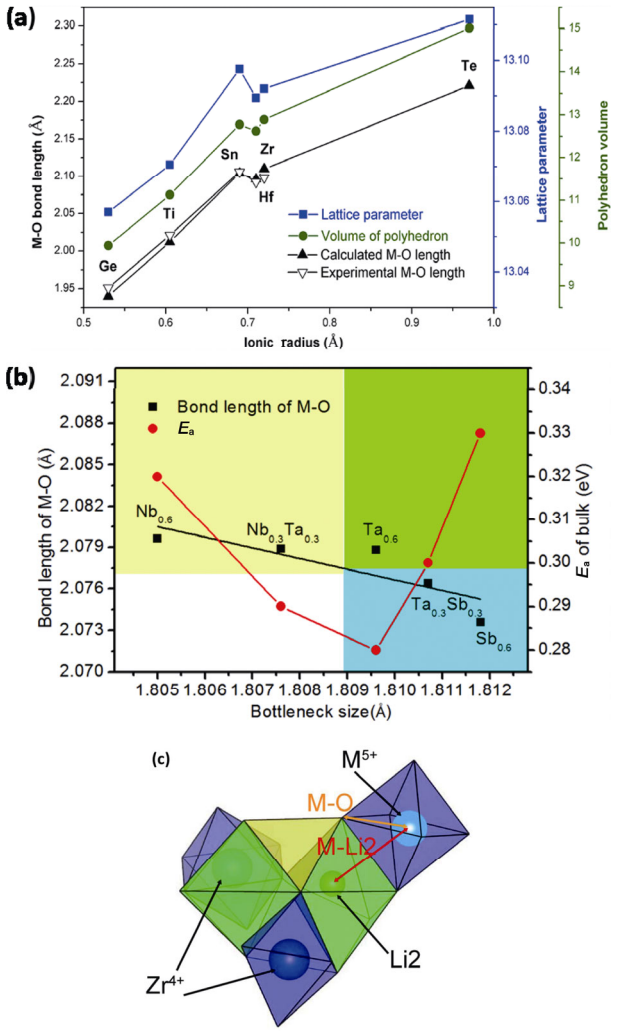

Fig. 12 Li^+ migration, bottleneck size, and larger bond lenght of M–O: (a) M–O bond length, lattice parameter, and calculated MO_6 polyhedral volume of M-doped LLZO dependent on the doping ionic radius. Reproduced with permission from Ref. [140], © Elsevier Ltd. 2017. (b) Dual regulation of E_a by bottleneck size and bond length of M–O. (c) Structural representation of the bond length of M–O and Li^+ migration channel. Reproduced with permission from Ref. [139], © The American Ceramic Society 2019.

of La^{3+}-sites resulted in a relaxed the crystal structure with enlarged the bottleneck, but improved ionic conductivity [135]. Bachman *et al.* [136] summarized published literature on findings by several groups and proposed a general rule applicable to all solid electrolytes. The proposal is that the size of the Li-ion migration channel and the cell parameter volume increase if the doping ion radius in the framework structure increases, while the activation energy decreases facilitating the lithium-ion migration. Consistently, Wang and coworkers [137] calculated the crystal

framework and the diffusion coefficient of Li-ion by using the first principles [137]. They found that with the increase of framework volume, the ion diffusion coefficient increases. Simulations of a cubic phase LLZO model where the cell volume was changed by adjusting the external force at 1000 K, showed that the conductivity of Li-ion was enhanced as the cell parameters were increased [32]. However, variations of metal concentrations also rendered changes in sizes. Nemori *et al.* [104] used 0.75 mol of Nb^{5+} (0.69 Å) and Ta^{5+} (0.64 Å) into Zr^{4+} (0.72 Å) to prepare $Li_{6.25}La_3Zr_{1.25}M_{0.75}O_{12}$ (M = Nb, Ta), and obtained larger ions. The unit cell parameters (12.909 nm) and ion conductivity (2.03×10^{-4} S·cm^{-1}) of Nb^{5+} doped LLZO were smaller than Ta^{5+} doped LLZO (12.912 nm, 2.72×10^{-4} S·cm^{-1}) [104,105]. When Ca and Ta were used to dope La- and Zr-sites to control the size of the Li-ion migration channels, it was observed a decrease in the lattice parameters with the increase of co/doping content, suggesting that the Li^+ migration path size of LLZO decreases ahead [138]. The study also showed an initial drop in the activation energy which gradually increases at a later time. The study concluded that the movement of Li ions is not conducive to the movement of too large or too small migration channels [135,138]. Xiang and co-workers [139] developed the $Li_{6.4}La_3Zr_{1.4}M_{0.6}O_{12}$ (where M represents Sb, Ta, Nb) compound, and investigated changes in particle sizes by neutron diffraction. The study showed that the pentavalent ions are doped by a stronger inter-particle Coulomb force produced in the reaction. As shown in Fig. 12(b) the radius of the hetero ions, the length of the M–O, and the distance between the lithium-ion and the migration channel increase, while the length of the La–O bond is compressed, and the bottleneck size and unit cell volume gradually decrease [139]. Thus, the activation energy is coordinated by the size of the bottleneck and the M–O bond length [139,140]. On the other hand, the bond length of M–Li2 became larger with the increase of radius of doping ions, consistently with the increase of M–O [139]. Figure 12(c) shows the structural representation of the bond M–O length indicating the difference between the M^{5+} and Li^+ migration channel.

5.2.2 *Coordinated regulation of lithium-ion concentration and mobility*

As discussed above, the ionic conductivity of LLZO can also be improved by simultaneously adjusting the Li-ion concentration and changing the skeleton and then adjusting the mobility. When using the heterovalent ion Ta to dope Zr-sites and concurrently modulating the Li-ion concentration and migration channel size, an inverse correlation was found. The increase in Ta doping (up to 0.6 mol) leads to a drop in the concentration of Li-ion and reduction of the migration channel size, and the activation energy decreased resulting in the ionic conductivity to be 1×10^{-3} S·cm^{-1} at RT [111]. A cubic phase $Li_{6.10+2y}Ga_{0.3}La_{3-y}Rb_yZr_2O_{12}$ compound where the Rb concentration was increased, resulted in an increased concentration of Li-ion and migration channel size; the activation energy increases until the content of Rb doped is 0.05 mol. Under these conditions, the activation energy is the lowest, and the ion conductivity is high as 1.6×10^{-3} S·cm^{-1} [112]. Buannic *et al.* [113] reported the cubic phase of $Li_{6.55+y}Ga_{0.15}La_3Zr_{2-y}Sc_yO_{12}$, where the increase of Scandium (Sc) doping increased the concentration of the Li-ion concentration and the migration channel size, similarly to other metals; in this case the activation energy exhibited an initial decreased followed by an increase. A concentration of 0.1 mol of Sc resulted in the lowest activation energy and an ion conductivity of 1.8×10^{-3} S·cm^{-1}. Under these conditions, the LLZO structure is most stable when the occupancy rates of Li1 and Li2 are 46% and 47%, respectively [47]. Zeier [120] has shown that controlling the unit cell parameters in the $Li_6MLa_2Ta_2O_{12}$ compund and substituting the La-site leads via chemical pressure of the Li–O polyhedra pathways, ultimately lead to a change of the Li^+ mobility. Thus, the evidence supports a mechanism by which co-doping can stabilize the cubic junction and can effectively promote the transport of Li ions.

DFT was used to measure the possible locations of selected dopants in the LLZO, and was proven to be a good method for finding LLZO-based SE with excellent performance [141]. In this case the doping elements included Al, Fe, Ge, and Ga to replace Li, and Sr, Y, and Ce to replace Zr. All of these are amongst the most common elements that can be incorporated to LLZO (Table 3). Al^{3+} promotes the lattice distortion allowing 3 Li vacancies and the migration in the tetrahedron site is more difficult for Li-ions [129]. Although the occupancy of the tetrahedron site with Al^{3+} has a blocking effect on the Li-ion conduction, it rendered a consistent increase of the bottleneck size [74,156]. Furthermore, the introduction of Al^{3+} in the crystal structure increased the conductivity [73–75,82]. Thus, it is essential to

regulate the concentration rate during element doping, since these may alter the Li concentration [94,103].

Recent work targeted the substitution of Ga^{3+} on the tetrahedral Li site [93]. This substitution also increased the ionic conductivity. The crystal structure of c-LLZO showed the local structure of the molecule with increased conductivity [116,121]. This was associated with the enhanced disorder, the transport route change from 96h→24d→96h to 48e→12a (12b) →48e and 48e↔48e and the Li content on the mobile octahedral site [116,142]. The amount of Li content of LLZO with the highest conductivity was 6.1–6.8 per formula unit, lower than the theoretical limit of 7.5 per unit [143]. The range of Li concentrations in the $Li_{6.55}Ga_{0.15}La_3Zr_2O_{12}$ compound represents the highest ionic conductivity of 2.06×10^{-3} S·cm^{-1} at RT [120]. In addition, MD simulations calculated by Jalem *et al*. [144] suggested that the ionic conductivity of $Li_{7-3x}Ga_xLa_3Zr_2O_{12}$ (x = 0.02) was 6.08×10^{-3} S·cm^{-1}, which is one of the highest values reported for LLZO electrolytes. Nevertheless, it is still lower than liquid Li electrolytes (~1×10^{-2} S·cm^{-1} at RT) [136]. The size of the bottleneck in the study of the LLZO solid electrolyte structure [139], precisely refers to the circumscribed circle radius of the smallest triangle of the Li-ion migration channel. The radius of the circumscribed circle has a major effect on the migration of Li. As we know, ZrO6 octahedron and LaO8 dodecahedron form the framework structure of LLZO through the common edge, where Li ions fill the voids in the framework [140]. Therefore, modifying the shape of their structure and the size of bottleneck by doping at the La- or Zr-sites results in an altered Li-ion migration channel [138–140,144].

6 Applications of garnet-based LLZO in all-solid-state lithium batteries

In recent years, significant improvements have been made to the performance of ASSLBs using LLZO electrolytes [36,40,79]. Research has addressed problems associated with the electrode/electrolyte interface and increasing their energy and power densities (Fig. 13) [149–156]. The high interfacial resistance between electrolyte and electrode has become an urgent task to solve, as it possesses significant influence on the

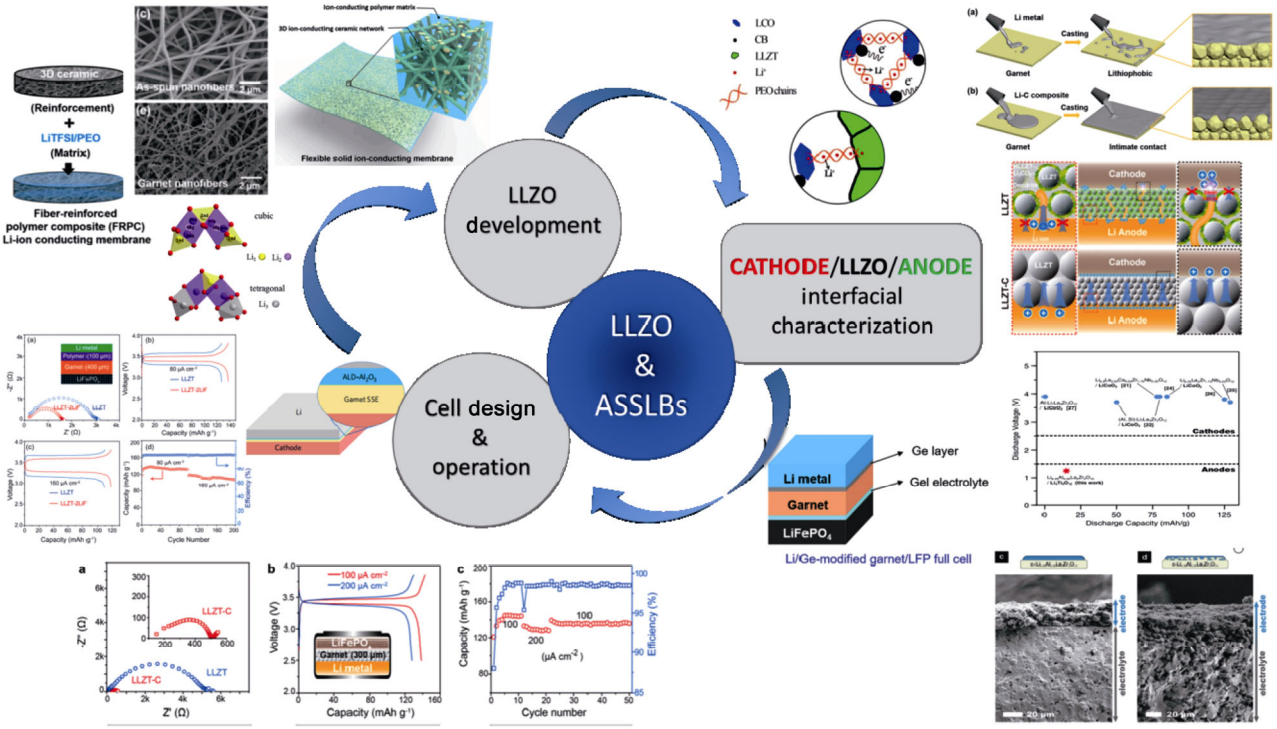

Fig. 13 Fundamentals for all-solid-state batteries for LLZO solid electrolytes: development, interfacial characterization, cell design, and operation. Reproduced with permission from Ref. [149], © WILEY-VCH Verlag GmbH & Co. KGaA, Weinheim 2017; Ref. [150], © Macmillan Publishers Limited, part of Springer Nature 2017; Ref. [151], © WILEY-VCH Verlag GmbH & Co. KGaA, Weinheim 2016; Ref. [152], © American Chemical Society 2018; Ref. [153], © WILEY-VCH Verlag GmbH & Co. KGaA, Weinheim 2019; Ref. [154], © The Author(s) 2016; Ref. [155], © The Author(s) 2017; Ref. [156], © Elsevier B.V. 2015.

overall performance of the battery [8]. The study of electrochemical reactions is a major research area to understand the contact interphase of the solid–solid electrolyte–electrode interface, as insufficient contact between these leads to the formation of a solid electrolyte interface (SEI) [146]. Li ions diffuse from electrolyte to electrode through their interconnected region, and redox reactions with active materials and electrons happen at the electrolyte–electrode interface [145,150]. To ensure that the charge transfer reaction continues steadily, it is important to maintain an efficient solid–solid electrolyte–electrode interface in the battery all the time [149]. A major challenge to be solved is how to improve the ionic conductivity at the electrode–solid electrolyte interface [150,151]. Despite that, studies focusing on Li-ion migration, diffusion behavior across the interface, and understanding the interface at the sub-molecular and atomic-level, are still limited [152]. Another important factor affecting the ionic interphase is the mechanical properties of the SEs in terms of fragmentation of electrode materials [145]. The interfacial contact between the active electrode and the SE represents critical elements during battery design, assembly and manufacturing, and overall battery performance [40]. Table 4 lists the fundamental parameters for the performance of ASSLBs. There are two basic strategies to use LLZO as a solid electrolyte for ASSLBs. One is used LLZO-based solid electrolytes as bulk ceramic [119]. However, they usually exhibit larger interfacial resistance, poor battery performance due to weak contacts between the electrode–electrolyte, side reactions with the electrolytes, and moisture/CO_2, which lead to low battery performance [149–152]. Nevertheless, developing a composite solid electrolyte (SCE) by combining LLZO with a solid polymer electrolyte (SPE), has become a research spotlight due to the advantages these represents [146–148]. For instance, SCEs exhibit a wide electrochemical window, favorable mechanical strength, stability, and remarkably improved ionic conductivity [157,158]. On the other hand, challenges exist on the interfacial resistance of each material. According to the previous development of the garnet-type LLZO solid electrolytes, it is well known that the high conductivity is a necessary but an insufficient property to design future ASSLBs.

6. 1 LLZO-based all-solid-state lithium batteries

LLZO electrolytes have a high elastic modulus with small contact area between them and the electrodes [164]. It is possible that structural defects, such as voids and cracks at the interface, or even a third phase during the charge and discharge cycles impair the performance of the device [165]. The unideal interfacial contact leads to a high interface resistance, thus reducing the Li^+ migration dynamics at the interface [161]. One of the first studies with LLZO-based ASSLBs and Li showed that Li-ions move through LLZO-based electrolytes without Li accumulation on the surface of LLZO [165], where the interfacial issues result in a low discharge capacity of 15 $\mu Ah \cdot cm^{-2}$ [35]. An alternative cell was assembled with LCO|LLZO–Nb|Li, and showed stable cycling performance and comparable interfacial impedances with traditional batteries; 98% of the initial capacity was retained after 100 cycles [166]. Another strategy to overcome interfacial issues was the development of a co-sintering model of LLZO with $LiCO_2$ not having side reactions [167]. The performance of the battery was successful; this device charged and discharged with specific capacities of 98 and 78 $mAh \cdot g^{-1}$ [167]. Using an interface-engineered $Li_{6.25}Al_{0.25}La_3Zr_2O_{12}$–$Li_4Ti_5O_{12}$ the ASSLB showed an enhanced Li-ion transport at the anode electrode–electrolyte interface, and the SE had a relatively higher discharge rate of 8 $A \cdot kg^{-1}$. Another effort to improve the performance of the battery demonstrated that in $Li4Ti_5O_{12}$|porous LLZO-dense LLZO, the Li shows a performance of almost 25 cycles with a discharge capacity of 15 $mAh \cdot g^{-1}$[151]. In an ASSLB assembled with a mixture of $LiMn_2O_4$ and LLZO–B_2O_3, the performance of the specific capacity was 102.6 $mAh \cdot g^{-1}$ on the first cycle, and kept a capacity retention of 94% after 20 cycles [168]. Using LLZO nanoparticles, Yan and co-workers [169] fabricated an ultrathin solid electrolyte film and the Li|LLZO|$LiFePO_4$ battery presented a discharge capacity of 160.4 and 136.8 $mAh \cdot g^{-1}$ in the first cycle and 100th cycle at RT, respectively [169]. This work demonstrated a high performance of SE layer with micrometer thickness that is suitable for applications of ASSLBs. From experimental and computational analyses, it was concluded that LLZO is favorable for ASSLBs with high energy and power densities [153,155]. However, interfacial issues and long resistances with anode and cathode electrodes are the bottleneck headache; especially the grain boundary chemistry of LLZO needs to be studied for further application of LLZO- based solid electrolytes.

Table 4 Fundamental parameters for ASSLBs using garnet LLZO solid electrolyte

Solid electrolyte						Battery performance			
Composite solid electrolyte	Ionic conductivity ($S \cdot cm^{-1}$)	Cathode material	Electrochemical window (V)	t_{Li+}	ARS ($\Omega \cdot cm^2$)	Potential range (V)	Cycle performance	Capacity ($mAh \cdot g^{-1}$)	Ref.
Ge-modified $Li_{6.85}La_{2.9}Ca_{0.1}Zr_{1.75}Nb_{0.25}O_{12}$	1.23×10^{-4}	$LiFePO_4$	—	—	115	2.4–4	≈ 100% (0.1 C, 100 cycles)	140 (1 C)	[149]
PEO_{15}–$LiClO_4$ + $Li_{6.4}La_3Zr_{1.4}Ta0._6O_{12}$ (30.1 wt%)	4.8×10^{-4} (60 ℃) 1×10^{-3} (80 ℃)	$LiFePO_4$	4.6	0.16	75	2.5–4	83% (1 C, 500 cycles)	~140 (1 C, 60 ℃) ~80 (4 C, 60 ℃)	[157]
PEO_{18}–LiTFSI + 10%SN + $Li_7La_3Zr_2O_{12}$	1.19×10^{-4} (25 ℃) 3.69×10^{-4} (60 ℃)	$LiFePO_4$ $LiCoO_2$	5.5	0.41	—	2.8–4	95.2% (0.5 C, 100 cycles) 80% (1 C, 500 cycles)	157.9 (0.2 C, 60 ℃) 145.6 (0.5 C, 60 ℃)	[147]
PEO_8–LiTFSI + $Li_{6.4}La_3Zr_{1.4}Ta_{0.6}O_{12}$ (10 wt%)	1.17×10^{-4} (30 ℃) 1.59×10^{-3} (80 ℃)	$LiFePO_4$	5	—	—	2.9–3.8	93.% (0.2 C, 100 cycles)	149.1 (0.1 C, 55 ℃) 148.6 (0.2 C, 55 ℃)	[148]
PEO_{18}–LiTFSI + SN (10 wt%) + $Li_{6.4}La_3Zr_{1.4}Ta_{0.6}O_{12}$ (60 wt%)	1.22×10^{-4} (30 ℃) 9.70×10^{-4} (60 ℃)	$LiFePO_4$	5.5	0.410	—	2.8–4	95.4% (0.2 C, 50 cycles) 98.% (0.5 C, 200 cycles)	150.8 (0.2 C, 60 ℃) 147.3 (0.5 C, 60 ℃)	[158]
PEO_{16}–LiTFSI + 1D nanowires $Li_7La_3Zr_2O_{12}$ (10 wt%)	2.39×10^{-4} (RT) 1.53×10^{-3} (60 ℃)	$LiFePO_4$	5.5	—	—	2.8–4.2	97.4 (0.5 C, 70 cycles) 158.7 $mAh \cdot g^{-1}$ after 80 cycles at 0.1 C and 45 ℃	163 (0.5 C, 60 ℃) 177.4 (0.1 C, 60 ℃)	[159]
PEO_{10}–$LiClO_4$ + 2D nanosheet $Li_{6.5}La_3Zr_{1.5}Nb_{0.5}O_{12}$ (15 wt%)	3.6×10^{-4} (RT)	$LiFePO_4$	—	—	—	2–4	97.5% (0.05 C, 30 cycles)	98.1 (0.05 C, 40 ℃)	[160]
Cross-linked PEO/LLZT–2 wt% LiF $Li_{6.5}La_3Zr_{1.5}Ta_{0.5O12}$	5.2×10^{-4} (60 ℃)	$LiFePO_4$	—	—	385	2.8–3.8	84.51% (80 μA/cm², 100 cycles)	142 (80 μA/cm², 65 ℃) 128 (160 μA/cm², 65 ℃)	[161]
PEO/LLZTO $Li_{6.4}La_3Zr_{1.4}Ta_{0.4}O_{12}$	—	$LiFePO_4$	4.2	—	—	2.5–4.2	~140 (0.2 C, 90 ℃)	135 $mAh \cdot g^{-1}$ (200 th, 0.2 C)	[162]
PPC-LiTFSI (4:1) + $Li_{6.75}La_3Zr_{1.75}Ta_{0.25}O_{12}$ (5 wt%)	5.2×10^{-4} (20 ℃)	$LiFePO_4$	4.6	—	—	2.5–4	120 (0.1 C, 0 ℃) 123 (0.1 C, 20 ℃) 120 (0.2 C, 20 ℃)	95% (1 C, 200 cycles, 20 ℃) 95% (1 C, 800 cycles)	[163]

6.1.1 Interfacial issues between LLZO/anode

Li-metal is the most attractive anode material possess a high theoretical specific capacity (3860 $mAh \cdot g^{-1}$), the lowest redox potential (–3.040 V vs. standard hydrogen electrode), and low density (0.534 $g \cdot cm^{-3}$) [170]. Insufficient contact between electrolyte and electrodes leads to form an SEI on Li metal anode, decreasing the capacity and low coulombic efficiency (CE) [171]. Also, irregular deposition of Li metal can form Li dendrites, go through the current collectors, and mix with the products of reactions happening in the SEI during the cycling, resulting in active material losses, increasing impedance, and with the possibility of short circuit, affecting the performance of the ASSLBs [180]. The area-specific resistance (ASR) is used to define impedance, which depends on the area of ionic contact between the solid electrolyte and the active material (electrodes) [189–191]. *In situ* computational analyses of LLZO suggest an excellent electrochemical stability with Li metal [21]; however, experimental evidence reports high ASR, and thus, many strategies have been developed to improve the contact of LLZO and Li [177]. Atomic layer deposition (ALD), sputtering, heat or wet treatment, evaporation, polishing, among others [149,153,164,171–174] point towards the challenges and requirements for long-term stability, lifetime (in terms of the number of discharge-charge cycles of the battery), minimizing the Li dendrites, and reducing the costs of processing technologies to be consider at the Li|LLZO interface.

Research revealed a slight thermodynamic stability of $Li_7La_3Zr_2O_{12}$ although at very low potentials (0.05 V vs. Li^0) and with low reaction energies (20 meV per atom) [21,175]. So, the observed stability of LLZO electrolytes against Li^0 is likely the result of the kinetic stabilization [175]. One of the simplest ways to improve the interface contact is Li heating and melting; after heating, the ASR is lower to 25–28 $\Omega \cdot cm^2$ at RT [176]. The formation of the Li_2CO_3 passivation layer inhibits the adhesion of Li to the surface of LLZO [89]. The interfacial instability of the Li interface, which is determined by *in-situ* electron microscopy when LLZO is in direct contact with Li metal [177], showed that upon contact with Li, a layer of t-LLZO is formed in the interphase (~5 unit cells), and prevents full degradation of c-LLZO while promoting the Li^+ transport.

A strategy using heat or wet treatment by Zhou *et al.* [237] incorporated a wet process technology to treat Zn. A $(NO_3)_2$ solution is uniformly distributed on the surface of LLZO and thermal decomposition results in the formation of ZnO; thus, the ASR between Li and LLZO is also reduced effectively. Sharafi and co-workers [178] used the wet method before heating the Li metal supplemented by glycol-based additives, as strategies for polishing the LLZO surface. As a result the interface resistance of Li LLZO was reduced to 2 $\Omega \cdot cm^2$. Polishing is another method used to improve the interface contact (Figs. 16(a) and 16(b)). Fu and co-workers [179] polished and ground LLZO

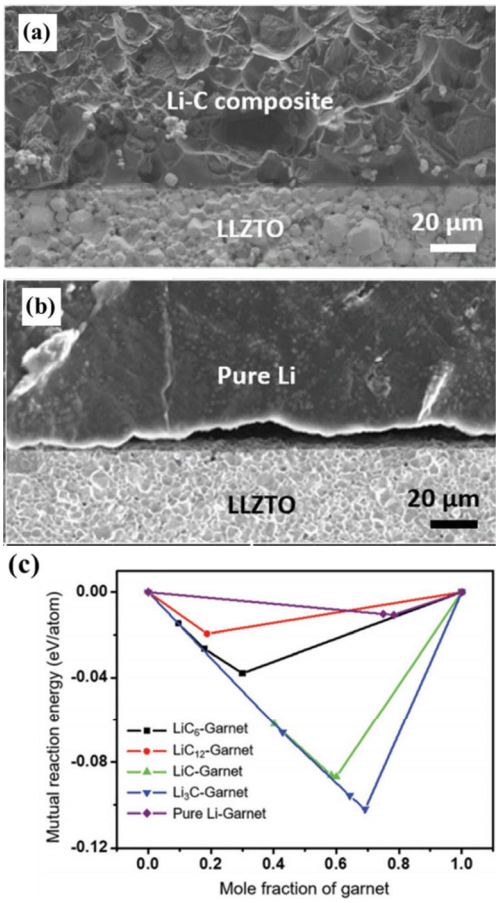

Fig. 14 Improvement of Li-anode interphase. SEM images of (a) Li–C/garnet and (b) pure Li/garnet interfaces. (c) Calculated mutual reaction energy of Li–C composite/garnet interface and pure Li/garnet interface. The Li–C composite and garnet show favorable reaction with mutual reaction energy of −20 to −100 meV per atom, whereas pure Li and garnet exhibit a less favorable mutual reaction, indicating the introduction of graphite into lithium could promote the interface. Reproduced with permission from Ref. [153], © WILEY-VCH Verlag GmbH & Co. KGaA, Weinheim 2019.

on MoS_2 powder to embed it on the surface of LLZO and heated it with Li at 100 ℃ for 2 h to improve the interface contact. The ASR of the Li negative electrode was reduced to 14 $\Omega \cdot cm^2$, and the assembled lithium was symmetrical. This battery can be operated at 100 ℃ at a current density of 2.2 $mA \cdot cm^{-2}$ [179]. LiF can also be used to increase stability of LLZTO and to suppress the formation of Li_2CO_3. The LLZT–2LiF shows a lower interfacial resistance of 385 $\Omega \cdot cm^2$, also with high coulombic efficiency 93% of its capacity after 100 cycles [161].

Another strategy to promote better interface contact is to introduce carbon as active electrodes and cycling them against the Li metal [180,181]. Mixing LLZO with carbon improves the electronic contacts and facilitates the intercalation of the mobile cations into and out the solid electrolyte on its reduction–oxidation process [182]. Mathematical analyses were used to understand the increase in wettability between Li–C composite and garnet electrolyte (Fig. 14(c)). The study showed that the Li–C composite and garnet present good interface stability upon electrochemical cycling [153]. The calculations favor a reaction between Li–C composite and garnet rather than Li–garnet. However, attention needs to be given to the surface contamination layer of Li_2CO_3, as this may affect the wettability of Li on LLZO [150,178]. Using composite materials is an alternative strategy to improve the interfacial contact [36]. A composite anode electrode was fabricated using Li–C and showed an improvement in the contact boundary between Li and solid electrolyte [153]. The composite is continuously stirred and melted on a hot plate at 250 ℃, and Li was prepared by adding graphite powder. The ASR with pure Li electrodes calculated is 381 $\Omega \cdot cm^2$ and the ASR obtained between Li–C/LLZO/Li–C was decreased to 11 $\Omega \cdot cm^2$, one of the lowest values reported thus far [153]. A recent design of a composite polymer electrolyte (CPE) consisted of SHP and LLZGO NPs, called "hybrid electrolyte" [183]. This compound presents strong adhesion and a seal-healing functionality design for stabilizing the Li anode [183]. In this model, the CPE membrane was soaked with liquid electrolyte ($LiPF_6$) to the lithium, and SEM characterization showed a good interfacial contact between them. The study only reports the resistance associated with the passivation layer impedance on the Li surface of 92.1 Ω after 500 cycles, and the hybrid electrolyte only 6.9 Ω after 500 cycles [183]. Apart from inhibiting the dendritic growth of Li and the improved the electrochemical performance, the use of a hybrid electrolyte can enhance the high energy density and extend the cycling life, with also a better safety performance for ASSLBs. Composite material coating of metal layers is another strategy to solve the interfacial contact [36,86]. Tsai and co-workers [69] deposited a layer of about 20 nm of Au on the surface of LLZO using an ion sputtering coater. This strategy reduced the ASR of the Li anode to 58 $\Omega \cdot cm^2$ [69]. Xiang and co-workers [184] deposited a Cu film of about 100 nm on the surface of LLZO by magnetron sputtering and allowed to react with the Li negative electrode at 250 ℃. This process resulted in an alloy at the interlayer with reduced ASR (from 677 to 29 $\Omega \cdot cm^2$). This lithium symmetrical battery can run more than 800 cycles at a current density of 0.2 mA/cm^2 [184]. To modify the Li|LLZO interface a Ge layer was coupled to the Li|LLZO|$LiFePO_4$ system [149]. This combination rendered a stable cycling performance at RT for the device, and delivered an ASR of 115 $\Omega \cdot cm^2$, in addition to good stability. Wetting at the lithiathed Ge/LLZO interface was confirmed by mathematical modeling and fitting of the experimental data [149]. A recent report used a limited amount of Li anode, coupled to the garnet-type $Li_{6.4}La_3Zr_{1.4}Ta_6O_{12}$ (LLZTO) pellet [185]. In this case, the LLTO–cathode interface layer of solid-state plastic crystal electrolyte (PCE) and an anode–LLZTO interface layer of a gold thin film were prepared. The EIS measurements revealed that the ASR of Li|LLZTO ranged from 115 to 75 $\Omega \cdot cm^2$ after loading 20 MPa pressure, suggesting that the pressure can optimize the Li|LLZTO interface contact. However, for the Li|LLZTO|Li symmetry cell with Au thin film on LLZTO surface, the ASR of Li metal–LLZTO was 25 $\Omega \cdot cm^2$, thus presenting an increased stability [185]. This study suggested a mechanism for Li loss, where the LLZTO SE first reacts with Li to form a stable SEI, and then a quite high Li loss is associated to the irreversibly trapped lithium in the copper current collector, as well as the contact loss of deposited lithium during the stripping process. It is well known that LLZTO reacts with Li to form Li_2CO_3 and Li_2O compounds on the SEI layer [182]. Au reacts with LLZTO and promotes enhanced molten Li diffusion into the garnet surface, improving the interface stability [183]. The study shows Li–Au alloy can be used as a Li-ion conductor between Li metal and garnet, which allows more uniform Li^+ flux and

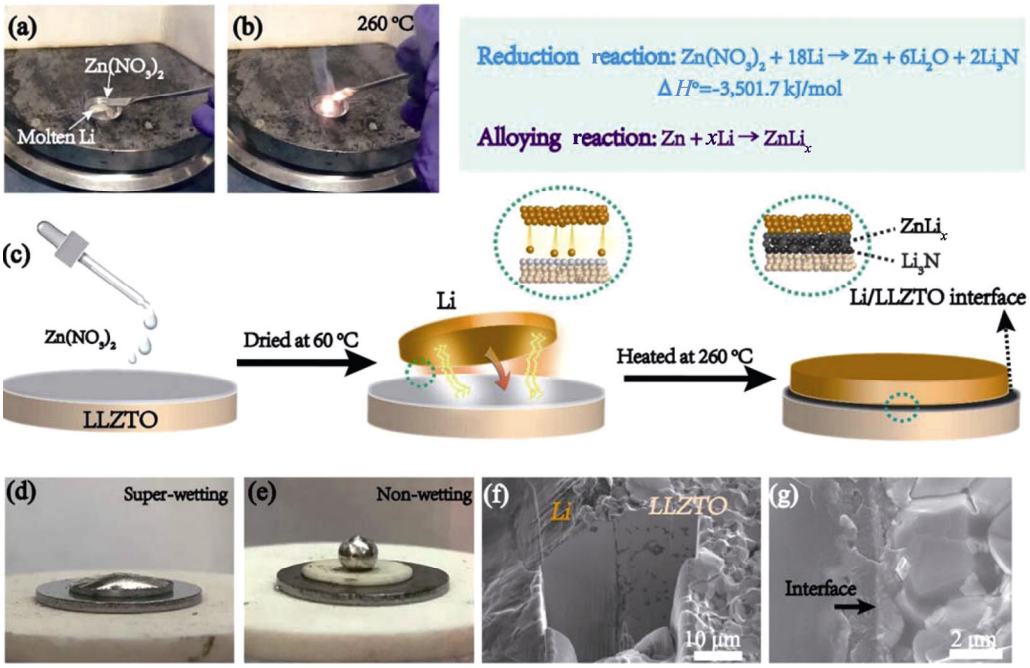

Fig. 15 Modification of Li-anode interphase. Photographs of Li reacting with $Zn(NO_3)_2$: (a) before and (b) amid the reaction. (c) Schematic illustration of the preparation procedure of the solid-state ZNR Li/LLZTO interface. Li wetting on (d) $Zn(NO_3)_2$-coated and (e) pristine LLZTO pellets. (f, g) Cross-section SEM images of the ZNR interface. Reproduced with permission from Ref. [38], © Wiley-VCH Verlag GmbH & Co. KGaA, Weinheim 2020.

improves Li^+ transport. However, the formation of Li dendrites at high current densities (0.30 $mA \cdot cm^{-2}$) is inevitable [185]. ALD of Al_2O_3 has become one effective method to reduce the ASR from 1710 to 1 $\Omega \cdot cm^2$ [144]. While the molten metal Li is on the surface of LLZO treated by ALD, the existence of the AL_2O_3 layer increases the interface contact area and inhibits the formation of Li_2CO_3 [144].

A chemical reaction between $Zn(NO_3)_2$ and Li produced a new solid-state interface that bonds together the $Li_{6.4}La_3Zr_{1.4}Ta_{0.6}O_{12}$ (LLZTO) electrolyte and the Li metal ion (denoted as the ZNR interface) [38]. This interface allows efficient conductive pathways for Li^+ transport through the interface without dendrite formation or side reactions with the electrolyte observed after 1000 h of continuous charging and discharging. The ASSLB Li||$LiFePO_4$ (Li||LFP) also showed a stable capacity of 150 $mAh \cdot g^{-1}$ at 1 C rate for nearly 400 cycles, which represents the highest performance reported to date [38]. Han and coworkers [171] deposited a layer of 6 nm Al_2O_3 on the surface of $Li_7La_{2.75}Ca_{0.25}Zr_{1.75}Nb_{0.25}O_{12}$ by ALD and heated it with the lithium anode at 250 ℃ for 1 h to form an alloy intermediate layer. The ASR of the lithium negative electrode was reduced from 1720 to 1 $\Omega \cdot cm^2$ at RT. Experimental and computational analyses revealed that the oxide coating enables wetting of metallic lithium in contact with the garnet electrolyte surface, and that the lithiated-alumina interface allows effective lithium-ion transport between the Li metal anode and garnet electrolyte [171]. Although the high contact area ALD is a very effective method to improve the interface anode contact, simple polishing becomes more attractive for practical applications.

(1) Li dendrite on LLZO

Lithium dendrites can still be found in LLZO SEs; these tend to form along grain boundaries and SEs with voids [37,186]. There are two major mechanisms for the formation of Li-dendrites. The first one initiates with the nucleation of Li dendrite at the Li anode/LLZO electrolyte interface, which then passes through the interstitial space of LLZO electrolyte particles [187]. The second mechanism proposes the formation of dendrites within the solid electrolyte [188]. At high currents, the formation of dendrites causes the Li/LLZO/Li cell to short circuit. The critical current density, at which the cell will be shorted, is less than 0.9 $mA \cdot cm^{-2}$ at RT [69,189,190], while the critical current density of liquid electrolytes can reach 4–10 $mA \cdot cm^{-2}$ at RT [191]. Evidence suggested that doped LLZO becomes partially lithiated when interacting with Li [170]. This lithiation causes a phase transition

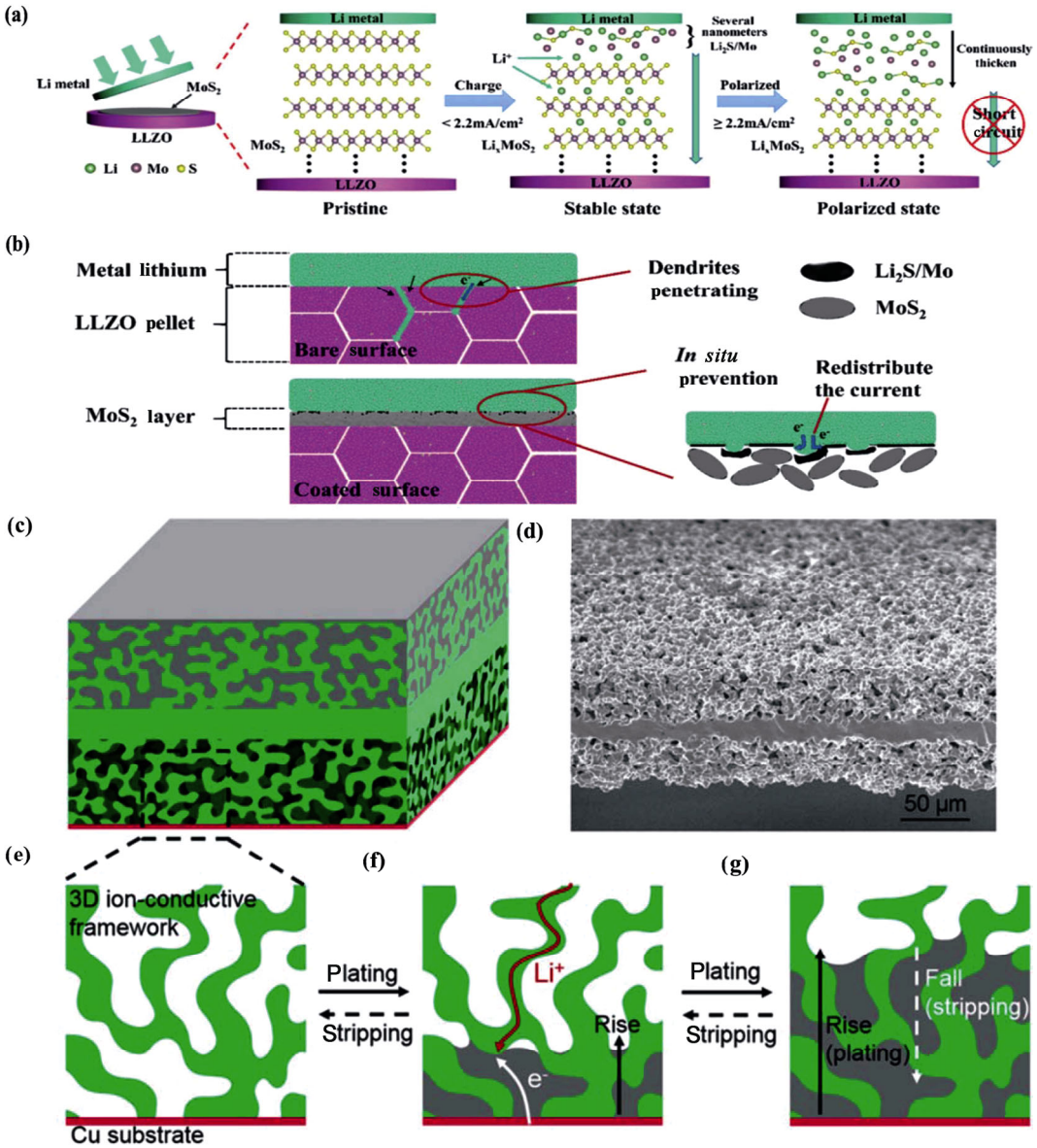

Fig. 16 Strategies to suppress Li dendrites. (a) Schematic representation of the morphological and chemical evolution of the MoS_2-coating layer in the polarization process. (b) Illustration of the *in situ* MoS_2 protection mechanism. The scheme shows the process of Li plating and stripping in the 3D Li-ion-conductive host. Reproduced with permission from Ref. [179], © The Royal Society of Chemistry 2019. (c) Diagram of the 3D ion-conductive host for studying Li-ion plating/stripping, where the upper layer is filled with the Li source and the lower layer is empty with Cu deposited on the bottom. (d) Side-view SEM image of the pristine 3D ion-conductive host. 2D local schematic for (e) lower layer of the pristine empty host without Li, (f) Li deposited in the 3D ion-conductive host from the bottom current collector, and (g) more Li deposited and grown in the 3D host. Reproduced with permission from Ref. [195], © Published under the PNAS license 2018.

from the cubic to the tetragonal phase [177,186]. The macroscopic ionic conductivity of the tetragonal phase is lower but barely limits conduction as a nanometric film, constituting ideal interphase [187]. Han and co-workers [188] proposed that short-circuit formation in garnet SSEs is caused by internal Li deposition led by high electronic conductivity. Since the electronic conductivities of garnet SSEs increase with temperature, the evidence showed that Li dendrites are easier to form at high temperatures. When the temperature increases (from 20 to 100 ℃), the ionic conductivity of garnet SSE increases by one order of magnitude, and the electronic conductivity increases by two orders of magnitude, from 6×10^{-8} to 1×10^{-7} S·cm^{-1} [188]. At higher temperatures, the electronic leakage current to ionic current ratio should be lower, resulting in less

internal Li deposition. However, according to other sources, the lithium dendrites form in LLZO, regardless of the dopants used to stabilize the cubic structure [191]. Also, the low relative density of SEs was thought to be the primary cause of Li dendrite growth, but there is no connection between dendrite suppression and the relative density LLZO [69]. Indeed, Li dendrites keep growing in a dense LLZO (relative density > 97%) [189,192], and further the formation of dendrites has been related to low lithium-ion diffusivity at grain boundaries [193,194].

As discussed above, increasing the ionic conductivity of grain boundaries does not increase dendrite suppression capability [196,197]. Dendrite growth was also thought to be primary reason of pre-existing defects in surface and bulk SEs, such as cracks, since dendrite growth is favored in defective or cracked areas. The stress that induces dendrites can further extend the crack, promoting Li dendrite propagation [198,199]. However, this theory lacks of evidence of the mechanisms by which the dendrites form at a similar current density in LLZO with different surface roughness and why the dendrites still form in single-crystalline LLZO [198]. Dendrite formation has also been attributed to inhomogeneous Li plating caused by inadequate interfacial interaction between Li and SEs [189]. This can be explained by the fact that the critical current density increases in an inverse manner with the decrease in interfacial resistance between Li and SEs [178]. Even if the ASR of the Li/electrolyte interface has been optimized to be comparable to or even lower than in the liquid electrolyte, dendrites still grow at a low current density (0.9–1 $mA \cdot cm^{-2}$) [200]. To date, there is a gap on our understanding on this process, and thus, there is no clear road to prevent lithium dendrite formation in LLZO at the current density used (10 $mA \cdot cm^{-2}$) required for the fast-charge goal, which may prevent their effective integration with Li anodes [201]. However, high mechanical strength can inhibit dendritic Li growth [159]. According to computational analyses, garnet SSEs should have enough mechanical strength to prevent Li dendrite growth [197,202]. At high current densities, however, Li dendrites can develop into single crystal garnet SSEs, according to a recent experimental report [193,199]. Despite that, experimental evidence suggests that Li dendrites can grow into single crystal garnet SSEs at high current densities [198]. Good contact between electrodes and SSEs can also enhance the cycling stability, due to an improved interface and uniformly distributed Li-ion transport. An alloy interface layer, on the other hand, can provide a secure interface during cycling as well [198–200].

Some strategies have been developed to improve the SEIs, and to inhibit the formation of lithium dendrites between the Li metal anode and garnet-type SE. For example, designing 3D ion-conductive frameworks (Fig. 16(c)) have been proposed to effectively suppress the growth of Li dendrites and avoid the occurrence of cell short-circuit [195]. In this model, 3D solid electrolytes that have plenty pores and voids allow Li to expand smoothly through the structure host without causing Li dendrites formation [195]. Furthermore, using electrolyte additives, external pressure, highly concentrated electrolyte, composite materials, surface coating, polishing layers, and unlimited Li sources, are other alternatives strategies to overcome these issues [199–201]. Hence, research needs to be directed to characterize novel compounds' structures at the atomic level and to utilize *in situ* modeling techniques to understand the mechanism of Li anode-solid electrolytes and improve the stability among them.

(2) Electrochemical stability of LLZO

With both the Li anode and the cathode materials, the LLZO SEs are among the most stable SEs [6,9,21,22,29]. The wide electrochemical window of garnet SEs (> 6 V vs. Li/Li^+ from CV studies and 3 V from computational analyses) allows for high voltage batteries [203]. Stable battery efficiency also involves electrochemical stability [4,5,79,204]. The current density, mechanical properties, interfaces, and ionic and electrical conductivities all play a role in electrochemical stability [193]. In addition to theoretical calculations for understanding lithium-ion conductivity in garnet electrolytes, the intrinsic electrochemical stability of $Li_7La_3Zr_2O_{12}$ can be calculated *in situ* by first-principals analyses (Fig. 17) [204]. A semi-blocking electrode is applied to test the electrochemical stability window by using a conventional method [17,204]. In this case, the c-LLZO electrolyte presented a wide electrochemical window that ranged between 0 and 6 V [205]. Despite this, the value derived from first-principals analyses was significantly lower than the experimental results. For instance, at 2.91 V, the LLZO electrolyte was found to oxidize to La_2O_3, $Li_6Zr_2O_7$, and Li_2O_2. The output of O_2 increased as the voltage was increased, as did the oxidation of

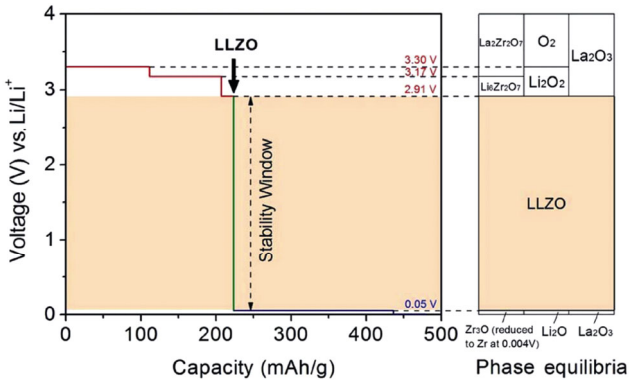

Fig. 17 Voltage profile of LLZO solid electrolyte upon determined from the first-principles calculation. Reproduced with permission from Ref. [204], © WILEY-VCH Verlag GmbH & Co. KGaA, Weinheim 2016.

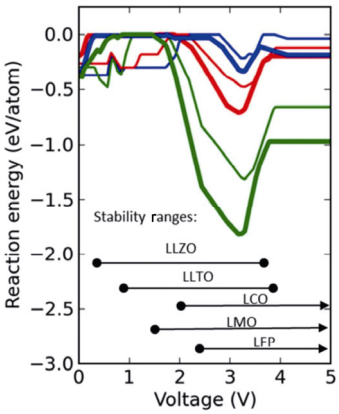

Fig. 18 Stability window for cathode materials with LLZO. Driving force for interphase formation between electrolyte and cathode, with varying voltage from 0 to 5 V vs. Li metal. The calculated LLZO, LLTO, and LCO, LMO, LFP intrinsic stability windows are marked on the bottom for reference. Colors represent: blue—$LiCoO_2$, red—$LiMnO_2$, green—$LiFePO_4$, thick—LLZO, thin—LLTO. Reproduced with permission from Ref. [141], © American Chemical Society 2015.

Li_2O_2. At the same time, the LLZO electrolyte was reduced to Zr_3O, La_2O_3, and Li_2O when the potential was reduced to a low value (below 0.05 V) [134]. Additionally, Zr is produced by reducing Zr_3O at a much lower potential. The LLZO electrolyte was not thermally stable, according the first-principals analyses. Nonetheless, deposition of lithium ions interfered with LLZO reduction at low potential, making the reduction of LLZO difficult [204]. The reduction of Zr_3O to Zr occurred thermodynamically, without taking into account the effect of DFT measurement bias [204,205]. With the same calculation method, the electrochemical stability of LLZO doped with Al, Ta, and Nb was also investigated [112,139,176,196]. The analyses showed that elemental doping had no effect on electrochemical stability, and the small amount of element doping had a negligible effect [17,134]. The electrochemical stability of SSEs and Li metal anodes has been reported to be improved by a Li–Al or Li–Mg alloy interface [70]. Because of the lack of driving force, Li can deposit on the alloy layer and drive it away from the interface rather than moving through the metallically conductive alloy interface layer [159]. Better understanding of the electrochemical stability of the LLZO solid electrolytes with electrode materials is of great importance, which can provide guidance to avoid forming unwanted compounds and decrease the interfacial resistance and help to optimize the solid-state interphase at the battery performance.

6.1.2 Interfacial issues between LLZO/cathode

There are a large variety of materials used for the cathode electrodes. Figure 18 shows the reaction energy of LLMO (M = Zr, Ta), the most used cathode materials, to study the thermodynamic stability of the cathode–LLZO interface [141], being the most common $LiFePO_4$ (LFP) and $LiCoO_2$ (LCO). $LiFePO_4$ has a long-term life cycle and high-power capacity in traditional lithium-ion batteries [206]. On the other hand, theoretical calculations indicate that LCO|LLZO has the most stable interphase due to a small driving force for LLZO decomposition in the charging state. $LiMnO_2$ (LMO) and LFP react very strongly with LLZO-based electrolytes [141,207]. X-ray diffraction (XRD), Raman spectroscopy, and X-ray photoelectron spectroscopy (XPS), have been used to study the chemical compatibilities with LLZO [208]. These studies showed LMO and LFP can react with LLZTO at temperatures as low as 500 ℃ and the reaction products between LLZTO and NCM are complex. LCO have received a lot of attention, due to its high electrochemical and chemical stability against a Li-garnet electrolyte, as well as its compatibility with LLZO SE [207,209]. Understanding the mechanism and stability of LLZO SE against mixing and sintering with major commercial oxide cathodes may help to avoid unwanted compounds, lower the interfacial resistance, and improve the composition of coating layers [141,207–209]. First-principals studies based on thermodynamic DFT estimated the oxidation potential of LLZO to be 2.9 V, with an equilibrium potential of 3.3 V, which corresponds to totally de-lithiated LLZO

[204]. This oxidation potential refers to the oxygen evolution reaction, which is considered to be kinetically difficult, and is predicted to have a high overpotential, which may be the cause of LLZO garnet's strong oxidation stability [204].

After all, the high ARS between LLZO and cathode materials represents a challenge that needs to be solved [212]. Undesired reactions occurred during battery usage that impaired their performance [211,212]. For instance, the formation of a tetragonal LLZO phase at the LCO|LLZO interface, due to the cross-diffusions of elements at high temperature, decreased the initial CE and life cycle [209]. The secondary phase on LLZO forms in a humid atmosphere, leading to form high ASR and adversely affecting the capacity at RT. Therefore, the reaction of LLZO with the cathode, CO_2/H_2O, and diffusion layers with cathode–LLZO interface, reduce the electrochemical performance of ASSLBs [214]. In addition, high interfacial resistance is due to the formation of the Li_2CO_3 layer and weak physical contact [82].

To mitigate interface concerns, several approaches have been developed, where employing coating layers on the interface contributes to lowering the resistance and enhancing the lithium mobility at the interface [208–215]. Pulsed laser deposition technology (PLD) has been used to coating the cathode–electrolyte interface to address interface concerns [166,167,184]. A study used PLD to deposited $LiCoO_2$ and assembled the $LiCoO_2$|$Li_{6.75}La_3Zr_{1.75}Nb_{0.25}O_{12}$ ASSLB, and determined the electrochemical performance and ASR [166]. Under these conditions, the ASR between LCO and LLZO–Nb was 170 $\Omega\cdot cm^2$ at RT [166]. The battery showed a good charge–discharge behavior and a stable cycle efficiency, as well as a theoretical electrochemical capacity for $LiCoO_2$ of 137 $mAh\cdot g^{-1}$, for 0.5 Li per CoO_2 [166].

Studies have also focused on the usage of mixtures of different cathode materials to enhance the interfacial stability with LLZO and electrochemical and chemical properties of combinations like LCO/LLZO and LCO–$LiBO_3$/LLZO cathode interfaces [210,214]. For the LCO/LLZO cathode interface, an irreversible electrochemical reaction at 3.0–3.8 V vs. Li^+/Li was determined; this was detrimental to reversible capacity retention of the ASSLB [210]. Apart from that, during the high temperature cathode formation, time-of-flight secondary ion mass spectroscopy (TOF-SIMS) and XRD confirmed c-LLZO reacts with LCO and forms the t-LLZO phase at the interface [209]. For the LCO–$LiBO_3$/LLZO cathode interface, it was determined that the $LiBO_3$ blocks undesirable chemical reactions at high temperature and the charge capacity was 79.9 $mAh\cdot g^{-1}$, and discharge capacity was 67.2 $mAh\cdot g^{-1}$ with a CE of 84.1% [209], making this combination the most efficient and with higher capacity of all the samples tested [209]. Wet coating and hot-pressing methods were used to develop a simple low-cost method to construct ASSLB (Fig. 19(a)) [162]. The LFP cathode layer was uniformly coated on the Al foil; Figs. 19(b) and 19(c) indicate the not so obvious interface between the cathode layer and the electrolyte [162]. The interfacial resistance of the LFP/LLZO was reduced from 248 to 62 $\Omega\cdot cm^2$ [162].

Screen-printing is another method for enhancing the cathode interface [210]. An ASSLB was assembled with Li_3BO_3 (LBO) lithium-ion conductor as a buffer layer between LCO active cathode material and Nb-doped $Li_7La_3Zr_2O_{12}$ (LLZO–Nb) solid electrolyte [210]. Sufficient contact between the cathode layer and LLZO–Nb solid electrolyte was easily achieved by sintering LBO into the cathode layer by the annealing process (700 ℃) [210]. XRD and SEM results showed a good chemical stability and interfacial contact between the cathode and solid electrolyte materials and the ASR of the battery was 80 $\Omega\cdot cm^2$ at RT [210]. By using V_2O_5 as cathode material, a high temperature ASSLB was assembled with $Li_7La_{2.75}CaZr_{1.75}Nb_{0.25}O_{12}$ (LLCZNO) particles in a reaction carried out at 100 ℃ [211]. The resulting compound had reliable safety parameters and stable cycling performance [211]. A thermal annealing technique to treat the cathode and garnet interface was also employed to ensure no parasitical reactions associated. In this case, the ASR was significantly decreased, from 2.5×10^4 to 71 $\Omega\cdot cm^2$ at RT, and the battery presented an interfacial resistance of 45 $\Omega\cdot cm^2$ with a CE of 97% and a stable discharge capacity at 100 ℃ [211].

The compatibility of $Li_{6.75}La_3Zr_{1.75}Ta_{0.25}O_{12}$ (Ta–LLZO) with LCO and $Li(NiCoMn)_{1/3}O_2$ (NCM) commercial cathode materials was investigated [212]. First-principles DFT analyses indicated that the NCM/Ta–LLZO interface is more stable, with poor cycling stability which may be due to the formation of $LaNiO_3$ [212]. Figure 20 summarizes of the process for ball-milling and sintering treatments. In this case, Mn is the most stable element in NCM, while Ni is an active element and exchange with both Li and La at the interface

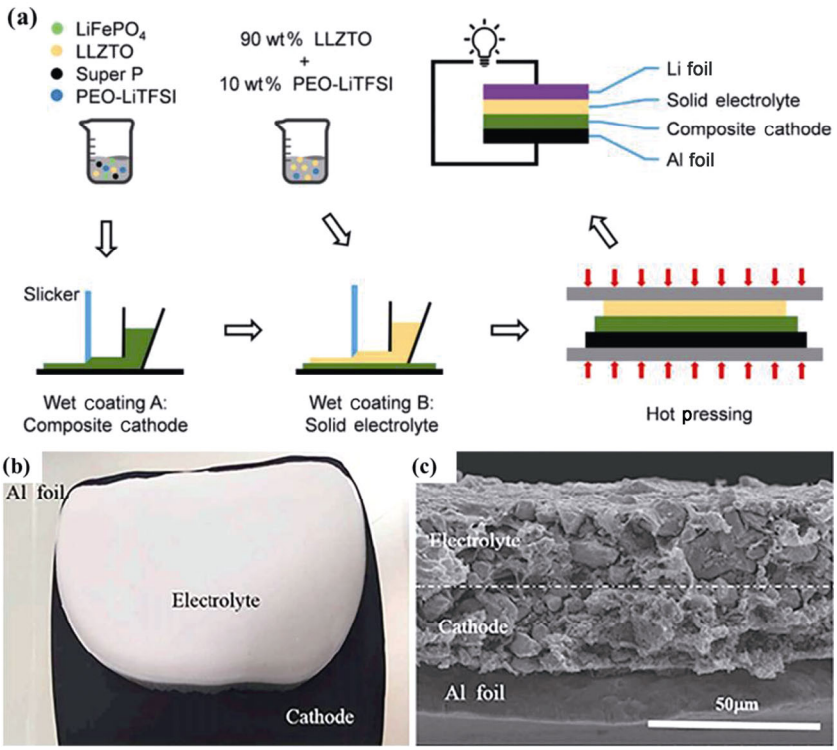

Fig. 19 Li-cathode interphase modification. (a) Schematic illustration of the synthesis procedure. (b) Photograph and (c) cross-sectional FESEM image of the $LiFePO_4$ cathode layer and $90LLZTO–10PEO_{18}$ electrolyte layer. Reproduced with permission from Ref. [162], © Elsevier B.V. 2018.

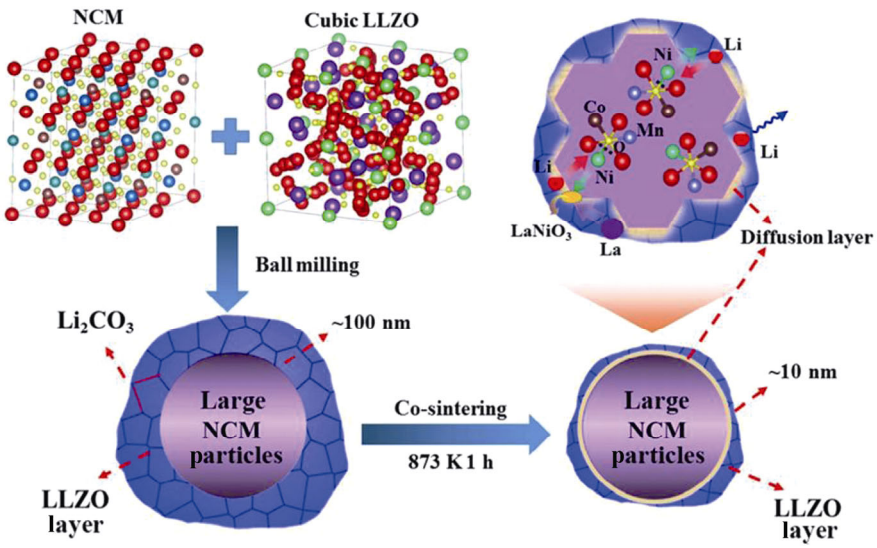

Fig. 20 LLZO and NCM cathode material. A brief schematic representation for the formation process and the structure of the LLZO surface layer on large NCM particles during the ball milling and co-sintering processes. Reproduced with permission from Ref. [212], © American Chemical Society 2018.

[212]. Increasing Ni–Li/Ni–La may improve the interfacial stability between cathode and LLZO SE at high temperatures [212]. A novel mixture of cathode material composed by $LiNi_{0.7}Co_{0.15}Mn_{0.15}O_2$ and LFP was developed [213]. This cathode material exhibited oxidation and reduction peaks at 3.58 V (cathodic peak) and 3.38 V (anodic peak), which correspond to the two-phase transition of the Fe^{2+}/Fe^{3+} redox couple [213]. This work proved that mixing cathode materials could improve the electrochemical properties, higher interface contact between cathode/LLZO, and better battery performance [213].

Coating materials are one promising solution to improve the cathode/LLZO interface, under different processing conditions [208–211]. $LiNbO_3$ and $LiTaO_3$ are recommended ternary metal oxides for mixing with LLZO, due to the improved the oxidation stability of LLZO, as these oxides do not have high oxidation limit [214]. $LiTaO_3$/NCM and $LiNbO_3$/LCO interfaces have no driving force to interact with the oxide cathodes in both fully lithiated and half lithiated stages [214]. Thus, to improve the interface contact between LLZO and the positive electrode, a composite positive electrode material with a solid PEO electrolyte and assembled $LiCoO_2$–PEO|Ta–LLZO|Li battery was developed [155]. In this case, the ASR was large (6200 $\Omega \cdot cm^2$), but the battery can only run 10 cycles at 60 ℃ and 0.2 C [155].

An alternative ceramic processing strategy to assemble an oxide-based cathode composite based on LFP and LCO was developed (red square in Fig. 21). Here, the LCO–LLZO and LFP–LLZO were prepared through direct synthesis form metal salts to the oxide cathode in a porous LLZO scaffold. This allowed a good mechanical contact, with no adverse reactions at the interphase, and at low temperature 700 ℃ for synthesis [215]. The LCO–LLZO composite cathode showed a promising discharge capacity of 118 $mAh \cdot g^{-1}$ (3–4.05 V), with low interfacial resistance of 62 $\Omega \cdot cm^2$ [215]. This preparation method provides a solution to address the adverse interphase reactions based on chemistry and ceramic thermal processing records, as well as increasing the number of reaction sites for enhanced the performance of composite cathodes for LLZO ASSLBs.

6. 2 LLZO/polymer composite solid electrolyte and its all-solid-state lithium batteries

Composite solid electrolytes (CSEs) are mixtures of inorganic fillers and polymer electrolytes [36,148]. Latest research demonstrates that CSEs can effectively minimize the crystallinity of polymer, thereby increasing the ionic conductivity of the final CSEs [158]. These have exceptional properties that could enhance interface problems between electrode–electrolyte, ion transport process across the interfaces, simple architecture on ASSLBs solving the wetting problems, and improve CE [71,216,217]. The most studied solid polymer electrolyte is PEO because of its low cost, ability to dissolve a wide variety of lithium salts, and relatively high chemical/electrochemical stability [36,71]. However, the PEO has a low ionic conductivity (10^{-8}–10^{-6} $S \cdot cm^{-2}$) at RT [218] and its mechanical properties at high temperatures result in lithium dendrites and safety hazards [219,220]. PEO/LLZO composite electrolytes melt when heated to high temperatures (near to PEO

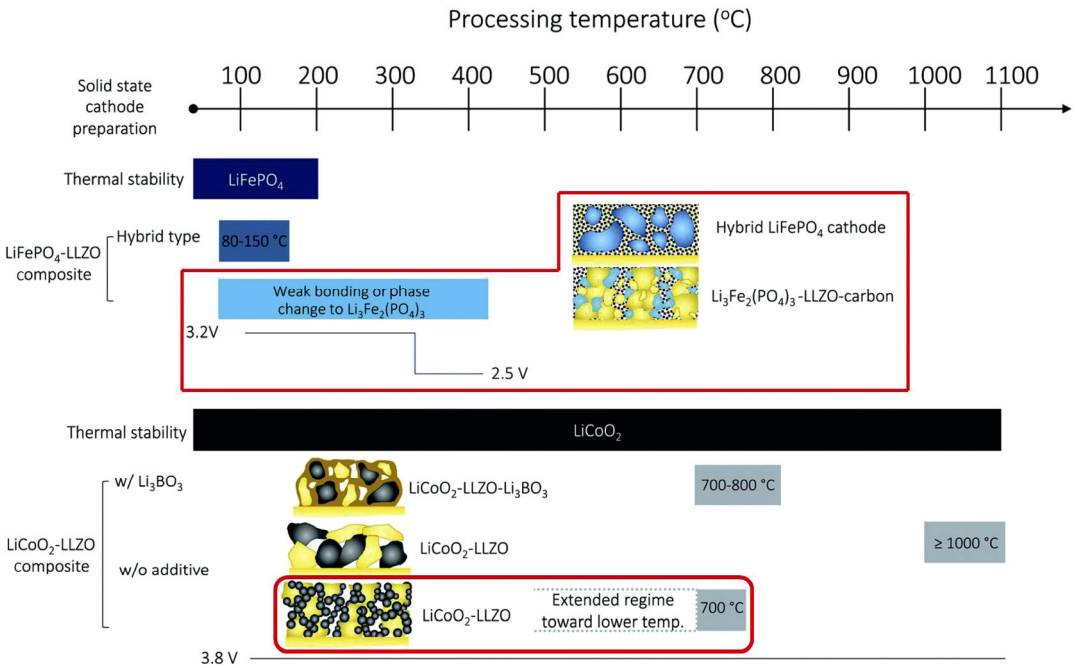

Fig. 21 Overview of all-oxide Li-garnet SSBs based on $LiFePO_4$- and $LiCoO_2$-based cathode composite design and ceramic processing options: processing temperature vs. chemical and mechanical stability. Reproduced with permission from Ref. [215], © The Royal Society of Chemistry 2020.

melting point), enhancing the ion transport [168,228]. Ion transport in the PEO matrix can be a slow process at low temperatures; here the formation and breaking of lithium–oxygen (Li–O) bonds, which involves the ether oxygen atoms on a segmental PEO chain coordinated with Li ions, leads to a rapid conductivity decrease [218]. Though PEO solidifies at low temperatures, the chain's segmental motion becomes slow; at the same time, the solid PEO blocks Li ions from moving between LLZO particles [158,162]. However, the integration of LLZO particles or fillers into polymer improves the ionic conductivity and also the mechanical strength and stability of the SE [36,155]. Combining experimental with computational analyses, researchers have investigated the Li transport properties of PEO. For the case of Ga–LLZO CSE, the improved ionic conductivity can be ascribed to the ionic conduction in the space charge regions and the percolation of the space charge regions. While the Ga–LLZO content exceeds the percolation threshold value, a continuous pathway is formed in charged regions that behaves as the fast channel for Li^+ ion transportation, as illustrated in Fig. 22. The PEO:Ga–LLZO composite shows great potential in ASSLBs with an electrochemical window 4.6 V [228]. This combination

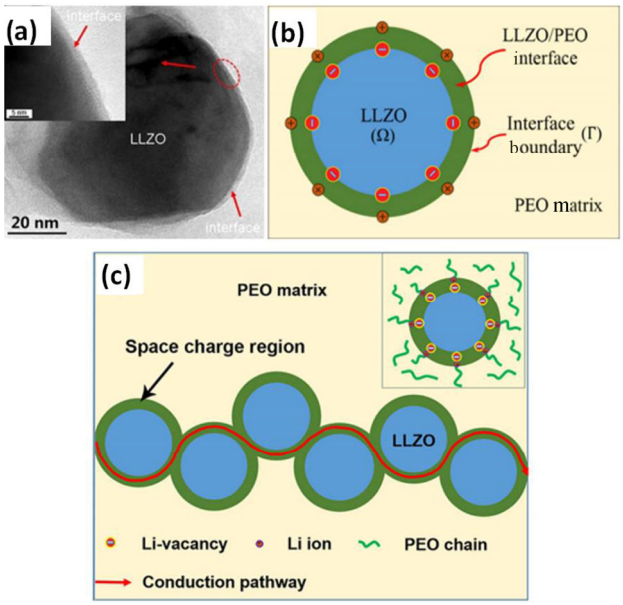

Fig. 22 Space charge region at the Ga–LLZO/PEO interface. (a) TEM images of the Ga–LLZO/PEO interface. (b) Schematic illustration of Ga–LLZO nanoparticle in the PEO:Ga–LLZO composite. (c) Schematic representation of the fast ionic conduction pathway along the space charge regions. Reproduced with permission from Ref. [228], © American Chemical Society 2018.

is stable with Li-anode, with a discharge capacity of 145 $mAh \cdot g^{-1}$ at 0.1 C [228]. To further develop LLZO CSEs with enhanced properties, other types of polymers, such as poly(propylene carbonate) (PPC) [163,219, 221,222], poly(ethylene carbonate) (PEC) [223], polyacrylonitrile (PAN) [70], poly(methyl methacrylate) (PMMA) [224], cross-linked polyethylene glycol [225], poly(ethylene glycol) diacrylate (PEGDA) [226], and mixed polymers [218,227] have been used as substrates for constructing novel and more efficient LLZO-based/polymer CSEs.

Our group fabricated a CSE of LLZO/PEO, by mixing different amounts of LLZO ceramic powders into the PEO matrix [158]. We found that the addition of LLZO can effectively inhibit PEO's crystallization [228]. A correlation between an increase in the crystallinity content and the increase in LLZO content was determined [229], consistent with the fact that excessive LLZO particles are difficult to disperse in PEO matrix and easily form clusters [228,229]. Follow up studies on CSE composed by LLZTO, PEO–LiTFSI, and SN demonstrated that the CSE 60%LLZTO–10%SN exhibits a maximum conductivity of 1.22×10^{-4} $S \cdot cm^{-1}$ [158]. The electrochemical stability of this compound ranged from 4.7 to 5.5 V vs. Li/Li^+ and a transfer number of 0.410 [158]. The LFP|LLZO/PEO–SN|Li cell shown in Fig. 23 exhibited the maximum discharge capacity of 151.1 $mAh \cdot g^{-1}$ after 200 cycles under 60 ℃ [158].

Another CSE (PEO–0.5LLZNO) was prepared by incorporating 33.3 wt% of LLZNO (LLZNO = $Li_{6.4}La_3Zr_{1.4}Nb_{0.6}O_{12}$) powder into the PEO matrix [230]. This CSE exhibited a high ionic conductivity of 1.4×10^{-3} $S \cdot cm^{-1}$ and a wide electrochemical window range of 0–5.2 V at 60 ℃ [230]. Also, an LFP|PEO–0.5LLZNO|Li cell was able to deliver a high specific discharge capacity of 153 $mAh \cdot g^{-1}$ and excellent capacity retention of 97% after 150 cycles at 0.5 C under 60 ℃ [230]. Another example is the PEO–LiBOB–LLZO composite electrolyte prepared by Guo and collaborators [231], which presented an ionic conductivity of 2.4×10^{-4} $S \cdot cm^{-1}$ at 20 ℃. The assembled LFP|LLZO–LiBOB|Li battery was cycled at 0.1 C for 100 cycles at RT [231] and rendered a rate for capacity retention of 84.6% [231]. Karthik and Murugan [232] prepared a CSE (GCPEM-20) by solution-casting method, and consisted of a PEO with a large molecular weight ($\sim5\times10^6$), LCO, and $Li_{6.28}Al_{0.24}La_3Zr_2O_{12}$ (Al–LLZO) in a mass ratio of 8:1:2. The fabricated CSE

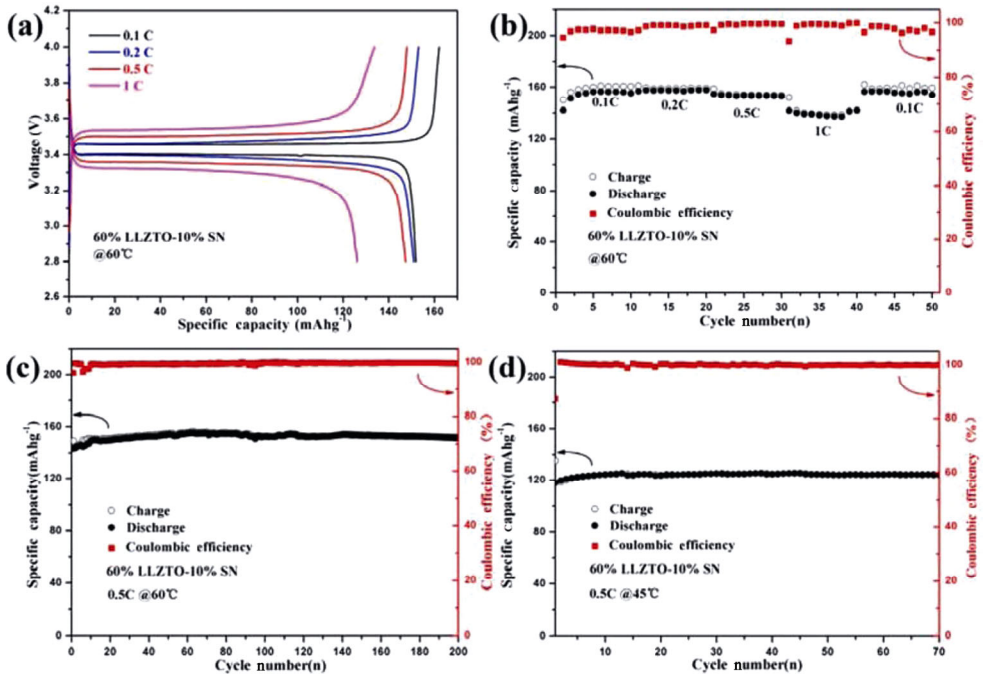

Fig. 23 Electrochemical performance of the Li/60%LLZTO–10%SN/$LiFePO_4$ batteries: (a) initial charge and discharge curves at different rates (0.1, 0.2, 0.5, and 1 C), (b) rate performance from 0.1 to 1 C, (c) cycling performance at 0.5 C and 60 ℃, and (d) cycling performance at 0.5 C and 45 ℃. Reproduced with permission from Ref. [158], © Elsevier B.V. 2018.

exhibited a high Li^+ conductivity of 4.4×10^{-4} S·cm^{-1} and a stable electrochemical window of 4.5 V at 30 ℃ [232]. Accordingly, the specific discharge capacity of $LiCoO_2$ in the LCO|PEO_8–$LiClO_4$ + 20 wt% Al–LLZO|Li cell is up to 142 mAh·g^{-1} at 0.06 C and 25 ℃ [232]. All these results showed CSE fabricated with LLZO and PEO can deliver good ionic conductivity, suitable Li^+ transfer number, and compatible electrode/electrolyte interfacial resistance. Even though ASSLBs show acceptable performance at higher temperatures, polymer solid electrolyte achieves a low ionic conductivity at RT, inhibiting good performance for the battery at ambient conditions. A three-dimensional LLZO framework was developed by filling polytetrafluoroethylene (PTFE) as a plasticizer and Ta doped LLZO; this hybrid LLZTO solid electrolyte composite showed a 1.2×10^{-4} S·cm^{-1} of ionic conductivity at 25 ℃ [233]. The assembled LFP|LLZTO–SN|Li handled a discharge capacity of 153 mAh·g^{-1}, at 0.2 C in the first cycle, and the capacity retention rate is high 90.3% after 200 cycles [233].

Particle size, morphology, and amount of LLZO solid electrolytes are key elements in the system of the cell. These can optimize ionic conductivity and solve interfacial issues, enhancing the performance of the ASSLBs [82,86]. Regarding particle size, a study of the effect of $Li_{6.4}La_3Zr_{1.4}Ta_{0.6}O_{12}$ (LLZTO) where different particle sizes (~40 nm, ~400 nm, and ~10 μm) were incorporated into the PEO matrix to form the LLZTO/PEO CSEs in the absence of lithium salts showed that the ionic conductivity of the CSEs inversely correlated the particle size of LLZTO [234]. The highest ionic conductivity was 2.1×10^{-4} S·cm^{-1} at 30 ℃ and ~40 nm LLZTO. Due to the high ionic conductivity, two batteries were assembled LFP|LLZTO/PEO|Li and $LiFe_{0.15}Mn_{0.85}PO_4$|LLZTO/PEO|Li [234]. Both displayed superior electrochemical performance, with the specific capacities of 153.3 and 132.1 mAh·g^{-1} at 0.05 C, respectively, and capacity retention of 90% after 200 cycles at 0.1 C under 60 ℃ [234]. The authors proposed that a small particle size of LLZTO favors to achieve a relatively larger specific surface area, which improves the Li pathways and facilitates percolation, thus showing a wide electrochemical window up to 4.7 V [234]. However, instability problems occurred when operating for prolonged period of time at high voltage [234]. Therefore, a novel type of CSE composed of silane-modified $Li_{6.28}La_3Al_{0.24}Zr_2O_{12}$ (s@LLAZO) nanofibers and poly-ethylene glycol diacrylate (PEGDA) was developed [226]. This combination presented excellent cycling stability and wextraordinary high rate capability with LFO and $Li[Ni_{1/3}Mn_{1/3}Co_{1/3}]O_2$ cathodes (Fig. 24) [226]. Additionally, with Li-ion batteries, LLZO

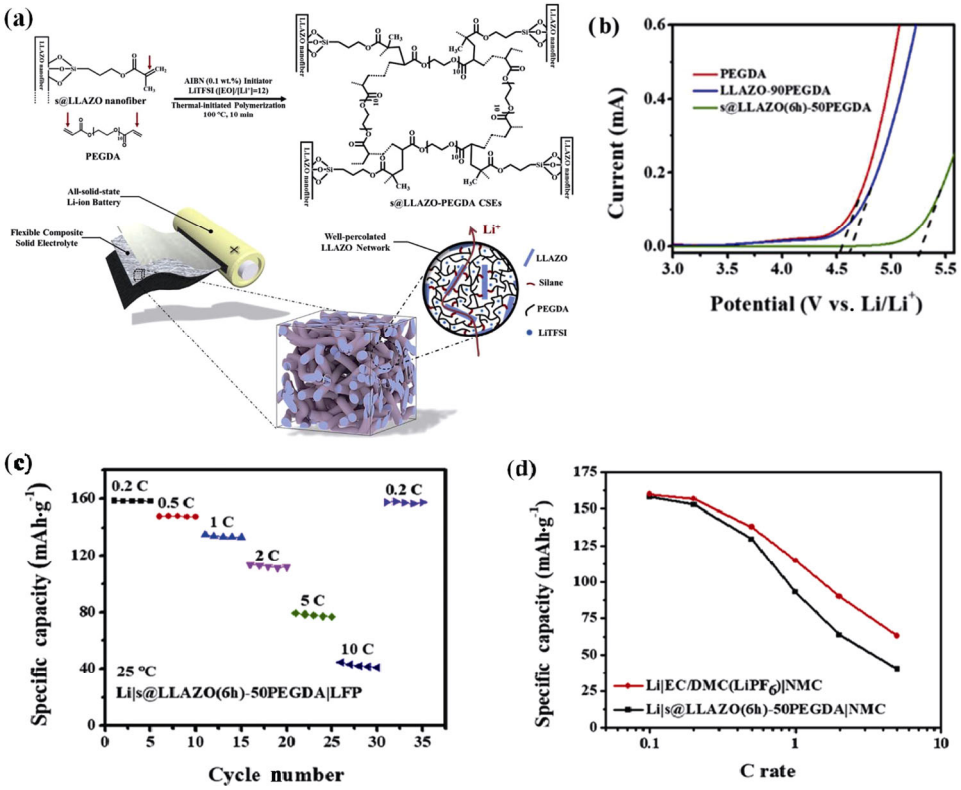

Fig. 24 LLZO–polymer composite electrolyte. (a) Schematic representation of the synthesis procedure of s@LLAZO–PEGDA CSE, providing the fast and nontortuos Li^+ conductive pathways. (b) Linear sweep voltammetry curves of PEGDA, LLAZO–90PEGDA, and s@LLAZO(6h)–50PEGDA CSEs. (c) Rate capability (0.2–10 C) of all-solid-state Li|s@LLAZO(6h)–50PEGDA|$LiFePO_4$ cell operated at 25 ℃; (d) rate capability (0.2–5 C) of all-solid-state Li|s@LLAZO(6h)–50PEGDA|NMC and liquid Li|EC/DMC($LiPF_6$)|NMC cells operated at 25 ℃. Reproduced with permission from Ref. [226], © Elsevier B.V. 2019.

solid electrolytes are remarkable applications in otherwise rechargeable lithium batteries, such as lithium–sulfur batteries (Li–S), oxygen battery (Li–O_2), and Li–V_2O_5 (Li–V) battery [40,86]. A solid-state Li–S battery was reported with LLZO–PEO electrolytes and sulfur composite cathodes based on LLZO@C, which operates successfully at 37 ℃ with a capacity of > 900 mAh·g^{-1} at 0.5 mA·cm^{-2} for 80 cycles [235]. Tao *et al.* [236] used a CSE containing PEO as the host and Al^{3+}/Nb^{5+} co-doped cubic $Li_7La_3Zr_2O_{12}$ (15 wt%) as the filler and a modified sulfur cathode to assemble a Li–S battery successfully. Inside the assemble Li–S battery, the sulfur-based cathode is formed by using LLZO@C matrix and PEO binders, which successfully reduce the interfacial resistance between the sulfur and the ion/electron conductive matrix [236]. Thus, taking advantage of the composite cathode and CSE, this Li–S battery can deliver good specific capacities of more than 900, 1210, and 1556 mAh·g^{-1} at 37, 50, and 70 ℃, respectively, and capacity retention of 98.7% after 90 cycles.

7 Conclusions and future outlooks

Garnet-type solid electrolytes are focus of intensive research and interesting due to their high ionic conductivity, wide electrochemical window, and chemical stability against Li ions. These are one of the most promising solid electrolyte materials to be used in the future ASSLBs. ASSLBs using LLZO-based solid electrolyte are expected to solve the challenges presented in terms of energy density and safety of power battery. However, after years of development, the ionic conductivity of LLZO at RT is still lower than liquid electrolytes. Though ASSLBs have many advantages during research and development progress, there are still two main problems: the low performance of ionic conductivity of solid electrolyte at RT, and the interface contact with the positive and negative electrodes. Besides, there is a significant gap in our understanding of the mechanisms of Li-ion transport and related electrochemical and chemical reactions, as well as

structural and morphological properties, and thermodynamic behavior at ASSLB interfaces. Thus, research must be broadened by innovative *in-situ* characterization techniques and theoretical calculations. Despite LLZO/polymer CSE composite solid electrolyte, SCEs also have attracted attention due to their novel properties, such as suitable ionic conductivity and good thermal and electrochemical stability, as well as enhanced interface performance and mechanical properties. However, there are still many limitations to be solved in the development of suitable solid electrolytes for the future. The processing routes and synthesis techniques are not scalable and mass manufacturable for the large-production of such CSE and composite cathodes, representing a limitation in production processes. Until now, the cost of a solid-state lithium battery is still significantly greater than the cost of a liquid lithium battery. LLZO solid electrolyte ASSLBS also faces many material and technology issues, such as expansion during charge/discharge and the relation between mechanical properties of the solid electrolyte and its performance. The problems of manufacturing technologies have to be addressed in commercial development, design, and optimization of garnet-LLZO solid electrolytes.

Acknowledgements

This work is supported by the National Key R&D Program of China (Nos. 2018YFB0905600 and 2017YFB0310400), the National Natural Science Foundation of China (No. 51972246), Fundamental Research Funds for the Central Universities in China, State Key Laboratory of Advanced Electromagnetic Engineering and Technology (Huazhong University of Science and Technology), the "111" project (No. B13035), and the Science and Technology Project of Global Energy Interconnection Research Institute Co., Ltd. (No. SGGR0000WLJS1801080). We would like to thank Asst. Prof. Teresita Padilla-Benavides (Wesleyan University, USA) for help with the language editing.

References

[1] Chagnes A, Świątowska J. *Lithium Process Chemistry: Resources, Extraction, Batteries, and Recycling*. Amsterdam, the Netherlands: Elsevier, 2015.

[2] Scrosati B, Garche J. Lithium batteries: Status, prospects and future. *J Power Sources* 2010, **195**: 2419–2430.

[3] Lisbona D, Snee T. A review of hazards associated with primary lithium and lithium-ion batteries. *Protection 2*011, **89**: 434–442.

[4] Mauger A, Julien CM. Critical review on lithium-ion batteries: Are they safe? Sustainable? *Ionics* 2017, **23**: 1933–1947.

[5] Yang Z, Zhang J, Kintner-Meyer MCW, *et al.* Electrochemical energy storage for green grid. *Chem Rev* 2011, **111**: 3577–3613.

[6] Janek J, Zeier WG. A solid future for battery development. *Nat Energ*y, 2016, **1**: 16141.

[7] Goodenough JB, Kim Y. Challenges for rechargeable Li batteries. *Chem Mater* 2010, **22**: 587–603.

[8] Famprikis T, Canepa P, Dawson JA, *et al*. Fundamentals of inorganic solid-state electrolytes for batteries. *Nat Mater* 2019, **18**: 1278–1291.

[9] Zha W, Li J, Yang D, *et al.* Research advances of inorganic solid electrolyte $Li_7La_3Zr_2O_{12}$. *Materials China* 2017, **36**: 700–707.

[10] Thangadurai V, Weppner W. Recent progress in solid oxide and lithium ion conducting electrolytes research. *Ionics* 2006, **12**: 81–92.

[11] Knauth P. Inorganic solid Li ion conductors: An overview. *Solid State Ionics* 2009, **180**: 911–916.

[12] Wu MS, Xu B, Ouyang CY. Physics of electron and lithium-ion transport in electrode materials for Li-ion batteries. *Chinese Phys B* 2016, **25**: 018206.

[13] Wang YM, Song SF, Xu CH, *et al*. Development of solid-state electrolytes for sodium-ion battery-A short review. *Nano Mater Sci* 2019, **1**: 91–100.

[14] Deng Z, Mo YF, Ong SP. Computational studies of solid-state alkali conduction in rechargeable alkali-ion batteries. *NPG Asia Mater* 2016, **8**: e254.

[15] Anderson NL, Pramod Vedula R, Schultz PA, *et al*. Defect level distributions and atomic relaxations induced by charge trapping in amorphous silica. *Appl Phys Lett* 2012, **100**: 172908.

[16] Fu J. Fast Li^+ ion conducting glass-ceramics in the system Li_2O–Al_2O_3–GeO_2–P_2O_5. *Solid State Ionics* 1997, **104**: 191–194.

[17] Kim Y, Yoo A, Schmidt R, *et al*. Electrochemical stability of $Li_{6.5}La_3Zr_{1.5}M_{0.5}O_{12}$ (M = Nb or Ta) against metalic lithium. *Front Energy Res* 2016, **4**: 20.

[18] Inaguma Y, Chen LQ, Itoh M, *et al*. High ionic conductivity in lithium lanthanum titanate. *Solid State Commun* 1993, **86**: 689–693.

[19] Seino Y, Ota T, Takada K, *et al*. A sulphide lithium super ion conductor is superior to liquid ion conductors for use in rechargeable batteries. *Energy Environ Sci* 2014, **7**: 627–631.

[20] Kamaya N, Homma K, Yamakawa Y, *et al*. A lithium superionic conductor. *Nat Mater* 2011, **10**: 682–686.

[21] Zhu YZ, He XF, Mo YF. Origin of outstanding stability in the lithium solid electrolyte materials: Insights from thermodynamic analyses based on first-principles calculations. *ACS Appl Mater Interfaces* 2015, **7**: 23685–23693.

[22] Zhu YZ, He XF, Mo YF. First principles study on electrochemical and chemical stability of solid electrolyte–electrode interfaces in all-solid-state Li-ion batteries. *J Mater Chem A* 2016, **4**: 3253–3266.

[23] Dong B, Yeandel SR, Goddard P, *et al*. Combined experimental and computational study of Ce-doped $La_3Zr_2Li_7O_{12}$ garnet solid-state electrolyte. *Chem Mater* 2020, **32**: 215–223.

[24] Thangadurai V, Kaack H, Weppner WJF. Novel fast lithium ion conduction in garnet-type $Li_5La_3M_2O_{12}$ (M = Nb, Ta). *J Am Ceram Soc* 2003, **86**: 437–440.

[25] Thangadurai V, Pinzaru D, Narayanan S, *et al*. Fast solid-state Li ion conducting garnet-type structure metal oxides for energy storage. *J Phys Chem Lett* 2015, **6**: 292–299.

[26] Thangadurai V, Weppner W. $Li_6ALa_2Nb_2O_{12}$ (A=Ca, Sr, Ba): A new class of fast lithium ion conductors with garnet-like structure. *J Am Ceram Soc* 2005, **88**: 411–418.

[27] Abbattista F, Vallino M, Mazza D. Remarks on the binary systems Li_2O–Me_2O_5 (Me=Nb, Ta). *Mater Res Bull* 1987, **22**: 1019–1027.

[28] Hyooma H, Hayashi K. Crystal structures of $La_3Li_5M_2O_{12}$ (M=Nb, Ta). *Mater Res Bull* 1988, **23**: 1399–1407.

[29] Ramakumar S, Deviannapoorani C, Dhivya L, *et al*. Lithium garnets: Synthesis, structure, Li^+ conductivity, Li^+ dynamics and applications. *Prog Mater Sci* 2017, **88**: 325–411.

[30] Thompson T, Wolfenstine J, Allen JL, *et al*. Tetragonal vs. cubic phase stability in Al-free Ta doped $Li_7La_3Zr_2O_{12}$ (LLZO). *J Mater Chem A* 2014, **2**: 13431–13436.

[31] Xu M, Park MS, Lee JM, *et al*. Mechanisms of Li^+ transport in garnet-type cubic $Li_{3+x}La_3M_2O_{12}$ (M = Te, Nb, Zr). *Phys Rev B* 2012, **85**: 052301.

[32] Miara LJ, Ong SP, Mo YF, *et al*. Effect of Rb and Ta doping on the ionic conductivity and stability of the garnet $Li_{7+2x-y}(La_{3-x}Rb_x)(Zr_{2-y}Ta_y)O_{12}$ ($0 \leqslant x \leqslant 0.375$, $0 \leqslant y \leqslant 1$) superionic conductor: A first principles investigation. *Chem Mater* 2013, **25**: 3048–3055.

[33] Murugan R, Thangadurai V, Weppner W. Fast lithium ion conduction in garnet-type $Li_7La_3Zr_2O_{12}$. *Angew Chem Int Ed* 2007, **46**: 7778–7781.

[34] Thangadurai V, Narayanan S, Pinzaru D. Garnet-type solid-state fast Li ion conductors for Li batteries: Critical review. *Chem Soc Rev* 2014, **43**: 4714.

[35] Kotobuki M, Munakata H, Kanamura K, *et al*. Compatibility of $Li_7La_3Zr_2O_{12}$ solid electrolyte to all-solid-state battery using Li metal anode. *J Electrochem Soc* 2010, **157**: A1076.

[36] Dirican M, Yan CY, Zhu P, *et al*. Composite solid electrolytes for all-solid-state lithium batteries. *Mater Sci Eng*: *R*: *Rep* 2019, **136**: 27–46.

[37] Zhou WD, Wang SF, Li YT, *et al*. Plating a dendrite-free lithium anode with a polymer/ceramic/polymer sandwich electrolyte. *J Am Chem Soc* 2016, **138**: 9385–9388.

[38] Zhong YR, Xie YJ, Hwang S, *et al*. A highly efficient all-solid-state lithium/electrolyte interface induced by an energetic reaction. *Angew Chem Int Ed* 2020, **59**: 14003–14008.

[39] Zhu YL, Wu S, Pan YL, *et al*. Reduced energy barrier for Li^+ transport across grain boundaries with amorphous domains in LLZO thin films. *Nanoscale Res Lett* 2020, **15**: 1–8.

[40] Xia SX, Wu XS, Zhang ZC, *et al*. Practical challenges and future perspectives of all-solid-state lithium-metal batteries. *Chem* 2019, **5**: 753–785.

[41] Wells AF. *Structural Inorganic Chemistry*. Oxford University Press, 2012.

[42] Awaka J, Kijima N, Hayakawa H, *et al*. Synthesis and structure analysis of tetragonal $Li_7La_3Zr_2O_{12}$ with the garnet-related type structure. *J Solid State Chem* 2009, **182**: 2046–2052.

[43] Bernstein N, Johannes MD, Hoang K. Origin of the structural phase transition in $Li_7La_3Zr_2O_{12}$. *Phys Rev Lett* 2012, **109**: 205702.

[44] Zhao Y, Yan JH, Cai WP, *et al*. Elastic and well-aligned ceramic LLZO nanofiber based electrolytes for solid-state lithium batteries. *Energy Storage Mater* 2019, **23**: 306–313.

[45] Aktaş S, Özkendir OM, Eker YR, *et al*. Study of the local structure and electrical properties of gallium substituted LLZO electrolyte materials. *J Alloys Compd* 2019, **792**: 279–285.

[46] Murugan R, Thangadurai V, Weppner W. Lattice parameter and sintering temperature dependence of bulk and grain-boundary conduction of garnet-like solid Li-electrolytes. *J Electrochem Soc* 2008, **155**: A90.

[47] Awaka J, Takashima A, Kataoka K, *et al*. Crystal structure of fast lithium-ion-conducting cubic $Li_7La_3Zr_2O_{12}$. *Chem Lett* 2011, **40**: 60–62.

[48] Ohta S, Kobayashi T, Asaoka T. High lithium ionic conductivity in the garnet-type oxide $Li_{7-X}La_3(Zr_{2-X}, Nb_X)O_{12}$ (X = 0–2). *J Power Sources* 2011, **196**: 3342–3345.

[49] Rettenwander D, Geiger CA, Tribus M, *et al*. A synthesis and crystal chemical study of the fast ion conductor $Li_{7-3x}Ga_xLa_3Zr_2O_{12}$ with x = 0.08 to 0.84. *Inorg Chem* 2014, **53**: 6264–6269.

[50] Chen F, Li JY, Huang ZF, *et al*. Origin of the phase transition in lithium garnets. *J Phys Chem C* 2018, **122**: 1963–1972.

[51] Meier K, Laino T, Curioni A. Solid-state electrolytes: Revealing the mechanisms of Li-ion conduction in tetragonal and cubic LLZO by first-principles calculations. *J Phys Chem C* 2014, **118**: 6668–6679.

[52] Kazyak E, Chen KH, Wood KN, *et al*. Atomic layer deposition of the solid electrolyte garnet $Li_7La_3Zr_2O_{12}$. *Chem Mater* 2017, **29**: 3785–3792.

[53] Adams S, Rao RP. Ion transport and phase transition in $Li_{7-x}La_3(Zr_{2-x}M_x)O_{12}$ ($M = Ta^{5+}$, Nb^{5+}, x = 0, 0.25). *J Mater Chem* 2012, **22**: 1426–1434.

[54] O'Callaghan MP, Cussen EJ. Lithium dimer formation in the Li-conducting garnets $Li_{5+x}Ba_xLa_{3-x}Ta_2O_{12}$ ($0 < x \leq 1.6$). *Chem Commun* 2007: 2048–2050.

[55] Janani N, Deviannapoorani C, Dhivya L, *et al*. Influence of sintering additives on densification and Li^+ conductivity of Al doped $Li_7La_3Zr_2O_{12}$ lithium garnet. *RSC Adv* 2014, **4**: 51228–51238.

[56] Larraz G, Orera A, Sanjuán ML. Cubic phases of garnet-type $Li_7La_3Zr_2O_{12}$: The role of hydration. *J Mater Chem A* 2013, **1**: 11419.

[57] Dhivya L, Murugan R. Effect of simultaneous substitution of Y and Ta on the stabilization of cubic phase, microstructure, and Li^+ conductivity of $Li_7La_3Zr_2O_{12}$ lithium garnet. *ACS Appl Mater Interfaces* 2014, **6**: 17606–17615.

[58] Hubaud AA, Schroeder DJ, Key B, *et al*. Low temperature stabilization of cubic $(Li_{7-x}Al_{x/3})La_3Zr_2O_{12}$: Role of aluminum during formation. *J Mater Chem A* 2013, **1**: 8813.

[59] Geiger CA, Alekseev E, Lazic B, *et al*. Crystal chemistry and stability of "$Li_7La_3Zr_2O_{12}$" garnet: A fast lithium-ion conductor. *Inorg Chem* 2011, **50**: 1089–1097.

[60] Dumon A, Huang M, Shen Y, *et al*. High Li ion conductivity in strontium doped $Li_7La_3Zr_2O_{12}$ garnet. *Solid State Ionics* 2013, **243**: 36–41.

[61] Ramakumar S, Satyanarayana L, Manorama SV, *et al*. Structure and Li^+ dynamics of Sb-doped $Li_7La_3Zr_2O_{12}$ fast lithium ion conductors. *Phys Chem Chem Phys* 2013, **15**: 11327.

[62] Rangasamy E, Wolfenstine J, Sakamoto J. The role of Al and Li concentration on the formation of cubic garnet solid electrolyte of nominal composition $Li_7La_3Zr_2O_{12}$. *Solid State Ionics* 2012, **206**: 28–32.

[63] Botros M, Djenadic R, Clemens O, *et al*. Field assisted sintering of fine-grained $Li_{7-3x}La_3Zr_2Al_xO_{12}$ solid electrolyte and the influence of the microstructure on the electrochemical performance. *J Power Sources* 2016, **309**: 108–115.

[64] Cheng L, Chen W, Kunz M, *et al*. Effect of surface microstructure on electrochemical performance of garnet solid electrolytes. *ACS Appl Mater Interfaces* 2015, **7**: 2073–2081.

[65] Zhang YH, Chen F, Tu R, *et al*. Field assisted sintering of dense Al-substituted cubic phase $Li_7La_3Zr_2O_{12}$ solid electrolytes. *J Power Sources* 2014, **268**: 960–964.

[66] Sakamoto J, Rangasamy E, Kim H, *et al*. Synthesis of nano-scale fast ion conducting cubic $Li_7La_3Zr_2O_{12}$. *Nanotechnology* 2013, **24**: 424005.

[67] Li YQ, Wang Z, Cao Y, *et al*. W-doped $Li_7La_3Zr_2O_{12}$ ceramic electrolytes for solid state Li-ion batteries. *Electrochimica Acta* 2015, **180**: 37–42.

[68] Kokal I, Somer M, Notten PHL, *et al*. Sol–gel synthesis and lithium ion conductivity of $Li_7La_3Zr_2O_{12}$ with garnet-related type structure. *Solid State Ionics* 2011, **185**: 42–46.

[69] Tsai CL, Roddatis V, Chandran CV, *et al*. $Li_7La_3Zr_2O_{12}$ interface modification for Li dendrite prevention. *ACS Appl Mater Interfaces* 2016, **8**: 10617–10626.

[70] Fu KK, Gong Y, Liu B, *et al*. Toward garnet electrolyte-based Li metal batteries: An ultrathin, highly effective, artificial solid-state electrolyte/metallic Li interface. *Sci Adv* 2017, **3**: e1601659.

[71] Yang T, Gordon ZD, Li Y, *et al*. Nanostructured garnet-type solid electrolytes for lithium batteries: Electrospinning synthesis of $Li_7La_3Zr_2O_{12}$ nanowires and particle size-dependent phase transformation. *J Phys Chem C* 2015, **119**: 14947–14953.

[72] Reinacher J, Berendts S, Janek J. Preparation and electrical properties of garnet-type $Li_6BaLa_2Ta_2O_{12}$ lithium solid electrolyte thin films prepared by pulsed laser deposition. *Solid State Ionics* 2014, **258**: 1–7.

[73] Djenadic R, Botros M, Benel C, *et al*. Nebulized spray pyrolysis of Al-doped $Li_7La_3Zr_2O_{12}$ solid electrolyte for battery applications. *Solid State Ionics* 2014, **263**: 49–56.

[74] Hu ZL, Liu HD, Ruan HB, *et al*. High Li-ion conductivity of Al-doped $Li_7La_3Zr_2O_{12}$ synthesized by solid-state reaction. *Ceram Int* 2016, **42**: 12156–12160.

[75] El-Shinawi H, Paterson GW, MacLaren DA, *et al*. Low-temperature densification of Al-doped $Li_7La_3Zr_2O_{12}$: A reliable and controllable synthesis of fast-ion conducting garnets. *J Mater Chem A* 2017, **5**: 319–329.

[76] Chen RJ, Huang M, Huang WZ, *et al*. Sol–gel derived Li–La–Zr–O thin films as solid electrolytes for lithium-ion batteries. *J Mater Chem A* 2014, **2**: 13277.

[77] Baek SW, Lee JM, Kim TY, *et al*. Garnet related lithium ion conductor processed by spark plasma sintering for all solid state batteries. *J Power Sources* 2014, **249**: 197–206.

[78] Kali R, Mukhopadhyay A. Spark plasma sintered/ synthesized dense and nanostructured materials for solid-state Li-ion batteries: Overview and perspective. *J Power Sources* 2014, **247**: 920–931.

[79] Sun CW, Liu J, Gong YD, *et al*. Recent advances in all-solid-state rechargeable lithium batteries. *Nano Energy* 2017, **33**: 363–386.

[80] Jin Y, McGinn PJ. $Li_7La_3Zr_2O_{12}$ electrolyte stability in air and fabrication of a $Li/Li_7La_3Zr_2O_{12}/Cu_{0.1}V_2O_5$ solid-state battery. *J Power Sources* 2013, **239**: 326–331.

[81] Galven C, Wu CH, Jarry A, *et al.* Interrelationships among gain size, surface composition air stability, and interfacial resistance of Al-substituted $Li_7La_3Zr_2O_{12}$ solid electrolytes. *ACS Appl Mater Interfaces* 2015, **7**: 17649–17655.

[82] Cheng L, Crumlin EJ, Chen W, *et al*. The origin of high electrolyte–electrode interfacial resistances in lithium cells containing garnet type solid electrolytes. *Phys Chem Chem Phys* 2014, **16**: 18294–18300.

[83] Sharafi A, Yu S, Naguib M, *et al*. Impact of air exposure and surface chemistry on $Li–Li_7La_3Zr_2O_{12}$ interfacial resistance. *J Mater Chem A* 2017, **5**: 13475–13487.

[84] Xia WH, Xu BY, Duan HN, *et al*. Reaction mechanisms of lithium garnet pellets in ambient air: The effect of

humidity and CO_2. *J Am Ceram Soc* 2017, **100**: 2832–2839.

[85] Yow ZF, Oh YL, Gu WY, *et al*. Effect of Li^+/H^+ exchange in water treated Ta-doped $Li_7La_3Zr_2O_{12}$. *Solid State Ionics* 2016, **292**: 122–129.

[86] Ramaswamy M, Werner W. *Solid Electrolytes for Advanced Applications*. Springer Nature Switzerland, 2019.

[87] Kobi S, Mukhopadhyay A. Structural (in)stability and spontaneous cracking of Li–La–zirconate cubic garnet upon exposure to ambient atmosphere. *J Eur Ceram Soc* 2018, **38**: 4707–4718.

[88] Xia WH, Xu BY, Duan HN, *et al*. Ionic conductivity and air stability of Al-doped $Li_7La_3Zr_2O_{12}$ sintered in alumina and Pt crucibles. *ACS Appl Mater Interfaces* 2016, **8**: 5335–5342.

[89] Li YT, Chen X, Dolocan A, *et al*. Garnet electrolyte with an ultralow interfacial resistance for Li-metal batteries. *J Am Chem Soc* 2018, **140**: 6448–6455.

[90] Ruan YD, Lu Y, Huang X, *et al*. Acid induced conversion towards a robust and lithiophilic interface for Li–$Li_7La_3Zr_2O_{12}$ solid-state batteries. *J Mater Chem A* 2019, **7**: 14565–14574.

[91] Abdel-Basset DM, Mulmi S, El-Bana MS, *et al*. Structure, ionic conductivity, and dielectric properties of Li-rich garnet-type $Li_{5+2x}La_3Ta_{2-x}Sm_xO_{12}$ ($0 \le x \le 0.55$) and their chemical stability. *Inorg Chem* 2017, **56**: 8865–8877.

[92] Li YT, Han JT, Wang CA, *et al*. Optimizing Li^+ conductivity in a garnet framework. *J Mater Chem* 2012, **22**: 15357.

[93] Wu JF, Chen EY, Yu Y, *et al*. Gallium-doped $Li_7La_3Zr_2O_{12}$ garnet-type electrolytes with high lithium-ion conductivity. *ACS Appl Mater Interfaces* 2017, **9**: 1542–1552.

[94] Kihira Y, Ohta S, Imagawa H, *et al*. Effect of simultaneous substitution of alkali earth metals and Nb in $Li_7La_3Zr_2O_{12}$ on lithium-ion conductivity. *ECS Electrochem Lett* 2013, **2**: A56–A59.

[95] Rangasamy E, Wolfenstine J, Allen J, *et al*. The effect of 24c-site (A) cation substitution on the tetragonal-cubic phase transition in $Li_{7-x}La_{3-x}AxZr_2O_{12}$ garnet-based ceramic electrolyte. *J Power Sources* 2013, **230**: 261–266.

[96] Thangadurai V, Weppner W. Effect of sintering on the ionic conductivity of garnet-related structure $Li_5La_3Nb_2O_{12}$ and In- and K-doped $Li_5La_3Nb_2O_{12}$. *J Solid State Chem* 2006, **179**: 974–984.

[97] Xiang X, Chen F, Shen Q, *et al*. Effect of the lithium ion concentration on the lithium ion conductivity of Ga-doped LLZO. *Mater Res Express* 2019, **6**: 085546.

[98] Xiang X, Liu Y, Chen F, *et al*. Crystal structure and lithium ionic transport behavior of Li site doped $Li_7La_3Zr_2O_{12}$. *J Eur Ceram Soc* 2020, **40**: 3065–3071.

[99] Xie H, Alonso JA, Li YT, *et al*. Lithium distribution in aluminum-free cubic $Li_7La_3Zr_2O_{12}$. *Chem Mater* 2011, **23**: 3587–3589.

[100] Wagner R, Redhammer GJ, Rettenwander D, *et al*. Fast Li-ion-conducting garnet-related $Li_{7-3x}Fe_xLa_3Zr_2O_{12}$ with uncommon *I*43*d* structure. *Chem Mater* 2016, **28**: 5943–5951.

[101] Rettenwander D, Redhammer G, Preishuber-Pflügl F, *et al*. Structural and electrochemical consequences of Al and Ga cosubstitution in $Li_7La_3Zr_2O_{12}$ solid electrolytes. *Chem Mater* 2016, **28**: 2384–2392.

[102] Nonemacher JF, Hüter C, Zheng H, *et al*. Microstructure and properties investigation of garnet structured $Li_7La_3Zr_2O_{12}$ as electrolyte for all-solid-state batteries. *Solid State Ionics* 2018, **321**: 126–134.

[103] Jiang Y, Zhu XH, Qin SY, *et al*. Investigation of Mg^{2+}, Sc^{3+} and Zn^{2+} doping effects on densification and ionic conductivity of low-temperature sintered $Li_7La_3Zr_2O_{12}$ garnets. *Solid State Ionics* 2017, **300**: 73–77.

[104] Nemori H, Matsuda Y, Mitsuoka S, *et al*. Stability of garnet-type solid electrolyte $Li_xLa_3A_{2-y}B_yO_{12}$ (A = Nb or Ta, B = Sc or Zr). *Solid State Ionics* 2015, **282**: 7–12.

[105] Tong X, Thangadurai V, Wachsman ED. Highly conductive Li garnets by a multielement doping strategy. *Inorg Chem* 2015, **54**: 3600–3607.

[106] Song SD, Chen BT, Ruan YL, *et al*. Gd-doped $Li_7La_3Zr_2O_{12}$ garnet-type solid electrolytes for all-solid-state Li-ion batteries. *Electrochimica Acta* 2018, **270**: 501–508.

[107] Gupta A, Murugan R, Paranthaman MP, *et al*. Optimum lithium-ion conductivity in cubic $Li_{7-x}La_3Hf_{2-x}Ta_xO_{12}$. *J Power Sources* 2012, **209**: 184–188.

[108] Dhivya L, Janani N, Palanivel B, *et al*. Li^+ transport properties of W substituted $Li_7La_3Zr_2O_{12}$ cubic lithium garnets. *AIP Adv* 2013, **3**: 082115.

[109] Deviannapoorani C, Dhivya L, Ramakumar S, *et al*. Lithium ion transport properties of high conductive tellurium substituted $Li_7La_3Zr_2O_{12}$ cubic lithium garnets. *J Power Sources* 2013, **240**: 18–25.

[110] Gai JL, Zhao EQ, Ma FR, *et al*. Improving the Li-ion conductivity and air stability of cubic $Li_7La_3Zr_2O_{12}$ by the co-doping of Nb, Y on the Zr site. *J Eur Ceram Soc* 2018, **38**: 1673–1678.

[111] Zhang YH, Deng JD, Hu DW, *et al*. Synergistic regulation of garnet-type Ta-doped $Li_7La_3Zr_2O_{12}$ solid electrolyte by Li^+ concentration and Li^+ transport channel size. *Electrochimica Acta* 2019, **296**: 823–829.

[112] Wu JF, Pang WK, Peterson VK, *et al*. Garnet-type fast Li-ion conductors with high ionic conductivities for all-solid-state batteries. *ACS Appl Mater Interfaces* 2017, **9**: 12461–12468.

[113] Buannic L, Orayech B, López del Amo JM, *et al*. Dual substitution strategy to enhance Li^+ ionic conductivity in $Li_7La_3Zr_2O_{12}$ solid electrolyte. *Chem Mater* 2017, **29**: 1769–1778.

[114] Wang DW, Zhong GM, Pang WK, *et al*. Toward understanding the lithium transport mechanism in garnet-type solid electrolytes: Li^+ ion exchanges and their mobility at octahedral/tetrahedral sites. *Chem Mater* 2015,

27: 6650–6659.

[115] Thompson T, Sharafi A, Johannes MD, *et al*. A tale of two sites: On defining the carrier concentration in garnet-based ionic conductors for advanced Li batteries. *Adv Energy Mater* 2015, **5**: 1500096.

[116] Kim S, Hirayama M, Taminato S, *et al*. Epitaxial growth and lithium ion conducntivity of lithium oxide garnet for an all solid-state battery electrolyte. *RSC Dalton Trans* 2013, **42**: 13112–13117.

[117] Liu K, Ma JT, Wang CG. Excess lithium salt functions more than compensating for lithium loss when synthesizing $Li_{6.5}La_3Ta_{0.5}Zr_{1.5}O_{12}$ in alumina crucible. *J Power Sources* 2014, **260**: 109–114.

[118] Cussen EJ. Structure and ionic conductivity in lithium garnets. *J Mater Chem* 2010, **20**: 5167.

[119] Samson AJ, Hofstetter K, Bag S, *et al*. A bird's-eye view of Li-stuffed garnet-type $Li_7La_3Zr_2O_{12}$ ceramic electrolytes for advanced all-solid-state Li batteries. *Energy Environ Sci* 2019, **12**: 2957–2975.

[120] Zeier WG. Structural limitations for optimizing garnet-type solid electrolytes: A perspective. *Dalton Trans* 2014, **43**: 16133–16138.

[121] Qin SY, Zhu XH, Jiang Y, *et al*. Growth of self-textured Ga^{3+}-substituted $Li_7La_3Zr_2O_{12}$ ceramics by solid state reaction and their significant enhancement in ionic conductivity. *Appl Phys Lett* 2018, **112**: 113901.

[122] Baral AK, Narayanan S, Ramezanipour F, *et al*. Evaluation of fundamental transport properties of Li-excess garnet-type $Li_{5+2x}La_3Ta_{2-x}Y_xO_{12}$ (x = 0.25, 0.5 and 0.75) electrolytes using AC impedance and dielectric spectroscopy. *Phys Chem Chem Phys* 2014, **16**: 11356.

[123] Kuhn A, Narayanan S, Spencer L, *et al*. Li self-diffusion in garnet-type $Li_7La_3Zr_2O_{12}$ as probed directly by diffusion-induced ^{7}Li spin-lattice relaxation NMR spectroscopy. *Phys Rev B* 2011, **83**: 094302.

[124] van Wüllen L, Echelmeyer T, Meyer HW, *et al*. The mechanism of Li-ion transport in the garnet $Li_5La_3Nb_2O_{12}$. *Phys Chem Chem Phys* 2007, **9**: 3298–3303.

[125] Adachi GY, Imanaka N, Aono H. Fast Li⊕ conducting ceramic electrolytes. *Adv Mater* 1996, **8**: 127–135.

[126] Mukhopadhyay S, Thompson T, Sakamoto J, *et al*. Structure and stoichiometry in supervalent doped $Li_7La_3Zr_2O_{12}$. *Chem Mater* 2015, **27**: 3658–3665.

[127] Kotobuki M, Kanamura K, Sato Y, *et al*. Fabrication of all-solid-state lithium battery with lithium metal anode using Al_2O_3-added $Li_7La_3Zr_2O_{12}$ solid electrolyte. *J Power Sources* 2011, **196**: 7750–7754.

[128] Rettenwander D, Blaha P, Laskowski R, *et al*. DFT study of the role of Al^{3+} in the fast ion-conductor $Li_{7-3x}Al_{3+x}La_3Zr_2O_{12}$ garnet. *Chem Mater* 2014, **26**: 2617–2623.

[129] Rettenwander D, Langer JL, Schmidt W, *et al*. Site occupation of Ga and Al in stabilized cubic $Li_{7-3(x+y)}Ga_xAl_yLa_3Zr_2O_{12}$ garnets as deduced from ^{27}Al and ^{71}Ga MAS NMR at ultrahigh magnetic fields. *Chem Mater* 2015, **27**: 3135–3142.

[130] Dash U, Sahoo S, Parashar SKS, *et al*. Effect of Li^+ ion mobility on the grain boundary conductivity of Li_2TiO_3 nanoceramics. *J Adv Ceram* 2014, **3**: 98–108.

[131] Huang M, Liu T, Deng YF, *et al*. Effect of sintering temperature on structure and ionic conductivity of $Li_{7-x}La_3Zr_2O_{12-0.5x}$ (x = 0.5~0.7) ceramics. *Solid State Ionics* 2011, **204–205**: 41–45.

[132] García Daza FA, Bonilla MR, Llordés A, *et al*. Atomistic insight into ion transport and conductivity in Ga/Al-substituted $Li_7La_3Zr_2O_{12}$ solid electrolytes. *ACS Appl Mater Interfaces* 2019, **11**: 753–765.

[133] Wagner R, Redhammer GJ, Rettenwander D, *et al.* Crystal structure of garnet-related Li-ion conductor $Li_{7-3x}Ga_xLa_3Zr_2O_{12}$: Fast Li-ion conduction caused by a different cubic modification? *Chem Mater* 2016, **28**: 1861–1871.

[134] Nolan AM, Zhu Y, He X, *et al*. Computation-accelerated design of materials and interfaces for all-solid state lithium-ion batteries. *Joule* 2018, **2**: 2016–2046.

[135] Song SF, Kotobuki M, Zheng F, *et al*. Roles of alkaline earth ions in garnet-type superionic conductors. *ChemElectroChem* 2017, **4**: 266–271.

[136] Bachman JC, Muy S, Grimaud A, *et al*. Inorganic solid-state electrolytes for lithium batteries: Mechanisms and properties governing ion conduction. *Chem Rev* 2016, **116**: 140–162.

[137] Wang Y, Richards WD, Ong SP, *et al*. Design principles for solid-state lithium superionic conductors. *Nat Mater* 2015, **14**: 1026–1031.

[138] Zhang YH, Hu DW, Deng JD, *et al*. Li^+ transport channel size governing Li^+ migration in garnet-based all-solid-state lithium batteries. *J Alloys Compd* 2018, **767**: 899–904.

[139] Xiang X, Chen F, Yang WY, *et al*. Dual regulation of Li^+ migration of $Li_{6.4}La_3Zr_{1.4}M_{0.6}O_{12}$ (M = Sb, Ta, Nb) by bottleneck size and bond length of M−O. *J Am Ceram Soc* 2020, **103**: 2483–2490.

[140] Zhang YH, Chen F, Li JY, *et al*. Regulation mechanism of bottleneck size on Li^+ migration activation energy in garnet-type $Li_7La_3Zr_2O_{12}$. *Electrochimica Acta* 2018, **261**: 137–142.

[141] Miara LJ, Richards WD, Wang YE, *et al*. First-principles studies on cation dopants and Electrolyte|Cathode interphases for lithium garnets. *Chem Mater* 2015, **27**: 4040–4047.

[142] Bernuy-Lopez C, Manalastas W, Lopez del Amo JM, *et al*. Atmosphere controlled processing of Ga-substituted garnets for high Li-ion conductivity ceramics. *Chem Mater* 2014, **26**: 3610–3617.

[143] Zeier WG, Zhou SL, Lopez-Bermudez B, *et al*. Dependence of the Li-ion conductivity and activation energies on the crystal structure and ionic radii in $Li_6MLa_2Ta_2O_{12}$. *ACS Appl Mater Interfaces* 2014, **6**: 10900–10907.

[144] Jalem R, Rushton MJD, Manalastas W, *et al*. Effects of

gallium doping in garnet-type $Li_7La_3Zr_2O_{12}$ solid electrolytes. *Chem Mater* 2015, **27**: 2821–2831.

[145] Santosh KC, Longo RC, Xiong K, *et al*. Electrode-electrolyte interface for solid state Li-ion batteries: Point defects and mechanical strain. *J Electrochem Soc* 2014, **161**: F3104–F3110.

[146] Kim DH, Kim MY, Yang SH, *et al*. Fabrication and electrochemical characteristics of NCM-based all-solid lithium batteries using nano-grade garnet Al-LLZO powder. *J Ind Eng Chem* 2019, **71**: 445–451.

[147] Chen F, Zha WP, Yang DJ, *et al*. All-solid-state lithium battery fitted with polymer electrolyte enhanced by solid plasticizer and conductive ceramic filler. *J Electrochem Soc* 2018, **165**: A3558–A3565.

[148] Chen L, Li YT, Li SP, *et al*. PEO/garnet composite electrolytes for solid-state lithium batteries: From "ceramic-in-polymer" to "polymer-in-ceramic". *Nano Energy* 2018, **46**: 176–184.

[149] Luo W, Gong YH, Zhu YZ, *et al*. Reducing interfacial resistance between garnet-structured solid-state electrolyte and Li-metal anode by a germanium layer. *Adv Mater* 2017, **29**: 1606042.

[150] Han XG, Gong YH, Fu K, *et al*. Negating interfacial impedance in garnet-based solid-state Li metal batteries. *Nat Mater* 2017, **16**: 572–579.

[151] Van den Broek J, Afyon S, Rupp JLM. Interface-engineered all-solid-state Li-ion batteries based on garnet-type fast Li^+ conductors. *Adv Energy Mater* 2016, **6**: 1600736.

[152] Li YT, Chen X, Dolocan A, *et al*. Garnet electrolyte with an ultralow interfacial resistance for Li-metal batteries. *J Am Chem Soc* 2018, **140**: 6448–6455.

[153] Duan J, Wu WY, Nolan AM, *et al*. Lithium-graphite paste: An interface compatible anode for solid-state batteries. *Adv Mater* 2019, **31**: 1807243.

[154] Fu KK, Gong YH, Dai JQ, *et al*. Flexible, solid-state, ion-conducting membrane with 3D garnet nanofiber networks for lithium batteries. *PNAS* 2016, **113**: 7094–7099.

[155] Zhang YH, Chen F, Yang DJ, *et al*. High capacity all-solid-state lithium battery using cathodes with three-dimensional Li^+ conductive network. *J Electrochem Soc* 2017, **164**: A1695–A1702.

[156] Zhang YH, Chen F, Tu R, *et al*. Effect of lithium ion concentration on the microstructure evolution and its association with the ionic conductivity of cubic garnet-type nominal $Li_7Al_{0.25}La_3Zr_2O_{12}$ solid electrolytes. *Solid State Ionics* 2016, **284**: 53–60.

[157] Cheng SHS, He KQ, Liu Y, *et al*. Electrochemical performance of all-solid-state lithium batteries using inorganic lithium garnets particulate reinforced PEO/$LiClO_4$ electrolyte. *Electrochimica Acta* 2017, **253**: 430–438.

[158] Zha WP, Chen F, Yang DJ, *et al*. High-performance $Li_{6.4}La_3Zr_{1.4}Ta_{0.6}O_{12}$/poly(ethylene oxide)/succinonitrile composite electrolyte for solid-state lithium batteries. *J Power Sources* 2018, **397**: 87–94.

[159] Yang CP, Xie H, Ping WW, *et al*. An electron/ion dual-conductive alloy framework for high-rate and high-capacity solid-state lithium-metal batteries. *Adv Mater* 2019, **31**: 1804815.

[160] Ci JL, Cao C, Kuga S, *et al*. Improved performance of microbial fuel cell using esterified corncob cellulose nanofibers to fabricate air-cathode gas diffusion layer. *ACS Sustain Chem Eng* 2017, **5**: 9614–9618.

[161] Li YT, Xu BY, Xu HH, *et al*. Hybrid polymer/garnet electrolyte with a small interfacial resistance for lithium-ion batteries. *Angew Chem Int Ed* 2017, **56**: 753–756.

[162] Zha W, Xu Y, Chen F, *et al*. Cathode/electrolyte interface engineering via wet coating and hot pressing for all-solid-state lithium battery. *Solid State Ionics* 2019, **330**: 54–59.

[163] Zhang JJ, Zang X, Wen HJ, *et al*. High-voltage and free-standing poly(propylene carbonate)/$Li_{6.75}La_3Zr_{1.75}Ta_{0.25}O_{12}$ composite solid electrolyte for wide temperature range and flexible solid lithium ion battery. *J Mater Chem A* 2017, **5**: 4940–4948.

[164] Yu S, Schmidt RD, Garcia-Mendez R, *et al*. Elastic properties of the solid electrolyte $Li_7La_3Zr_2O_{12}$ (LLZO). *Chem Mater* 2016, **28**: 197–206.

[165] Yu S, Siegel DJ. Grain boundary contributions to Li-ion transport in the solid electrolyte $Li_7La_3Zr_2O_{12}$ (LLZO). *Chem Mater* 2017, **29**: 9639–9647.

[166] Ohta S, Kobayashi T, Seki J, *et al*. Electrochemical performance of an all-solid-state lithium ion battery with garnet-type oxide electrolyte. *J Power Sources* 2012, **202**: 332–335.

[167] Ohta S, Seki J, Yagi Y, *et al*. Co-sinterable lithium garnet-type oxide electrolyte with cathode for all-solid-state lithium ion battery. *J Power Sources* 2014, **265**: 40–44.

[168] Feng LL, Li L, Zhang YQ, *et al*. Low temperature synthesis and ion conductivity of $Li_7La_3Zr_2O_{12}$ garnets for solid state Li ion batteries. *Solid State Ionics* 2017, **310**: 129–133.

[169] Yan XF, Li ZB, Wen ZY, *et al*. Li/$Li_7La_3Zr_2O_{12}$/$LiFePO_4$ all-solid-state battery with ultrathin nanoscale solid electrolyte. *J Phys Chem C* 2017, **121**: 1431–1435.

[170] Liu B, Zhang JG, Xu W. Advancing lithium metal batteries. *Joule* 2018, **2**: 833–845.

[171] Han XG, Gong YH, Fu K, *et al*. Negating interfacial impedance in garnet-based solid-state Li metal batteries. *Nat Mater* 2017, **16**: 572–579.

[172] Wang CW, Gong YH, Liu BY, *et al*. Conformal, nanoscale ZnO surface modification of garnet-based solid-state electrolyte for lithium metal anodes. *Nano Lett* 2017, **17**: 565–571.

[173] He MH, Cui ZH, Chen C, *et al*. Formation of self-limited, stable and conductive interfaces between garnet electrolytes and lithium anodes for reversible lithium cycling in solid-state batteries. *J Mater Chem A* 2018, **6**:

11463–11470.

[174] Zhao N, Fang R, He MH, *et al*. Cycle stability of lithium/garnet/lithium cells with different intermediate layers. *Rare Metal* 2018, **37**: 473–479.

[175] Richards WD, Miara LJ, Wang Y, *et al*. Interface stability in solid-state batteries. *Chem Mater* 2016, **28**: 266–273.

[176] Inada R, Yasuda S, Hosokawa H, *et al*. Formation and stability of interface between garnet-type Ta-doped $Li_7La_3Zr_2O_{12}$ solid electrolyte and lithium metal electrode. *Batteries* 2018, **4**: 26.

[177] Ma C, Cheng YQ, Yin KB, *et al*. Interfacial stability of Li metal-solid electrolyte elucidated via *in situ* electron microscopy. *Nano Lett* 2016, **16**: 7030–7036.

[178] Sharafi A, Kazyak E, Davis AL, *et al.* Surface chemistry mechanism of ultra-low interfacial resistance in the solid-state electrolyte $Li_7La_3Zr_2O_{12}$. *Chem Mater* 2017, **29**: 7961–7968.

[179] Fu JM, Yu PF, Zhang N, *et al*. *In situ* formation of a bifunctional interlayer enabled by a conversion reaction to initiatively prevent lithium dendrites in a garnet solid electrolyte. *Energy Environ Sci* 2019, **12**: 1404–1412.

[180] Tian YS, Shi T, Richards WD, *et al*. Compatibility issues between electrodes and electrolytes in solid-state batteries. *Energy Environ Sci* 2017, **10**: 1150–1166.

[181] Hakari T, Deguchi M, Mitsuhara K, *et al*. Structural and electronic-state changes of a sulfide solid electrolyte during the Li deinsertion-insertion processes. *Chem Mater* 2017, **29**: 4768–4774.

[182] Koerver R, Walther F, Aygün I, *et al*. Redox-active cathode interphases in solid-state batteries. *J Mater Chem A* 2017, **5**: 22750–22760.

[183] Xia SX, Lopez J, Liang C, *et al*. High-rate and large-capacity lithium metal anode enabled by volume conformal and self-healable composite polymer electrolyte. *Adv Sci* 2019, **6**: 1802353.

[184] Xiang X, Cao SY, Chen F, *et al*. Li/$Li_7La_3Zr_2O_{12}$ interfacial modification by constructing a layer of Cu–Li alloy. *J Electrochem Soc* 2019, **166**: A3028–A3030.

[185] Chen SJ, Zhang JX, Nie L, *et al*. All-solid-state batteries with a limited lithium metal anode at room temperature using a garnet-based electrolyte. *Adv Mater* 2021, **33**: 2002325.

[186] Rettenwander D, Wagner R, Reyer A, *et al*. Interface instability of Fe-stabilized $Li_7La_3Zr_2O_{12}$ versus Li metal. *J Phys Chem C* 2018, **122**: 3780–3785.

[187] Ma C, Cheng YQ, Yin KB, *et al*. Interfacial stability of Li metal-solid electrolyte elucidated via *in situ* electron microscopy. *Nano Lett* 2016, **16**: 7030–7036.

[188] Han FD, Westover AS, Yue J, *et al*. High electronic conductivity as the origin of lithium dendrite formation within solid electrolytes. *Nat Energy* 2019, **4**: 187–196.

[189] Yonemoto F, Nishimura A, Motoyama M, *et al*. Temperature effects on cycling stability of Li plating/stripping on Ta-doped $Li_7La_3Zr_2O_{12}$. *J Power Sources* 2017, **343**: 207–215.

[190] Taylor NJ, Stangeland-Molo S, Haslam CG, *et al*. Demonstration of high current densities and extended cycling in the garnet $Li_7La_3Zr_2O_{12}$ solid electrolyte. *J Power Sources* 2018, **396**: 314–318.

[191] Qian JF, Henderson WA, Xu W, *et al*. High rate and stable cycling of lithium metal anode. *Nat Commun* 2015, **6**: 6362.

[192] Cheng EJ, Sharafi A, Sakamoto J. Intergranular Li metal propagation through polycrystalline $Li_{6.25}Al_{0.25}La_3Zr_2O_{12}$ ceramic electrolyte. *Electrochimica Acta* 2017, **223**: 85–91.

[193] Raj R, Wolfenstine J. Current limit diagrams for dendrite formation in solid-state electrolytes for Li-ion batteries. *J Power Sources* 2017, **343**: 119–126.

[194] Ren YY, Shen Y, Lin YH, *et al*. Direct observation of lithium dendrites inside garnet-type lithium-ion solid electrolyte. *Electrochem Commun* 2015, **57**: 27–30.

[195] Yang CP, Zhang L, Liu BY, *et al*. Continuous plating/stripping behavior of solid-state lithium metal anode in a 3D ion-conductive framework. *PNAS* 2018, **115**: 3770–3775.

[196] Ishiguro K, Nemori H, Sunahiro S, *et al*. Ta-doped $Li_7La_3Zr_2O_{12}$ for water-stable lithium electrode of lithium–air batteries. *J Electrochem Soc* 2014, **161**: A668–A674.

[197] Sudo R, Nakata Y, Ishiguro K, *et al*. Interface behavior between garnet-type lithium-conducting solid electrolyte and lithium metal. *Solid State Ionics* 2014, **262**: 151–154.

[198] Porz L, Swamy T, Sheldon BW, *et al*. Mechanism of lithium metal penetration through inorganic solid electrolytes. *Adv Energy Mater* 2017, **7**: 1701003.

[199] Kerman K, Luntz A, Viswanathan V, *et al*. Practical challenges hindering the development of solid state Li ion batteries. *J Electrochem Soc* 2017, **164**: A1731–A1744.

[200] Han FD, Yue J, Zhu XY, *et al*. Suppressing Li dendrite formation in Li_2S–P_2S_5 solid electrolyte by LiI incorporation. *Adv Energy Mater* 2018, **8**: 1703644.

[201] Albertus P, Babinec S, Litzelman S, *et al*. Status and challenges in enabling the lithium metal electrode for high-energy and low-cost rechargeable batteries. *Nat Energy* 2018, **3**: 16–21.

[202] Deng Z, Wang ZB, Chu IH, *et al*. Elastic properties of alkali superionic conductor electrolytes from first principles calculations. *J Electrochem Soc* 2015, **163**: A67–A74.

[203] Wang CW, Fu K, Kammampata SP, *et al*. Garnet-type solid-state electrolytes: Materials, interfaces, and batteries. *Chem Rev* 2020, **120**: 4257–4300.

[204] Han FD, Zhu YZ, He XF, *et al*. Electrochemical stability of $Li_{10}GeP_2S_{12}$ and $Li_7La_3Zr_2O_{12}$ solid electrolytes. *Adv Energy Mater* 2016, **6**: 1501590.

[205] Thompson T, Yu S, Williams L, *et al*. Electrochemical window of the Li-ion solid electrolyte $Li_7La_3Zr_2O_{12}$. *ACS Energy Lett* 2017, **2**: 462–468.

[206] Nitta N, Wu FX, Lee JT, *et al*. Li-ion battery materials:

Present and future. *Mater Today* 2015, **18**: 252–264.

[207] Miara L, Windmüller A, Tsai CL, *et al*. About the compatibility between high voltage spinel cathode materials and solid oxide electrolytes as a function of temperature. *ACS Appl Mater Interfaces* 2016, **8**: 26842–26850.

[208] Ren YY, Liu T, Shen Y, *et al*. Chemical compatibility between garnet-like solid state electrolyte $Li_{6.75}La_3Zr_{1.75}Ta_{0.25}O_{12}$ and major commercial lithium battery cathode materials. *J Materiomics* 2016, **2**: 256–264.

[209] Park K, Yu BC, Jung JW, *et al*. Electrochemical nature of the cathode interface for a solid-state lithium-ion battery: Interface between $LiCoO_2$ and garnet-$Li_7La_3Zr_2O_{12}$. *Chem Mater* 2016, **28**: 8051–8059.

[210] Ohta S, Komagata S, Seki J, *et al*. All-solid-state lithium ion battery using garnet-type oxide and Li_3BO_3 solid electrolytes fabricated by screen-printing. *J Power Sources* 2013, **238**: 53–56.

[211] Liu BY, Fu K, Gong YH, *et al*. Rapid thermal annealing of cathode-garnet interface toward high-temperature solid state batteries. *Nano Lett* 2017, **17**: 4917–4923.

[212] Zhang N, Long XH, Wang Z, *et al*. Mechanism study on the interfacial stability of a lithium garnet-type oxide electrolyte against cathode materials. *ACS Appl Energy Mater* 2018, **1**: 5968–5976.

[213] Lee JS, Heo K, Kim HS, *et al*. Blended cathode materials for all-solid-state Li-ion batteries. *J Alloys Compd* 2019, **781**: 553–559.

[214] Xiao YH, Miara LJ, Wang Y, *et al*. Computational screening of cathode coatings for solid-state batteries. *Joule* 2019, **3**: 1252–1275.

[215] Kim KJ, Rupp JLM. All ceramic cathode composite design and manufacturing towards low interfacial resistance for garnet-based solid-state lithium batteries. *Energy Environ Sci* 2020, **13**: 4930–4945.

[216] Lin DC, Liu W, Liu YY, *et al*. High ionic conductivity of composite solid polymer electrolyte via *in situ* synthesis of monodispersed SiO_2 nanospheres in poly(ethylene oxide). *Nano Lett* 2016, **16**: 459–465.

[217] Sheng OW, Jin CB, Luo JM, *et al*. $Mg_2B_2O_5$ nanowire enabled multifunctional solid-state electrolytes with high ionic conductivity, excellent mechanical properties, and flame-retardant performance. *Nano Lett* 2018, **18**: 3104–3112.

[218] Xue ZG, He D, Xie XL. Poly(ethylene oxide)-based electrolytes for lithium-ion batteries. *J Mater Chem A* 2015, **3**: 19218–19253.

[219] Zhang JJ, Zhao JH, Yue LP, *et al*. Safety-reinforced poly(propylene carbonate)-based all-solid-state polymer electrolyte for ambient-temperature solid polymer lithium batteries. *Adv Energy Mater* 2015, **5**: 1501082.

[220] Rosso M, Brissot C, Teyssot A, *et al*. Dendrite short-circuit and fuse effect on Li/polymer/Li cells. *Electrochimica Acta* 2006, **51**: 5334–5340.

[221] Huo HY, Sun JY, chen C, *et al*. Flexible interfaces between Si anodes and composite electrolytes consisting of poly(propylene carbonates) and garnets for solid-state batteries. *J Power Sources* 2018, **383**: 150–156.

[222] Chen H, Jing MX, Han C, *et al*. A novel organic/inorganic composite solid electrolyte with functionalized layers for improved room-temperature rate performance of solid-state lithium battery. *Int J Energy Res* 2019, **43**: 5912–5921.

[223] Ma C, Feng YM, Xing FZ, *et al*. A borate decorated anion-immobilized solid polymer electrolyte for dendrite-free, long-life Li metal batteries. *J Mater Chem A* 2019, **7**: 19970–19976.

[224] Sun JQ, Li YG, Zhang QH, *et al*. A highly ionic conductive poly(methyl methacrylate) composite electrolyte with garnet-typed $Li_{6.75}La_3Zr_{1.75}Nb_{0.25}O_{12}$ nanowires. *Chem Eng J* 2019, **375**: 121922.

[225] Tian GY, Zhao ZJ, Zinkevich T, *et al*. A crosslinked polyethyleneglycol solid electrolyte dissolving lithium bis(trifluoromethylsulfonyl)imide for rechargeable lithium batteries. *ChemSusChem* 2019, **12**: 4708–4718.

[226] Yan CY, Zhu P, Jia H, *et al*. Garnet-rich composite solid electrolytes for dendrite-free, high-rate, solid-state lithium-metal batteries. *Energy Storage Mater* 2020, **26**: 448–456.

[227] He ZJ, Chen L, Zhang BC, *et al*. Flexible poly(ethylene carbonate)/garnet composite solid electrolyte reinforced by poly(vinylidene fluoride-hexafluoropropylene) for lithium metal batteries. *J Power Sources* 2018, **392**: 232–238.

[228] Li Z, Huang HM, Zhu JK, *et al*. Ionic conduction in composite polymer electrolytes: Case of PEO: Ga-LLZO composites. *ACS Appl Mater Interfaces* 2019, **11**: 784–791.

[229] Choi J-H, Lee C-H, Yu J-H, *et al*. Enhancement of ionic conducntivity of composite membranes for all-solid-state lithium rechargable batteries incorporating tetragonal $Li_7La_3Zr_2O_{12}$ into a polyethylene oxide matrix. *J Power Sources* 2015, **274**: 458–463.

[230] He KQ, Chen CL, Fan R, *et al*. Polyethylene oxide/garnet-type $Li_{6.4}La_3Zr_{1.4}Nb_{0.6}O_{12}$ composite electrolytes with improved electrochemical performance for solid state lithium rechargeable batteries. *Compos Sci Technol* 2019, **175**: 28–34.

[231] Guo HL, Sun H, Jiang ZL, *et al*. A new type of composite electrolyte with high performance for room-temperature solid-state lithium battery. *J Mater Sci* 2019, **54**: 4874–4883.

[232] Karthik K, Murugan R. Lithium garnet based free-standing solid polymer composite membrane for rechargeable lithium battery. *J Solid State Electrochem* 2018, **22**: 2989–2998.

[233] Jiang TL, He PG, Wang GX, *et al*. Solvent-free synthesis of thin, flexible, nonflammable garnet-based composite solid electrolyte for all-solid-state lithium batteries. *Adv Energy Mater* 2020, **10**: 1903376.

[234] Zhang JX, Zhao N, Zhang M, *et al*. Flexible and ion-conducting membrane electrolytes for solid-state

lithium batteries: Dispersion of garnet nanoparticles in insulating polyethylene oxide. *Nano Energy* 2016, **28**: 447–454.

[235] Huang X, Liu C, Lu Y, *et al*. A Li-Garnet composite ceramic electrolyte and its solid-state Li-S battery. *J Power Sources* 2018, **382**: 190–197.

[236] Tao XY, Liu YY, Liu W, *et al*. Solid-state lithium-sulfur batteries operated at 37 ℃ with composites of nanostructured $Li_7La_3Zr_2O_{12}$/carbon foam and polymer. *Nano Lett* 2017, **17**: 2967–2972.

[237] Zhou C, Samson AJ, Hofstetter K, *et al.* A surfactant-assisted strategy to tailor Li-ion charge transfer interfacial resistance for scalable all-solid-state Li batteries. *Sustainable Energy Fuels* 2018, **2**: 2165–2170.